U.PORTO
FACULDADE DE CIÊNCIAS
UNIVERSIDADE DO PORTO

PhD

PhD
3.º CICLO
FCUP
ANO

U.PORTO

Precise spectroscopic analysis of solar-type stars with moderate and fast rotation

Maria Tsantaki

FC

U.PORTO
FACULDADE DE CIÊNCIAS
UNIVERSIDADE DO PORTO

Precise spectroscopic analysis of solar-type stars with moderate and fast rotation

Maria Tsantaki

Tese de Doutoramento apresentada à
Faculdade de Ciências da Universidade do Porto,
Departamento de Física e Astronomia

2015

PhD

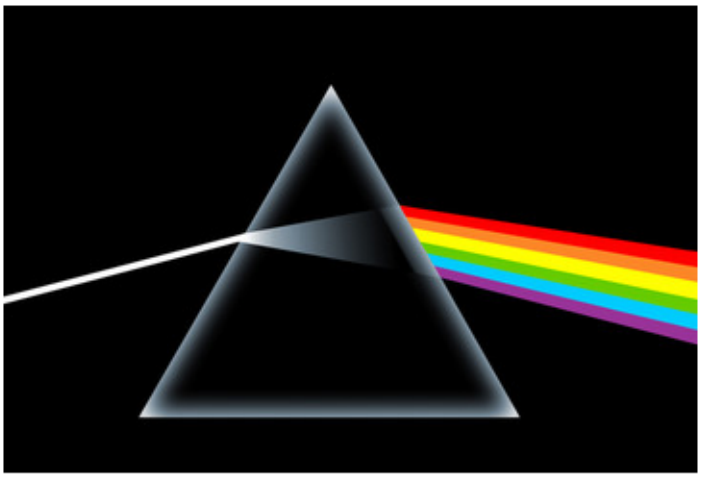

Precise spectroscopic analysis of solar-type stars with moderate and fast rotation

Maria Tsantaki

Doutoramento em Astronomia
Departamento de Física e Astronomia
2014

Orientador
Sérgio A. G. Sousa, Investigador,
Faculdade de Ciências

Coorientador
Nuno C. Santos, Professor Associado Convidado,
Faculdade de Ciências

PhD

U.PORTO

FACULDADE DE CIÊNCIAS
UNIVERSIDADE DO PORTO

Precise spectroscopic analysis of solar-type stars with moderate and fast rotation

Maria Tsantaki

Centro de Astrofísica da Universidade do Porto
Departamento de Física e Astronomia, Faculdade de Ciências, Universidade do Porto
Tese de Doutouramento

Orientadores: S. G. Sousa, N. C. Santos

October, 2014

To Astrophysics

"May it help free minds in destroying ignorance, superstitions, and beliefs in god-like entities."

Abstract

In this thesis, I describe the processes of deriving the fundamental stellar parameters for solar-type stars. The purpose of this thesis is to optimize existing methods but also create new methodologies for determining stellar parameters that covers a very diverse group of stars.

In Chapters 2 and 3, I describe the standard method of deriving stellar parameters for slowly rotating FGK stars that is based on the measurement of equivalent width (EW) of iron lines and by imposing ionization and excitation balance. Even though, this method has been successfully applied to large sample of stars, it has been reported considerable discrepancies for the lower temperature regime ($T_{\rm eff} < 5000\,{\rm K}$). These stars have line-crowded spectra and the precise measurement of the EW is difficult.

We dealt with this problem by carefully selecting a line list, using a K-type star as a reference. The new parameters for cool stars are now in agreement with more model-independent methods, namely the infrared flux method. The new line list is also used for giant stars and for the cooler planet hosts.

A principal part of this thesis was to create a procedure to deal with stars with high rotational velocities. The parameters for these stars cannot be derived with the standard EW method because their spectral lines are broadened and therefore strongly blended. In chapter 4, I present the basic principles of the spectral synthesis technique. In chapter 5, I present a refinement of the spectral synthesis technique designed to treat fast rotating stars better. The comparison of our stellar parameters shows good agreement with literature values, both for slowly and for fast rotating stars. In addition, our results are on the same scale as the parameters derived from the EW method, presented in our previous work. We applied the new methodology to transit planet hosts, as these stars have wide dispersion in their rotational velocities compared to the radial velocity targets.

With this thesis, we provide the tools to derive precise stellar parameters. This work is expected to have strong impact on the study of stellar populations of the Milky Way, the characterization of planets and their hosts, and understanding stellar atmospheres.

Resumo

Nesta tese, descrevo os processos de derivação de parmetros fundamentais estelares para estrelas do tipo solar. O propósito desta tese é, não só optimizar mtodos existentes, mas também criar novas metodologias para a determinação de parâmetros estelares que abranjam um grupo muito diverso de estrelas.

Nos capítulos 2 e 3, descrevo o mtodo padro de derivação de parâmetros estelares para estrelas FGK de baixa rotação, baseado na medição da largura equivalente (LE) de linhas de ferro e impondo um equilíbrio de ionização e excitação. Apesar deste método ter sido aplicado com sucesso a numerosas amostras de estrelas, várias discrepâncias tm sido referidas para estrelas no regime de temperaturas baixas ($T_{\rm eff}$ <5000 K). Estas estrelas têm espectros sobrecarregados por linhas e a medição das suas LE com precisão é difícil.

Lidámos com este problema através da selecção cuidadosa de uma lista de linhas, utilizando uma estrela do tipo K como referência. Os novos parmetros para as estrelas de temperatura baixa mostram uma concordância com métodos mais independentes de modelos. A nova lista de linhas também foi usada para estrelas gigantes e para estrelas de baixa temperatura que hospedam planetas.

Uma parte importante desta tese foi a criação de uma metodologia para lidar com estrelas com altas velocidades de rotação. Os parâmetros destas estrelas não podem ser obtidos pelo mtodo padrão de LE porque as suas linhas espectrais estão alargadas e, portanto, extremamente misturadas. No capítulo 4, apresento os princípios da técnica de síntese espectral. No capítulo 5, apresento um aperfeiçoamento da técnica de síntese espectral destinado a um melhor tratamento de estrelas de alta-rotação. A comparação dos nossos parâmetros estelares mostra uma boa concordância com valores presentes na literatura, tanto para estrelas de baixa-rotação como de alta-rotação. Adicionalmente, os resultados que obtivemos através do método de síntese estão em concordância com os parâmetros obtidos pelo método de LE, os quais apresentámos no nosso trabalho anterior. Aplicámos a nova metodologia a estrelas que hospedam planetas detectados através do método de trânsitos, pois estas estrelas têm uma dispersão mais elevada nas suas velocidades de rotação quando comparadas com estrelas observadas com o método

das velocidades radiais.

CONTENTS

LIST OF FIGURES

LIST OF TABLES

CHAPTER 1

Introduction

> "The universe is a pretty big place. If it's just us, seems like an awful waste of space."
>
> Carl Sagan, Contact

Is there anybody out there? There is no better place to answer this question but the field of extrasolar planets. Astronomers focus on exploring what would be one of the greatest discoveries of modern astronomy, new earths that could harbor life. As of January 2015, there are more than 1187 exoplanetary systems discovered[1] (Fig. 1.1) and the future looks even more promising as new missions are dedicated to this purpose (e.g., CHEOPS, TESS, PLATO 2.0).

From the very first discovery of an extrasolar planet orbiting a solar-type star (Mayor & Queloz 1995), it became clear that our Solar system is not the only possible configuration. This new planet was found in close orbit to the host star in contrast to our system, suggesting alternative formation mechanisms than it was previously thought. The discoveries that subsequently followed, revealed an impressive diversity of planets. For example, Kepler-16 b is a Saturn-mass planet orbiting a binary star, closely resembling Tatooine from the Star Wars series, proving that nature can reproduce fiction in

[1] according to www.exoplanet.eu

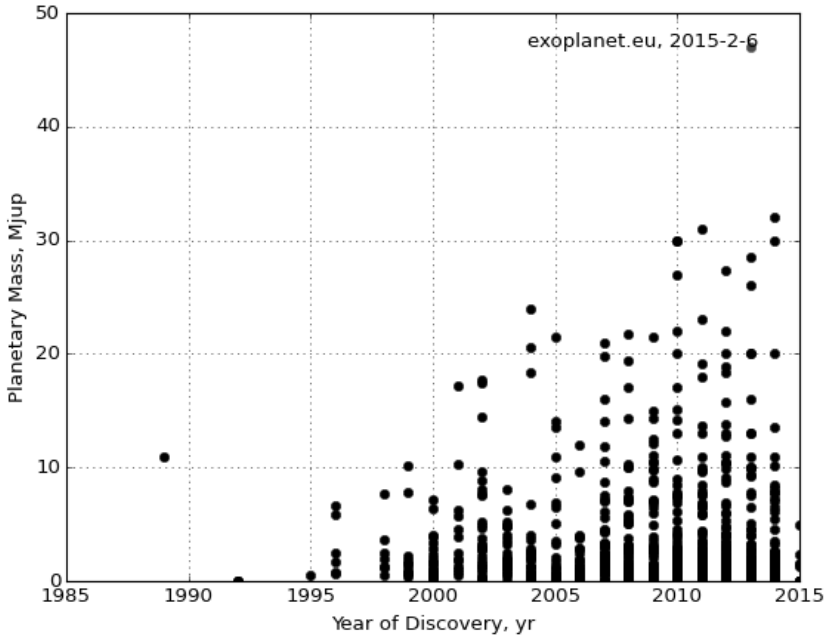

Figure 1.1: Planetary masses presented by the year of discovery according to exoplanet.eu

the best way. An artist conception of known planets that are likely to be habitable is shown in Fig. 1.2.

Most planet detection methods are indirect and focus on the observations of the host star. The most efficient ones are the radial velocity (RV) and the transit techniques. The RV method is based on the detection of variations in the radial velocity of the star, due to the gravitational pull from a planet as it orbits the star. When the star moves towards our line of sight, its spectrum is blueshifted, while it is redshifted when it moves away. While the above methods provide information about the planetary mass, the transit method can determine the radius of a planet. If a planet transits in front of the disc of its parent star, then the observed flux of the star drops a small amount.

The derivation of the planetary mass and radius (and other planetary parameters that depend on the above, such as density and temperature) are critically dependent on the fundamental atmospheric parameters of the planet host. Moreover, the fast growing samples of planet hosts have revealed interesting correlations between various parameters of planets and their hosts (some of them listed in Sect. 1.2) that provide the necessary constrains on their formation and evolution theories.

Even though our motivation is to study planet hosts in order to understand the planets themselves, there are even many more fields in astronomy related to the study of solar-type stars in our Galaxy. In the following sections, we present briefly the fields where fundamental stellar parameters are important.

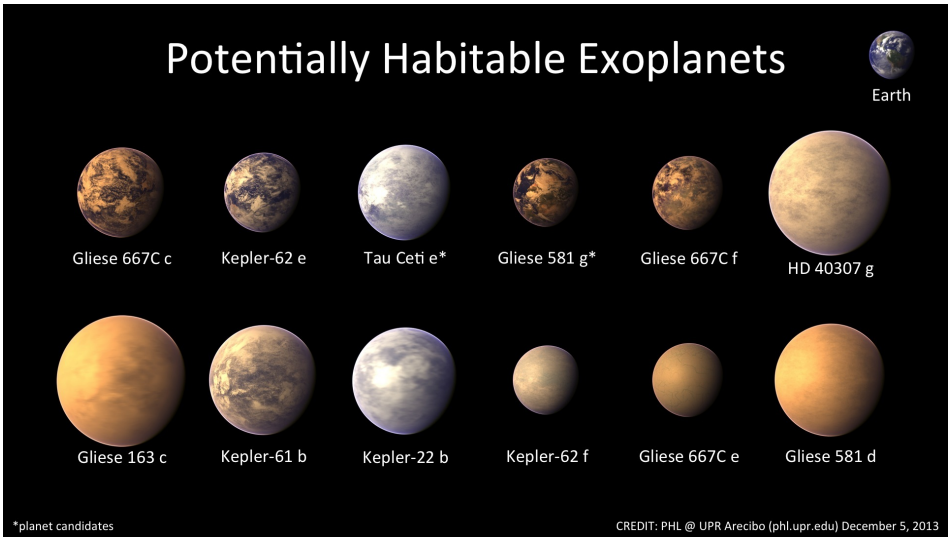

Figure 1.2: An artist conception of known planets that are likely to be habitable (Credit to UPR Arecibo).

1.1 Planetary and stellar characterization

To understand the physical processes involved in the formation and evolution of planetary systems, precise measurements of the fundamental properties of the exoplanets and their hosts are required.

From the analysis of the light curve of a transiting planet, the planetary radius is always dependent on the stellar radius ($R_p \propto R_\star$). Moreover, the mass of the planet, or the minimum mass in case the inclination of the orbit is not known, is calculated from the RV curve only if the mass of the star is known ($M_p \propto M_\star^{2/3}$). On the other hand, the stellar mass and radius depend on the observationally determined atmospheric parameters (with the exception of stars with interferometric measurements or stars that belong to eclipsing binaries) such as, effective temperature ($T_{\rm eff}$), surface gravity ($\log g$), and metallicity ([Fe/H], where iron is usually used as a proxy). The latter parameters are used to deduce stellar mass and radius either from calibrations (Torres et al. 2010; Santos et al. 2013) or stellar evolutionary models (e.g., Girardi et al. 2002).

It is therefore, imperative to derive precise and accurate stellar parameters to avoid the propagation of errors in the planetary properties. For instance, Torres et al. (2012) compared stellar parameters derived from spectral synthesis techniques with the ones after constraining surface gravity derived from the transit light curve. The authors show considerable systematic errors in the planetary mass and radius between the constrained and unconstrained analyses. In particular, the overestimated values of stellar radius (corresponds in turn to overestimated planetary radius) observed with the unconstrained analysis, may explain part of the anomalously inflated radii that has been reported for some Jovian planets, such as in the cases of HD 209458 b (Burrows et al. 2000) and

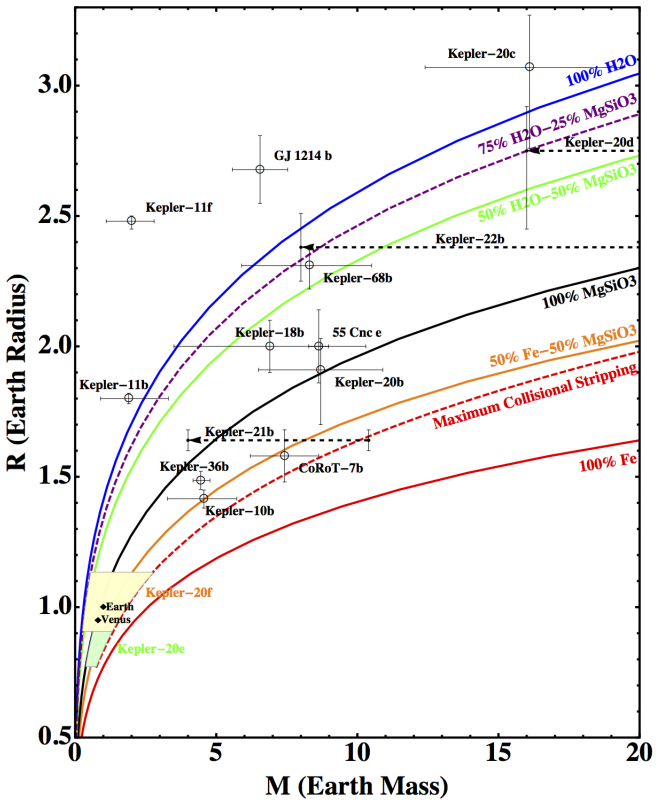

Figure 1.3: A model grid for solid planets from 0.1 through 100 earth masses. Transiting exoplanets are shown with their measured mass and radius. Earth and Venus are shown for comparison. The curves are calculated for planets composed of pure Fe, 50% Fe-50% $MgSiO_3$, pure $MgSiO_3$, 50% H_2O-50% $MgSiO_3$, 75% H_20-25% $MgSiO_3$ and pure H_2O. The red dashed curve is the maximum collisional stripping curve. Taken from Zeng & Sasselov (2013).

WASP-12 b (Hebb et al. 2009).

A combination of the RV and transit techniques can provide complete planet characterization by obtaining information on the planetary mass, radius, and density, only if precise and accurate stellar parameters are available. For example, planetary mean densities indicate their bulk composition, characterizing them between gaseous bulks (H, He, and water) or rocky (Fe or Ni) (Zeng & Seager 2008; Valencia et al. 2007). To date, densities are only known for a few planets, and even less for the smaller ones (Marcy et al. 2014), leaving the interior structure of exoplanets still as one of the open questions in the field (Fig. 1.3).

In addition, the planetary equilibrium temperature is defined as the theoretical temperature of the planet as if it were a black body heated only by its parent star. The temperature at which the thermal equilibrium exists, i.e. the power supplied by the star is equal to the power emitted by the planet, is proportional to the effective temperature and the radius of the star ($T_{eq} \propto T_{\rm eff} \times R_\star^{1/2}$).

1.2 Correlations between planets and their stellar hosts

Apart from the derivation of planetary properties mentioned above, stellar parameters can be used to reveal correlations between planets and their host stars that will give insights on their formation and evolution mechanisms. Several correlations have been studied so far with very interesting results.

- Metallicity and giant planet frequency. After the first detections of planets, it became clear that the stars hosting giant planets were systematically more metal rich than non hosts (Fig. 1.4). Several authors have confirmed the metallicity and planet frequency relation (Gonzalez 1997; Santos et al. 2004; Fischer & Valenti 2005; Sousa et al. 2008). This well established relation implies that core accretion is the main formation mechanism of giant planets (Pollack et al. 1996; Ida & Lin 2004; Mordasini et al. 2012) and not disc instability (Boss 2002). In the traditional core accretion scenario, giant planets are formed by a runaway accretion of gas around a previously formed rocky or icy core with ∼10-15 Earth masses. On the other hand, disc instability theories suggest a direct planet formation from a self-gravitational instability of the gaseous portion of the protoplanetary disk, resulting in shorter timescales to form planets.

  However, recent studies (e.g., Sousa et al. 2011; Buchhave et al. 2012) point out that for stars hosting Neptune-like and super-Earth planets, the metallicity correlation may no longer be valid suggesting that low-mass planets represent a different population.

- Abundances of other than iron elements. The composition of exoplanetary interiors and atmospheres are sensitive to the abundances of the host stars (e.g., Bond et al. 2010; Teske et al. 2013). Recent studies show that stars harboring both Jovian and Neptunian planets, with low metallicities are enhanced in alpha elements[2] compared to the non-host counterparts (Haywood 2008; Adibekyan et al. 2012b,a). These results indicate that metals other than iron may also have an important contribution to planet formation in metal poor environments. These observational studies favor the core accretion scenario where the formation of planetesimals starts from the condensation of heavy elements.

- Spin-orbit misalignment. For transiting planets, the spin-orbit angle can be measured via the Rossiter-McLaughlin effect. The Rossiter-McLaughlin effect is observed spectroscopically when a planet transits across the disc of the parent star. When a planet transits, it blocks part of the stellar disc, preventing some of the light from reaching the observer. In this way, parts of the rotating stellar surface are blocked, causing an anomalous net Doppler shift, which changes the stellar RV. This rotation anomaly depends on the angle between the projections of the stellar

[2]The elements synthesized during nuclear fusion reactions in which stars convert helium into heavier elements by the progressive addition of helium nuclei are called alpha elements, e.g. (C, N), O, Ne, Mg, Si, S, Ar, Ca, Ti.

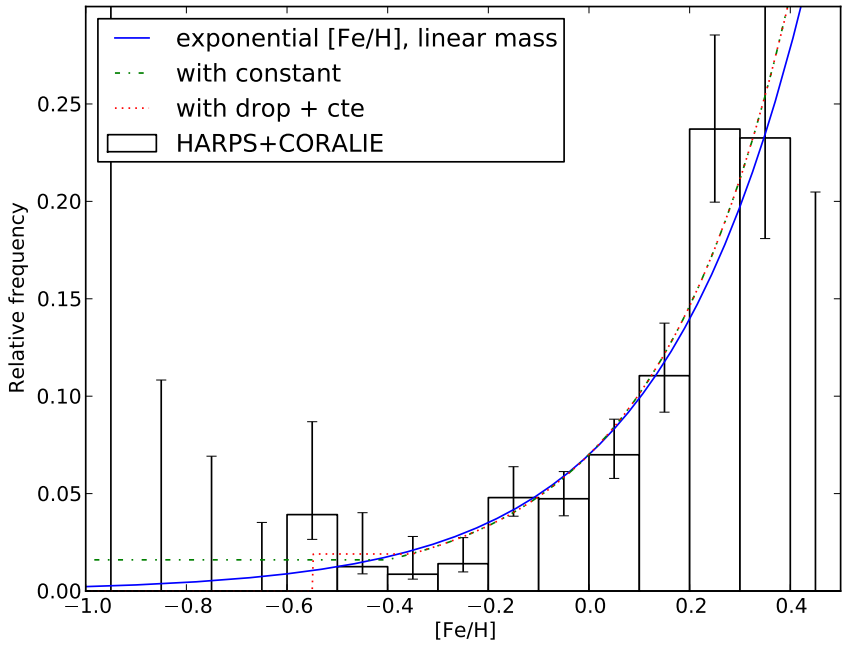

Figure 1.4: Frequency of giant planets as a function of metallicity and mass of the HARPS and the CORALIE sample. Three different functional forms are shown: a complete exponential with linear mass (blue curve), an exponential and a constant (green curve), and an exponential, a constant plus a drop (red curve). Taken from Mortier et al. (2013a).

rotation axis and orbital axis of the occultating companion that represents stellar obliquity. According to Winn et al. (2010) and Albrecht et al. (2012), there is a possible correlation between the stellar effective temperature and the obliquities of hot Jupiter systems where the misaligned systems are preferentially those with the hottest photospheres. Observational works also support this correlation providing clues for the tidal interaction between planets and their hosting stars (e.g., Johnson et al. 2011).

- Radius anomaly. A puzzling feature of hot Jupiters is that many of them have radii either too large or too small compared to the one guessed prior to their discovery. This discrepancy is referred as the the radius anomaly (the discrepancy between the observed radius and the one expected from planetary models). There is evidence for a possible correlation between the effective temperature, metallicity, and the radius anomaly for giant planets (Guillot et al. 2006; Laughlin et al. 2011).

  The small size of some planets can be explained as a consequence of heavy-metal enrichment. As for the larger radii, possible explanations include tidal friction, unexpected atmospheric properties, and heating from electrical currents driven by star-planet interactions.

- Lithium and the planet presence. Israelian et al. (2004) and Delgado Mena et al.

(2014) show that planet hosts are significantly more Li-depleted than stars without known planets. Even though there are some contradictory works (e.g., Ramírez et al. 2012), this correlation seems not to be associated to differences of age, mass, or metallicity between stars with and without planets (Sousa et al. 2010).

The mechanisms proposed to explain how the presence of planets could affect lithium depletion are 1) planetary migration, which affects the evolution of the angular momentum of the star (Castro et al. 2008) and 2) interactions between the protoplanetary disk and the star, which determine the degree of differential rotation between the radiative core and the convective envelope, therefore having an important impact on rotational mixing (Bouvier 2008; Israelian et al. 2009).

1.3 Galactic evolution

To understand the chemo-dynamical evolution of the Milky Way disc, it is important to study large stellar populations for the reconstruction of the history of our Galaxy. With the growing number of large Galactic surveys (e.g., APOGEE, RAVE, Gaia-ESO), the number of stars analyzed with high spectroscopic resolution has increased to several tens of thousands with available measurements of their kinematics, ages and chemical abundances. These surveys has addressed the question of the thin to thick disc transition with a robust statistical approach and provide constrains to Galactic evolution models (Fig. 1.5).

Kinematic and chemical analyses have been used to study the Milky Way for decades (e.g., Gilmore et al. 1989; Ivezić et al. 2012), providing, for example, the evidence of the existence of the Galactic thick disc (Gilmore & Reid 1983).

All heavy elements are produced in stars by nucleosynthesis. Therefore, the metal abundance of subsequent generations of stars should increase with time. The evolution of chemical element abundances in a galaxy provides a clock for galactic aging. The iron abundance is often used as a proxy of the overall metallicity and is of particular importance because it is a key ingredient for the study of the chemical evolution of stellar systems. Relations between the elemental abundance ratios [X/Fe] versus [Fe/H] (where X is the abundance of the element X) are generally used as tracers for the chemical evolution of galaxies (e.g., Reddy et al. 2003; Tolstoy et al. 2009; Adibekyan et al. 2012c, 2013). Thus, a good determination of the iron abundance is of fundamental importance.

1.4 The fundamental stellar parameters

In this work, we define as fundamental the parameters necessary to characterize a stellar atmosphere and are obtained from a first analysis of the spectrum. These parameters are the effective temperature, metallicity, and surface gravity, and define the physical conditions in the stellar atmosphere.

- Effective temperature. The effective temperature of a star is the temperature of a black body with the same luminosity per surface area (bolometric flux, $\mathcal{F}_{\rm Bol}$) as

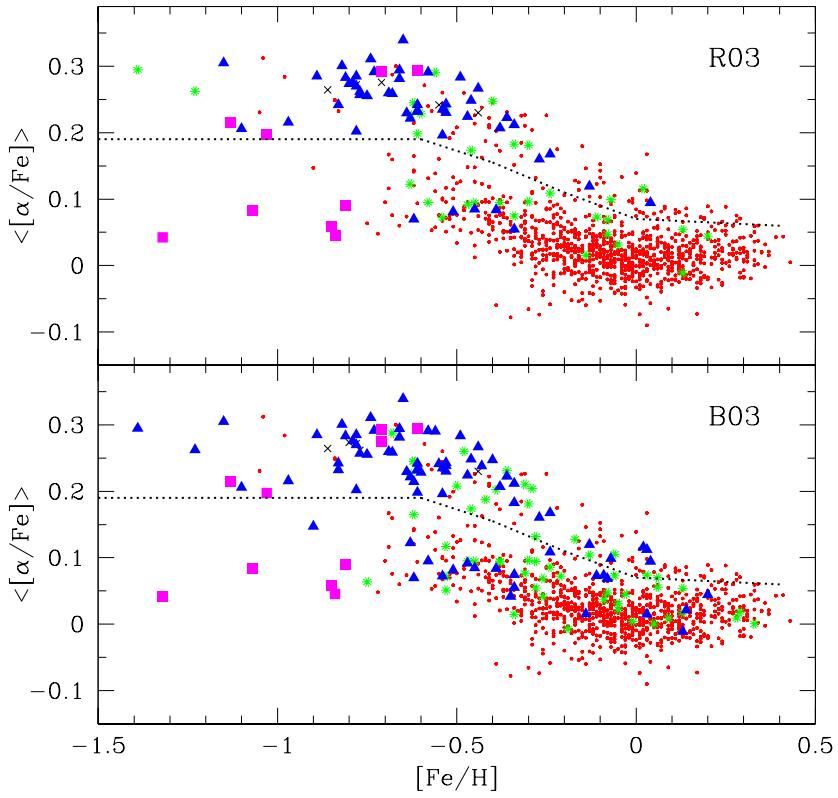

Figure 1.5: Abundance ratios [α/Fe] vs. [Fe/H] for the total HARPS sample. The blue triangles refer to the thick disk, red circles to the thin disk. The green asterisks and the black crosses refer to the transition stars between thin-thick and thick-halo, respectively. Magenta squares represent the stars belonging to the halo. The black dashed curve separates the stars with high- and low-α content. The top and bottom panels show the separation of the stellar groups according to the Reddy et al. (2006) (R06) and Bensby et al. (2003) (B03) criteria, respectively. Taken from Adibekyan et al. (2012b).

the star and is defined according to the Stefan-Boltzmann law:

$$\mathcal{F}_{\rm Bol} = \sigma T_{\rm eff}^4. \tag{1.1}$$

- Metallicity. With the term stellar metallicity we refer to the abundance of elements heavier than helium as a result of nucleosynthesis. The general definition of metallicity is expressed as:

$$[X/Y] = A(X) - A(Y) - (A(X) - A(Y))_\odot,$$

where A(X) = logN(X) – logN(H) + 12, and N is the number density.

- Surface gravity. The surface gravity is a measure of the photospheric pressure of the stellar atmosphere and can be calculated directly from Newton's Law of

Gravitation, which gives the formula:

$$g = \frac{GM}{R^2}, \tag{1.2}$$

where M is the mass of the object, R is its radius, and G is the gravitational constant.

From the above parameters we can later infer stellar mass, radius, and age. Other important parameters are the abundances of other elements and the parameters related to velocity fields, such as the projected rotational velocity ($\upsilon \sin i$), microturbulence (ξ_t), and macroturbulence (υ_{mac}). For solar-type stars, the techniques for the determination of the fundamental stellar parameters are spectroscopy, photometry and interferometry, or a combination of all.

Spectroscopy is a powerful technique for deriving stellar parameters. The stellar spectrum contains a large amount of information of the processes inside the stellar atmosphere since is the place where the spectral features we observe are formed. The huge amount of spectroscopic data challenges us to develop automatic procedures to perform the required analysis. Numerous automatic methods have been developed over the past years to handle large data sets (e.g., Valenti & Piskunov 1996; Katz et al. 1998; Recio-Blanco et al. 2006; Koleva et al. 2009; Jofré et al. 2010; Tabernero et al. 2012; Mucciarelli et al. 2013; Magrini et al. 2013; Blanco-Cuaresma et al. 2014).

Some spectroscopic methods for the determination of the atmospheric parameters are listed below.

- The Hα wings provide an excellent $T_{\rm eff}$ diagnostic for stars cooler than about 8000 K due to their virtually zero gravity dependence (e.g., Fuhrmann 2004).
- The line depth ratio technique can be used as a stellar thermometer based on the fact that metal lines have different sensitivities to $T_{\rm eff}$ (e.g., Gray 1994).
- In a detailed spectral analysis, the equivalent widths of spectral lines (usually iron) are often measured. The atmospheric parameters are derived by imposing the excitation and ionization balance of iron lines (e.g., Santos et al. 2004, see also Sect. 2).
- An alternative to the analysis of individual spectral lines, is to use wavelength intervals of the observed spectrum and compare with a synthetic spectrum, yielding the best-fit parameters (e.g., Valenti & Fischer 2005, see also Sect. 4).

Apart from spectroscopy, there are photometric methods proposed for the determination of the effective temperature.

- There have been many photometric systems to describe stellar flux distributions through colour differences. The effective temperature can be estimated from photometric colour indices, such as the $V-K$ and $B-V$ calibrations (e.g., Ramírez & Meléndez 2005).

- In addition, the infrared flux method (IRFM) proposed by Blackwell & Shallis (1977) provides precise temperature estimations based on the fact that the bolometric flux depends on the angular diameter and the effective temperature, as described by the Stefan-Boltzmann law, whereas the monochromatic flux in the infrared (IR) depends on the angular diameter but weakly on the effective temperature, this way the dependence on the angular diameter disappears:

$$\frac{f_{bol}}{f_{\lambda IR}} = \frac{\sigma T_{\rm eff}^4}{f_{\lambda IR}(model)}, \tag{1.3}$$

  where f_{bol} is the measured bolometric flux, $f_{\lambda IR}$ is the measured monochromatic IR flux and $f_{\lambda IR}$(model) is the monochromatic flux in the IR derived by the assuming model. This technique is more model-independent compared to the aforementioned spectroscopic techniques and has been implemented by various authors over the years (e.g., Ramírez & Meléndez 2005; Casagrande et al. 2006, 2010).

The above methods are indirect which means that they require model dependencies. In lack of direct methods applicable to most stars, we have to rely to them for the parameter determinations.

The different analysis techniques often yield significant differences in their results (e.g., Torres et al. 2008; Bruntt et al. 2012; Molenda-Żakowicz et al. 2013). These systematic errors are difficult to assess and are usually the main error contributors within a study. Such problems can be mitigated by a uniform analysis that will yield the precision needed.

1.5 This work

In this thesis, we will focus on the derivation of photospheric stellar parameters for solar-type stars. The technique can be applied to both high and medium resolution spectroscopy. The first Chapters describe the method based on the ionization and excitation balance of iron. The EW method built by our team was problematic for stars with low $T_{\rm eff}$ (below 5000 K). Our goal was to optimize this method for the cooler stars and re-derive their correct stellar parameters.

In the second part of the thesis we use another spectroscopic technique, namely spectral synthesis. We describe the principles of our methodology (e.g., code, procedure). Our aim is to provide stellar parameters for stars where the EW technique is not effective. We have applied this new method to stars with moderate and high rotation. This could be the case of transit planet hosts since the transit technique is not limited by stellar rotation, at least in first approach. Planet hosts with moderate and high rotation were analyzed with our method and their planetary parameters were revised.

CHAPTER 2

Spectroscopic stellar parameters - EW method

"It's a dirty job but someone has to do it."

Anonymous

In this section, we describe the procedure to derive stellar parameters for solar-type stars by measuring the equivalent widths (EW) of iron lines and by forcing the ionization and excitation balance. The theory behind this procedure is depicted in detail in Gray (2005).

2.1 The equivalent width

An important characteristic of FGK stars is the presence of many absorption features in their spectra because the atoms and molecules are not fully ionized. A common approach to derive atmospheric parameters for these spectral types is to exploit the large number and properties of the iron lines. In optical spectra iron lines are the most numerous with well-studied atomic transitions that make the abundance determination easier compared to other elements.

Usually, we refer as metallicity to the amount of iron content in a star. This is not strictly correct as for example, in the Sun, there are more abundant elements than

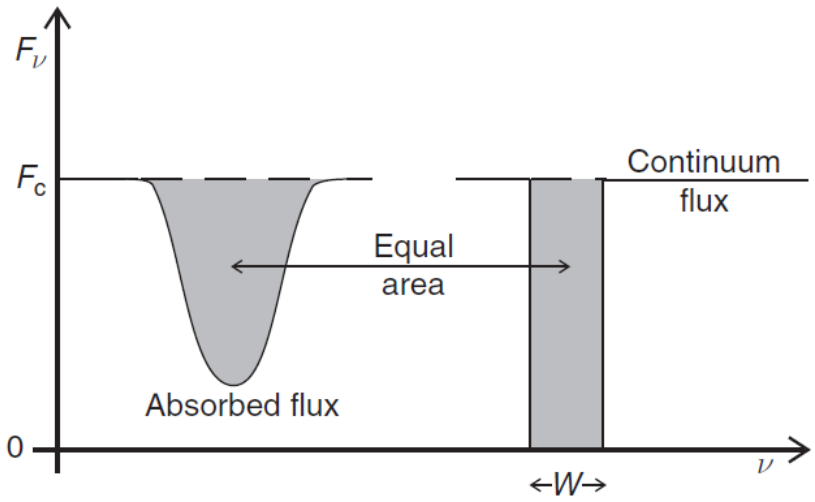

Figure 2.1: A simple depiction of the equivalent width. Taken from Pradhan & Nahar (2011).

iron (C, N, O, Ne, Mg, and Si). However, the overall metallicity correlates with iron abundance for field stars (Bodaghee et al. 2003; Gilli et al. 2006) and if we exclude the chemically peculiar stars, we can safely assume iron as a proxy for the overall metallicity.

The EW of a spectral line provides a measure of its strength. The EW forms a rectangle with a height equal to that of the continuum and a width such that the area of the rectangle is equal to that absorbed by the spectral line (Fig. 2.1). The mathematical description is given below:

$$EW = \int_{-\infty}^{+\infty} \frac{F_c - F_\lambda}{F_c} d\lambda, \tag{2.1}$$

where F_c is the flux of the continuum and F_λ is the line flux at each wavelength λ. The strength of the line depends on the atomic transition, the absorption coefficient, and the number of absorbers which in turn, depend on temperature, electron pressure and atomic constants (see more in the following Sections).

2.2 The temperature dependence

The spectral line strength is strongly correlated with temperature mostly due to the dependence on the ionization and excitation processes described below. We assume that the standard thermodynamic relations hold locally, despite the temperature and pressure gradients in the atmosphere, as described by the local thermodynamic equilibrium (LTE) approximation. In this regime, we consider that collisions (rather that radiation) dominate the excitation of the atoms, which is a good approximation in the case of FGK

atmospheres. We can express the ratio between the number of atoms in an energy level n and the total number of the atoms of that species as:

$$\frac{N_n}{N} = \frac{g_n}{u(T)} 10^{-\Theta(T)\chi_n}, \tag{2.2}$$

where N_n is the population of energy level n, N is the total number of atoms, g_n is the degeneracy of level n, χ_n is the excitation potential of the same level, T is the temperature, $\Theta(T) = 5040/T$, $u(T) = \sum g_i e^{-\chi_i/kT}$ is the partition function, and k is the Boltzmann constant.

Similarly, the ionization for the collision-dominated gas can be calculated using the Saha Equation:

$$\begin{aligned} \frac{N_{i+1}}{N_i} &= \frac{\Phi(T)}{P_e} \\ \Phi(T) &= \frac{(\pi m_e)^{3/2}(5kT)^{5/2}}{\hbar^3} \frac{u_{i+1}(T)}{u_i(T)} e^{-I/kT} \end{aligned} \tag{2.3}$$

where the N_{i+1}/N_i is the ratio of the total populations of atoms in two ionization states, i and $i+1$, the $u_{i+1}(T)/u_i(T)$ is the ratio of partition functions, m_e is the electron mass, $\hbar$ is the reduced Planck constant, P_e is the electron pressure, and I is the ionization potential.

The typical behavior of a weak, metal line with effective temperature is shown in Fig. 2.2, for neutral and ionized species. In the atmospheres of FGK dwarfs, most metals are singly ionized and therefore, the dependence of the EW with $T_{\rm eff}$ is presented by Case 2 (neutral species, where element is mostly ionized) and Case 4 (ionic species, where element is mostly ionized). In the same Figure, Case 1 depicts the behavior of the EW of neutral species with the element mostly neutral and Case 4, of ionized species where the element is mostly ionized.

The strength of a weak line (R) is proportional to the ratio of the line to continuous absorption coefficients and is defined as:

$$R = \frac{F_c - F_\lambda}{F_c} = \text{constant} \frac{\mathrm{l_v}}{\kappa_\mathrm{v}}, \tag{2.4}$$

where F_c is the flux of the continuum, F_λ is the line flux at each wavelength λ, l_v is the line absorption coefficient, and κ_v the continuous absorption coefficient (see Chapter 4 for a definition of the latter parameters). The strength of a weak line has a direct connection with the EW as seen from Equation 2.1.

The fractional change of R with temperature (T) shows its sensitivity to T. The behavior of a neutral species is described as:

$$\frac{1}{R}\frac{dR}{dT} = \frac{\chi + 0.75 - I}{kT^2}, \tag{2.5}$$

where the sensitivity to temperature depends on the lower-level excitation potential of

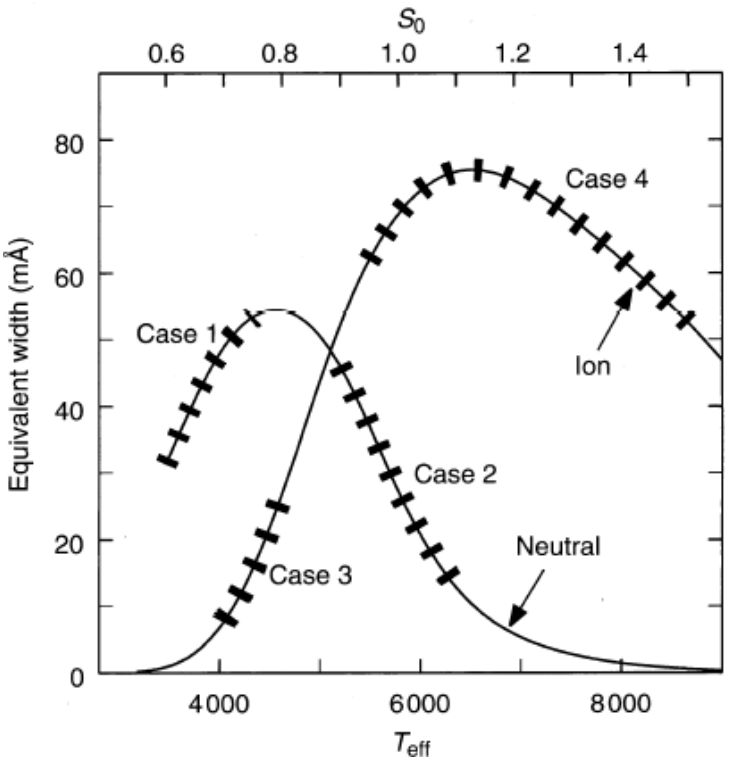

Figure 2.2: The EW dependence with effective temperature. $S_0 = 1.0$ refers to the solar value of $T_{\rm eff}$ (=5777 K). Taken from Gray (2005).

the line (χ). For solar-type stars, usually $\chi + 0.75 < I$ for metals, therefore, the EW of neutral species decreases with with increasing temperature. An effective way to constrain the stellar temperature is to use the excitation equilibrium of neutral lines of different χ.

For ionic species, the dependence has an extra dependence on the electron pressure:

$$\frac{1}{R}\frac{dR}{dT} = \frac{2.5}{T} + \frac{\chi + 0.75}{kT^2} - \Omega. \tag{2.6}$$

where Ω can be considered as a constant as it mildly depends on pressure. Ionic species show smaller sensitivity to temperature changes, except for those with high excitation potential. The temperature dependence for strong lines should include the damping constants.

2.3 The pressure dependence

Pressure dependence in stellar atmosphere can be related to gravity dependence. For FGK stars, an increase in the surface gravity compresses the photosphere, resulting in an

increase in pressure (both electron and gas). The electron pressure is much smaller than the gas pressure because hydrogen, as a main electron contributor, is not fully ionized. An empirical approximation of gas pressure (P_g) in dependence with gravity (g) is given for cool stars:

$$P_g \approx \text{constant}\, \mathrm{g}^{2/3} \tag{2.7}$$

Also, electron pressure (P_e) is described by:

$$P_e \approx \text{constant}\, \mathrm{g}^{1/3} \tag{2.8}$$

In solar-type stars, where the elements are mostly ionized, $N_n \ll N_{n+1}$ and the total number of atoms, N, equals to N_{n+1}. From the Saha equation (Equation 2.3), we obtain $N_n = \text{constant}\, P_e$. The line strength for neutral atoms is:

$$R = \frac{l_v}{\kappa_v} \approx \frac{\text{constant}\, \mathrm{N_n}}{\text{constant}\, \mathrm{P_e}} \approx \frac{\text{constant}\, \mathrm{P_e}}{P_e} \approx \text{constant}. \tag{2.9}$$

Therefore, neutral atoms are insensitive to pressure changes.

For first ions, we have the opposite population, $N_{n+1} = N$. The line strength for ions becomes:

$$R = \frac{l_v}{\kappa_v} \approx \frac{\text{constant}\, \mathrm{N}}{\text{constant}\, \mathrm{P_e}} \approx \frac{\text{constant}}{g^{1/3}}. \tag{2.10}$$

Obviously ions are pressure sensitive, with lower pressure causing stronger lines.

In addition, the wings of strong lines are good pressure indicators. This sensitivity arises from the pressure dependence of the damping parameters, namely the van der Waals and Quadratic Stark constants (see Chapter 4).

2.4 The abundance dependence

As the abundance increases, line strength also increases but not always linearly. The dependence of the EW with the abundance is described by the curve of growth, as shown in Fig. 2.3, and is divided into three different regimes. The first one corresponds to the behavior of weaker lines, where the Doppler core dominates and the EW is proportional to the abundance A. The second phase begins when the central depth approaches the maximum value. The line saturates and grows asymptotically towards a constant value. The third one starts as the optical depth of the line becomes significant compared to the absorption of the continuum and the wings dominate the line profile. In this case, the EW is proportional to the square root of the abundance.

It is clear that for abundance determinations, we want to select weak lines that fall on the linear part of the curve of growth, where the EW is more sensitive to abundance changes.

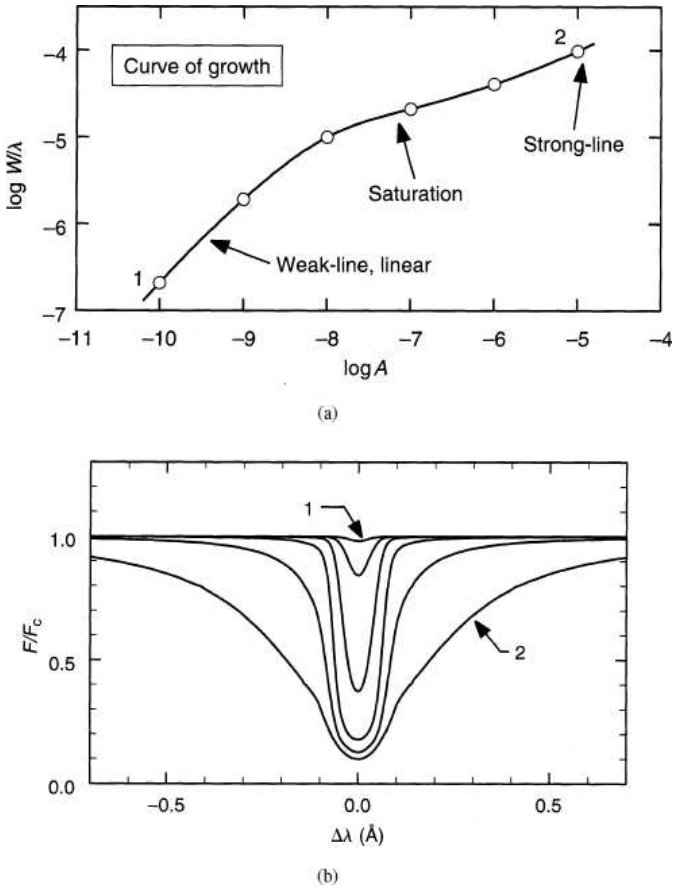

Figure 2.3: a) Typical curve of growth from a model photosphere: the reduced EW versus abundance (A). b) Line profile change with chemical abundance of the absorption species. The dots in (a) correspond to the different profiles in (b). Taken from Gray (2005).

2.5 Microturbulence

Microturbulence (ξ_t) is a parameter that describes the small-scale mass motions in dimensions of the optical depth. The velocities due to these motions produce Doppler shifts analogous to the thermal motions and are postulated by Gaussian distributions. Therefore, absorbers have additional turbulent velocities than the thermal ones, causing broadening with a wavelength shift of $\Delta\lambda$,

$$\Delta\lambda = \frac{\lambda}{c}\left(\frac{2kT}{m} + \xi^2\right)^{1/2}, \tag{2.11}$$

where λ is the central wavelength, T temperature, k Boltzmann constant. This shows that the line affected by ξ_t is broadened as if the temperature is increased.

In the abundance analysis, microturbulence is introduced to reconcile differences between the observed EW of saturated lines and the ones predicted from the classic

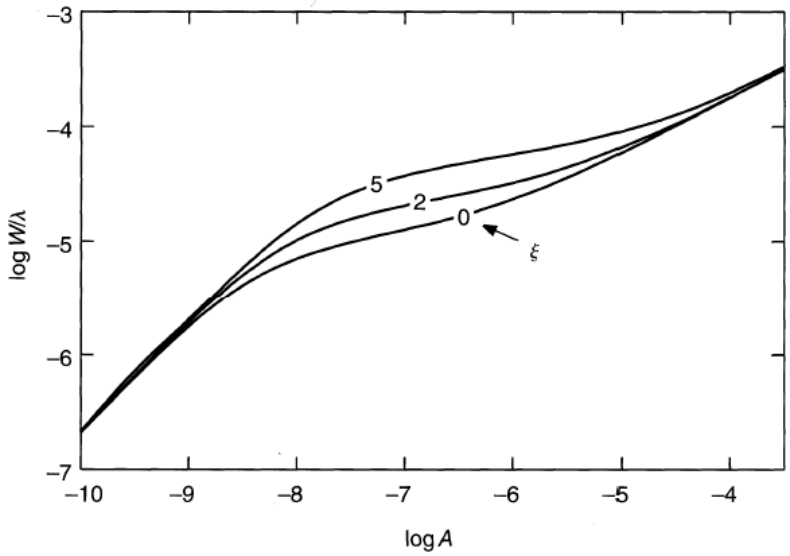

Figure 2.4: Curve of growth for different values of microturbulence. Taken from Gray (2005).

one-dimensional models (static and radial). The mechanism that is believed to be responsible for this observed velocity is convection, both in low-mass stars and massive stars. Figure 2.4 shows that the presence of ξ_t causes a delay in saturation. The observational data show a dependence of ξ_t on both effective temperature and on surface gravity (e.g., Nissen 1981; Reddy et al. 2003; Allende Prieto et al. 2004; Adibekyan et al. 2012a; Ramírez et al. 2013).

2.6 Model atmospheres

The spectroscopic techniques for parameter determinations are model dependent. This means that a model photosphere has to be constructed under some assumptions in which temperature and pressure are calculated as a function of the optical depth. In particular, a model atmosphere describes the depth-dependence of basic physical quantities: opacity at some reference frequency, electron temperature, electron pressure, gas pressure, abundances of different elements. The computation of a model atmosphere is simplified under the certain assumptions (see more in Sect. 4.1):

- Homogeneous plane-parallel layers

  The geometrical thickness of a stellar atmosphere is sufficiently small compared to the stellar radius. In case of the Sun, geometrical thickness of the photosphere is less than 0.1% in ratio. The plane-parallel assumption is appropriate for most main-sequence and giant stars, but will fail for the super giants, where they have large atmospheric extensions (>5%), or for stars with fast expanding envelopes. Homogeneity in the atmosphere requires that the physical quantities vary only

with depth and magnetic fields, star spots and granulation are ignored.

- Hydrostatic equilibrium

  Hydrostatic equilibrium may also be assured for main-sequence and giant stars. The atmospheres of these stars do not show large-scale gas motions such as expansion or contraction. Gravity determines the pressure profile, assuming a star at equilibrium or not in a quickly evolving evolutionary stage.

- Time independent

  The atmosphere is stationary and the properties do not change with time. The phenomena such as rotation, pulsation, expanding envelopes, variable magnetic fields, etc. are neglected. In this case, the radiative transfer equation has no time dependence (see Sect. 4.1).

- Radiative equilibrium

  Radiative equilibrium states that the bolometric flux in a plane-parallel atmosphere is constant. In some stars, particularly in late-type stars, convective energy transportation becomes important and we need to take into account.

- Local thermodynamic equilibrium

  As we mentioned in Sect. 2.2, it is assumed that all thermodynamic properties in a small volume have the thermodynamic equilibrium values at the local values of temperature and pressure. A system is in LTE if the local kinetic temperature is equal to the Planckian temperature of the radiation field.

Usually, a model atmosphere is presented in a tabular form where some physical properties, such as local temperature, pressure, and density are listed for each atmospheric layer. The optical depth (i.e. the layers of the atmosphere) is normally chosen at a wavelength in the visible region of the spectrum, e.g. at 5000 Å.

In the literature there are many atmospheric models precomputed in grids for a set of stellar parameters (e.g., ATLAS - Kurucz 1993, MARCS - Gustafsson et al. 2008).

2.7 The procedure for the EW method

The standard determination of spectroscopic parameters ($T_{\rm eff}$, [Fe/H], $\log g$, and ξ_t) for solar-type stars starts by measuring the EW of selected and well-defined absorption lines. Then we translate these measurements into individual line abundances, assuming a given atmospheric model. We obtain the correct stellar parameters by imposing excitation and ionization balance for the iron species.

The procedure of the standard method is shown in Fig. 2.5. The main steps are identified below:

- First, we define a list of neutral and ionized iron lines. For these lines precise atomic data are needed.

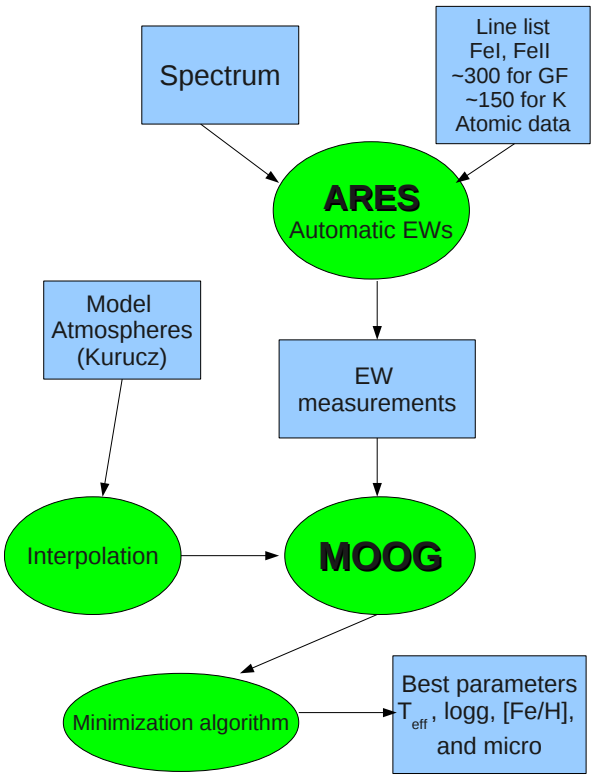

Figure 2.5: A schematic of the standard procedure.

- The EW of the selected lines should be measured precisely. The uncertainties of the EW depend on the determination of the continuum position, the signal-to-noise (S/N) of the data, the presence of blended lines, or any unexpected spectral feature, such as cosmic rays hits. Typical uncertainties of the EW values are of 2-5% for S/N ∼100.

- A stellar atmospheric model is interpolated from a grid of precomputed models for a set of initial stellar parameters.

- The abundances of individual iron lines are computed.

- The best parameters are obtained when the Fe I abundance shows no dependence on the excitation potential (excitation balance) and on the reduced equivalent width. Additionally, the mean abundances given by Fe I and the Fe II must be the same (ionization balance) and consistent with those of the input model atmosphere.

2.7.1 The line list and atomic data

The selection of the lines is crucial for the accuracy and precision of this method. Some authors use large sets of lines aiming to increase the statistical strength of the derived spectroscopic stellar parameters, e.g., the line list for the Gaia-ESO survey, hereafter GES (Heiter et al., in prep.). Others use a reduced and very well-defined set of lines adapted for specific type of stars, e.g., Hekker & Meléndez (2007) use a line list for giant stars. An effective approach to identify the lines with the best atomic data is described in Sousa et al. (2008) and in Sousa et al. (2014).

A reliable line list is comprised of lines that can be accurately measured, which usually means unblended lines. This is the main reason why this technique is limited to slowly rotating stars. Rotation causes line broadening which in turn, is responsible for blending. In addition, lines must be unsaturated, cover a wide range in excitation potential and have accurate atomic data.

The atomic data are required for the calculation of the line opacities. There are great efforts of improving atomic and molecular line data in recent databases (e.g., the Vienna Atomic Line Database[1] - Piskunov et al. (1995); Kupka et al. (1999, 2000). Many transitions have been analysed in the laboratory, leading to a large number of accurate line positions, and molecular constants. However, line strength information is often missing, and lines involving highly excited states are not visible in the laboratory, but are important in warm astrophysical environments like stellar atmospheres.

An effective way to solve for inconsistencies in the atomic data is to calibrate them with respect to the Sun. In this case, for all the solar lines, we only vary the atomic parameters so that each line reproduces the abundance equal to solar abundance. The stellar parameters are obviously fixed to the standard solar values.

2.7.2 Measurement of the EW

All fundamental stellar parameters are correlated, some stronger than others, with the equivalent width. Therefore, one has to be very precise and accurate in the measurement of the EW. Manual measurements (using interactive routines such as *splot* of IRAF) are possible but when we are dealing with long line lists or large sample of stars, this approach is far from practical or efficient. Additionally, the manual measurements are highly subjective that could cause inhomogeneity in the results.

At present, there are many automatic codes (Sousa et al. 2007; Stetson & Pancino 2008; Kang & Lee 2012, to name a few) that provide fast and reliable measurements of the EW. In our analysis, we use the Automatic Routine for line Equivalent widths in stellar Spectra[2] (ARES - Sousa et al. 2007) code that was build by our team.

ARES computes the EW locally (the interval is defined by the user) around each line of the input list. The continuum position is obtained iteratively by choosing local continuum points and is defined by the parameter *rejt*. The *rejt* parameter is set by the user as the calibration of the continuum position and is strongly dependent on the S/N

[1] http://vald.inasan.ru/∼vald3/php/vald.php
[2] http://www.astro.up.pt/∼sousasag/ares

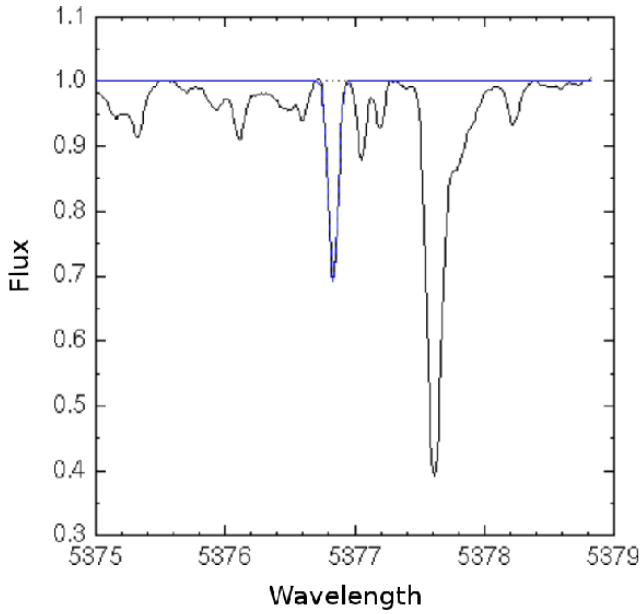

Figure 2.6: A Gaussian fit (blue line) of a spectral line (black line) as given by ARES. The black dots represent the continuum points and the x-axis the wavelength in Å.

value of the spectra. A table with typical *rejt* values in dependence with the S/N is presented in Mortier et al. (2013a). To calculate the EW, ARES fits the absorption lines with Gaussian profiles. This is a very good approximation for weak lines (below 150 mÅ). For stronger lines the Gaussian profile is unable to fit the wings of the lines and a Voigt profile is required. The center of the lines are calculated using the mathematical properties of the derivatives of the Gaussian function.

In Fig. 2.7, we present from Sousa et al. (2007) the agreement between the EW calculated by ARES and manually for a sample of HARPS stars.

2.7.3 Calculating the abundances - MOOG

For our analysis, we use the MOOG[3] package (Sneden 1973) that performs a variety of LTE line analysis and spectrum synthesis tasks. MOOG uses the equivalent widths to calculate the individual line abundances. This task is performed by the *abfind* driver.

The model atmospheres are formatted in a grid of Kurucz Atlas 9 plane-parallel, 1D static model atmospheres (Kurucz 1993). The interpolation from the grid is calculated from a spline bicubic function for temperature and from a geometric mean for surface gravity and metallicity. The general steps to find the best parameters are listed below and are visually depicted in Fig. 2.8:

- The effective temperature has a strong influence on the correlation of iron abun-

[3]http://verdi.as.utexas.edu/moog.html

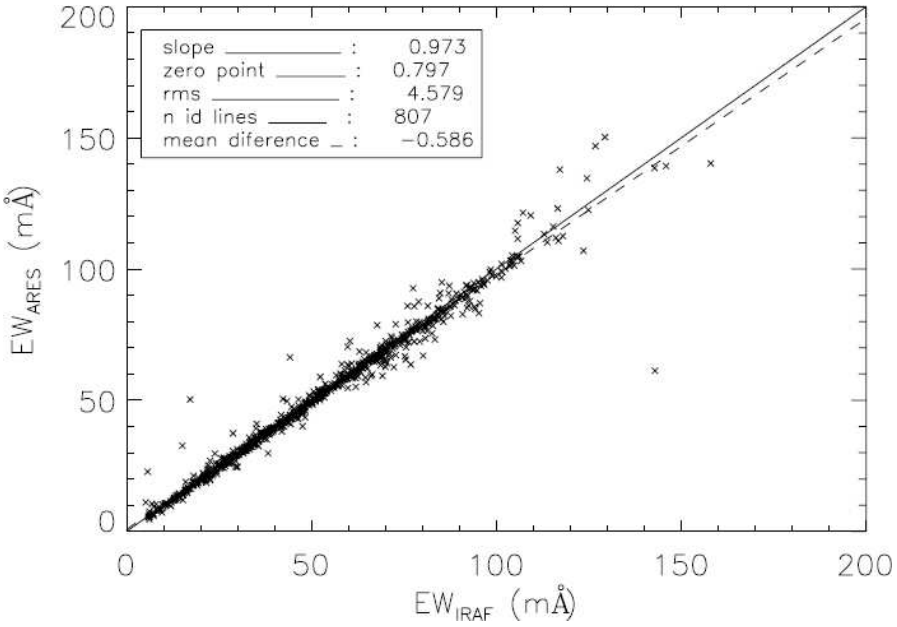

Figure 2.7: Results of ARES for a sample of HARPS spectra comparing the value of the EW obtained by ARES (EW_{ARES}) with the manual value from IRAF (EW_{IRAF}) (Sousa et al. 2007).

dance with the excitation potential (excitation balance). We obtain the $T_{\rm eff}$ when Fe I abundance shows no dependence on the excitation potential, i.e., the slope of abundance versus excitation potential is zero.

- Surface gravity is derived from the ionization balance of both Fe I and Fe II abundances. Therefore, the abundances of neutral iron should be equal to the abundance of ionized and consistent with the one of the input model atmosphere.

- Microturbulence is connected with the saturation of the stronger iron lines. The value of ξ_t has to derive the same abundances for weak and strong lines. Iron abundances should show no dependence on the reduced equivalent width, i.e. the slope of abundance vs the reduced EW is zero.

The optimal parameters are found with an iterative minimization code based on the Downhill Simplex Method (Press et al. 1992), making the total procedure automatic. The minimization procedure satisfies the excitation and ionization equilibrium conditions. The obtained solution is independent of the initial set of parameters employed, hence, we used the standard solar values as initial input values ($T_{\rm eff} = 5777\,\mathrm{K}$, $\log g = 4.44\,\mathrm{dex}$, $\xi_t = 1\,\mathrm{km\,s^{-1}}$).

This technique (ARES+MOOG) has been successfully applied to characterize large samples of solar-type stars. For instance, Adibekyan et al. (2012c) derived chemical abundances of refractory elements for a sample of 1111 stars using stellar parameters with the method described above (Fig. 2.9). In addition, Sousa et al. (2008, 2010) used

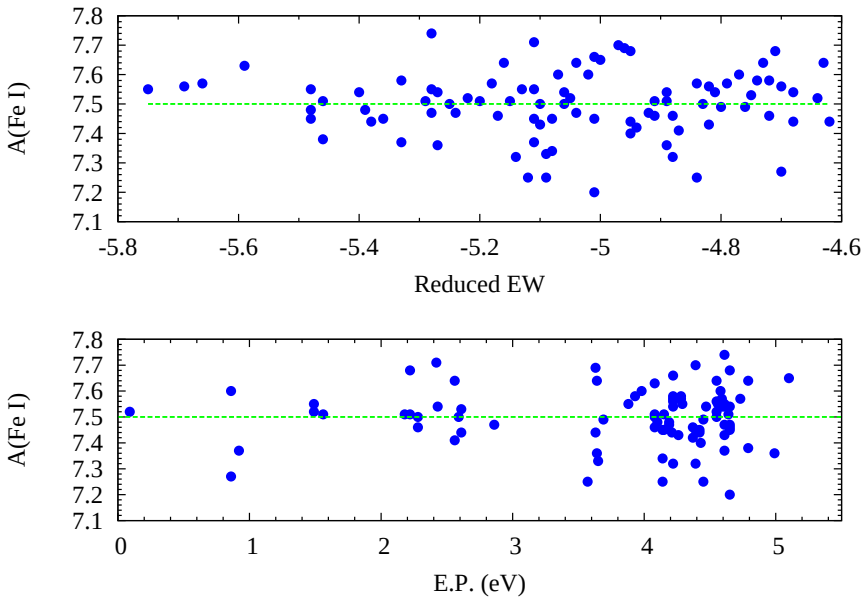

Figure 2.8: The Fe I abundances of HD 21749 versus the excitation potential, E.P. (upper panel) and the reduced EW (lower panel). The absolute abundance of the star is 7.50 dex with a scatter of 0.03 dex and the slope in both plots is zero and indicates the non-dependence of the Fe abundance on the x-axes.

the same technique to derive parameters for stars of the HARPS GTO planet search program.

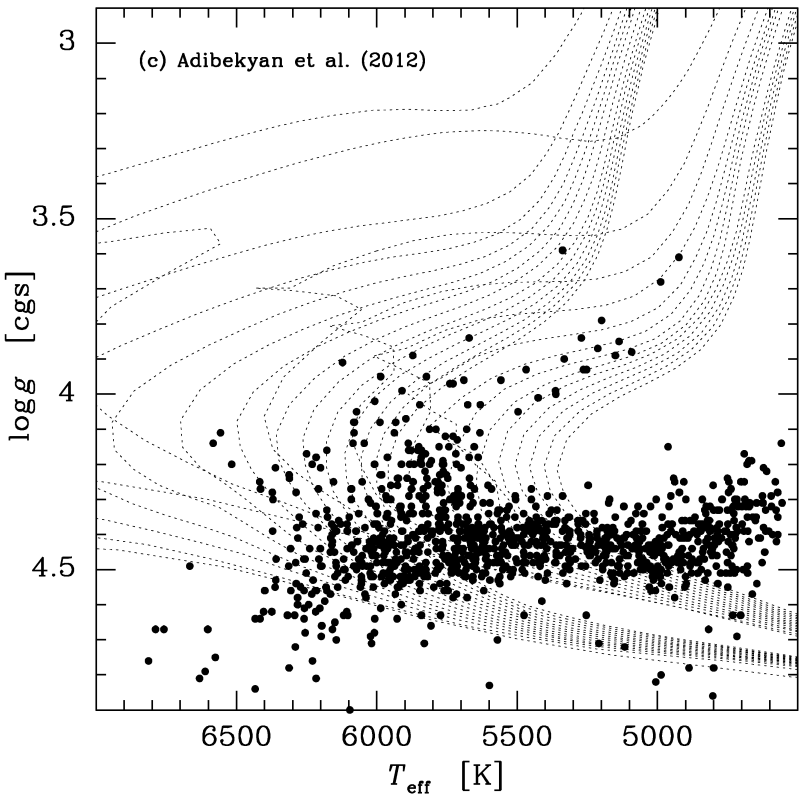

Figure 2.9: HR diagram for the Adibekyan et al. (2012c) sample. The α-enhanced Yonsei-Yale (Y2) isochrones have metallicities of [Fe/H] = -1 and +0.3 dex, respectively, and are shown from 1 to 15 Gyr in steps of 1 Gyr. A typical error for $T_{\rm eff}$ is $\pm$30 K and for $\log g$ $\pm$0.06 dex.

CHAPTER 3

Stellar parameters for cool stars

"Να κατεβουν οι αγγελοι να
χορεψουν τσιφτετελι"

K. Ferris

In this Chapter, I describe the problem of cool stars in the determination of mainly the effective temperature. This work led to a publication (Tsantaki et al. 2013). In the final section of this Chapter, I present some applications of this work where it has already been used in the community.

3.1 Introduction

The study of the $H\alpha$ and $H\beta$ wings (e.g., Fuhrmann 2004), the excitation balance of iron lines (e.g., Santos et al. 2004), spectral synthesis techniques (e.g., Valenti & Fischer 2005), line ratios (or line depth ratios) (e.g., Gray 1994) are the basic spectroscopic techniques that along with other techniques, such as photometry and interferometry can be used for the determination of the effective temperature. A comparison between these different methods can show considerable discrepancies in their results, such as the large differences reported between spectroscopic parameters and those in the Kepler Input Catalog (Bruntt et al. 2012; Thygesen et al. 2012). Even in the restricted group of

solar-type stars, the effective temperatures obtained with these methods can differ significantly (e.g., Kovtyukh et al. 2003; Ramírez & Meléndez 2004; Casagrande et al. 2006; Sousa et al. 2008; Molenda-Żakowicz et al. 2013). A comparison of different methods is shown in Fig. 3.1, where the authors compared four different methods of parameter determinations for a sample of 169 solar-type stars finding considerable differences in their results (Molenda-Żakowicz et al. 2013). For instance the mean differences in $T_{\rm eff}$ between spectroscopic (ROTFIT - Frasca et al. 2003, ARES+MOOG - Sousa et al. 2007, 2008, VWA - Bruntt et al. 2012) and photometric methods (IRFM - Pinsonneault et al. 2012) are $\sim$100 K.

The temperature determination becomes more difficult when we focus on K-type stars. Part of the difficulties in the stars with $T_{\rm eff} < 5000$ K emerge from their line crowed spectra that cause strong blending. Blending can be a considerable problem if one uses the technique based on the iron EWs. The spectral lines cannot be easily resolved and the continuum placement becomes more difficult, causing bad measurement of the EWs and hence, makes the calculation of stellar parameters ambiguous (Fig. 3.2). Therefore, it is important to carefully select the iron lines in such manner that will eliminate the blending effects. In addition, the choice of the atomic parameters influences the abundance determination. Some authors calculate the atomic parameters using the Sun as a reference to avoid the errors that emerge from the theoretical or laboratory values. For instance, an error of 5% in the atomic parameters, namely the oscillator strength, propagates to a 2% error in $T_{\rm eff}$ (Allende Prieto et al. 1998). In that way, the atomic parameters for stars that are different from the Sun, i.e. too hot or too cool are no longer accurate enough.

Sousa et al. (2008) (hereafter SO08) performed a spectroscopic analysis for a sample of solar-type stars. This sample is part of the High Accuracy Radial velocity Planet Searcher (HARPS) guaranteed time observations (GTO) survey that is composed of slow rotators and low activity FGK stars in order to detect low-mass planets. A comparison of these spectroscopic results with the infrared flux method indicates a disagreement in the effective temperatures only for the cooler stars of the sample with temperatures below ~ 5000 K. Figure 3.3 shows the effective temperatures derived by the spectroscopic analysis and the IRFM in the work of SO08. To recover the bolometric flux that is missing from the multi-band photometry for the IRFM, the authors used two different models: 1) the ATLAS9-ODFNEW models (Castelli & Kurucz 2004) (upper panel), and 2) the Phoenix models (Brott & Hauschildt 2005) (bottom panel).

Motivated by that, we compile an optimized line list to improve the accuracy of the stellar parameters for the cooler stars and compare our results with other independent methods (IRFM, interferometry).

3.2 Stellar sample and previous spectroscopic analysis

The stellar sample, presented in SO08, is composed of 451 stars as part of the HARPS high-precision GTO program at the ESO La Silla 3.6m telescope with the objective to detect low-mass exoplanets with high radial velocity accuracy (Mayor et al. 2003). It

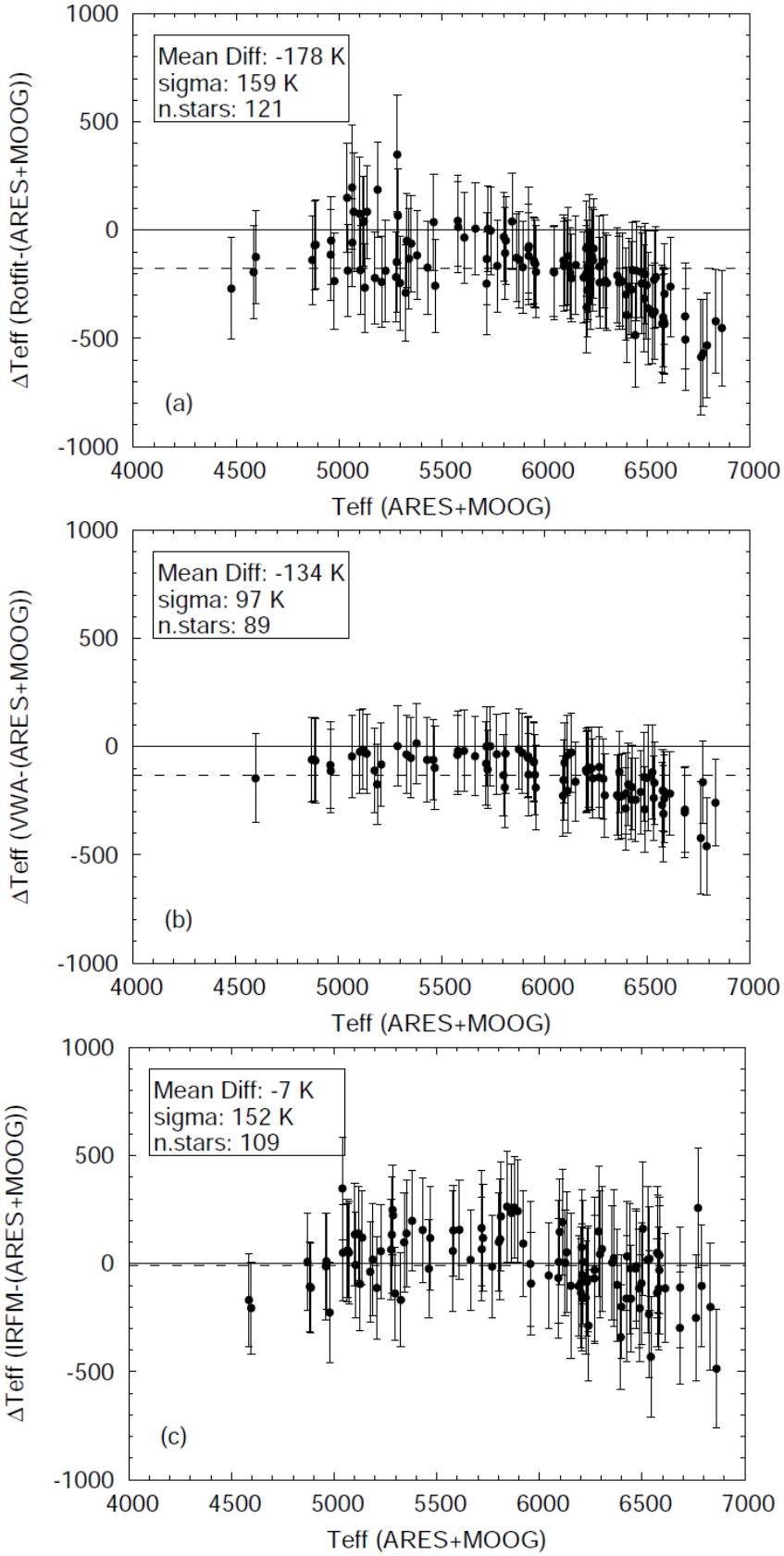

Figure 3.1: Comparison of $T_{\rm eff}$ values measured with four different methods from Molenda-Żakowicz et al. (2013): ROTFIT and ARES+MOOG (Molenda-Żakowicz et al. 2013), VWA (Bruntt et al. 2012; Thygesen et al. 2012) and IRFM (Pinsonneault et al. 2012). In the insets, the mean difference between the compared sets of data, the standard deviation of the mean, and the number of stars in common are given.

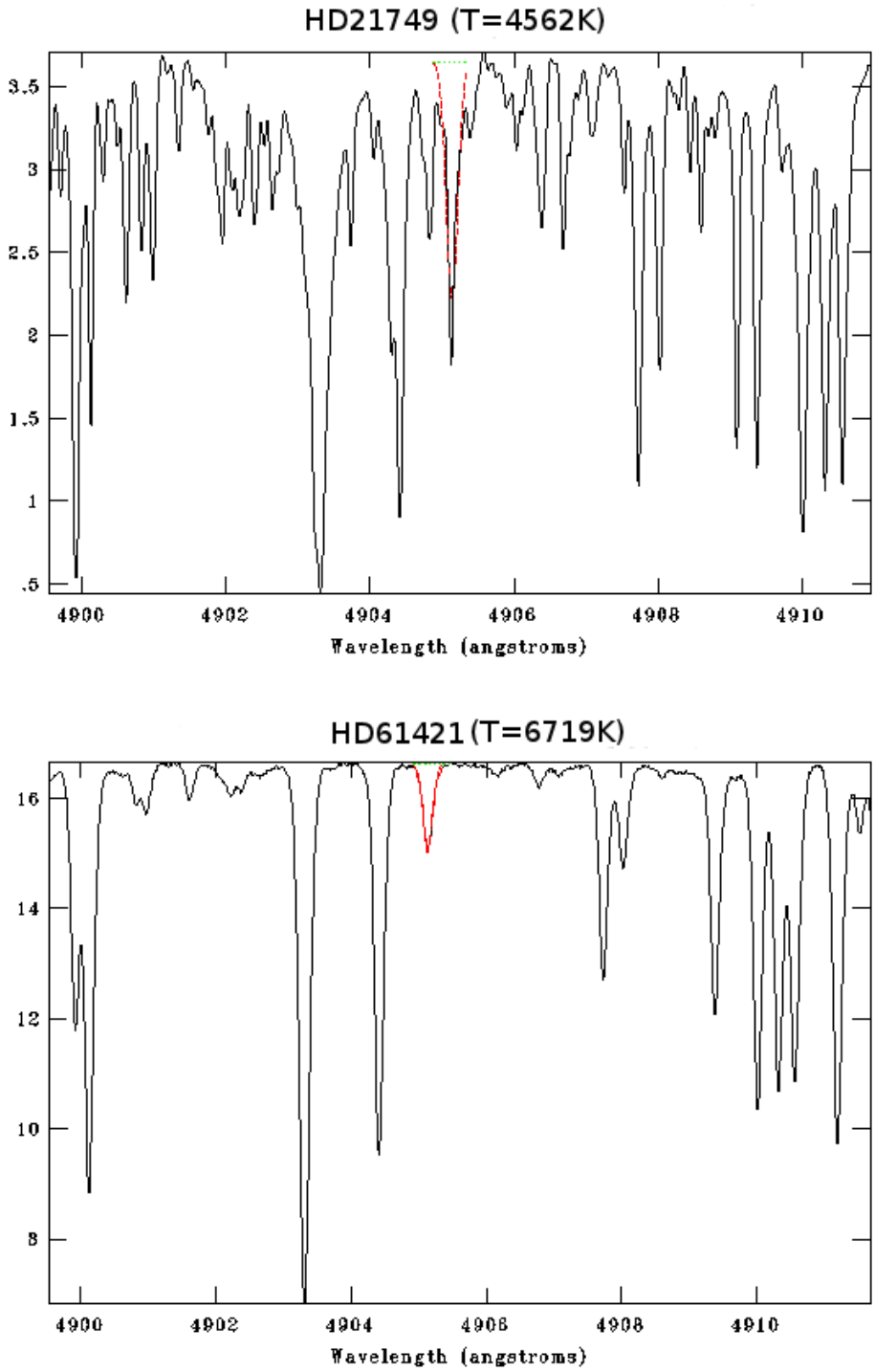

Figure 3.2: Depiction of a cool and a hot spectrum for the same wavelength interval of stars with similar metallicity and gravity. Cooler spectra are more line crowded and the continuum is not well defined.

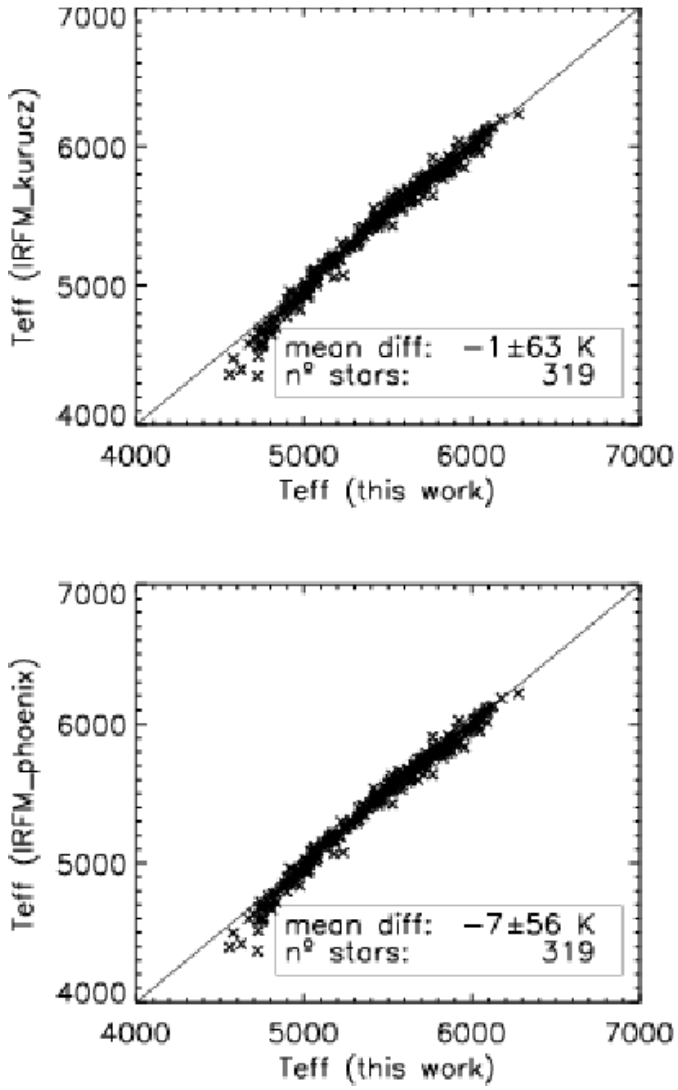

Figure 3.3: Comparison for the effective temperature with the EW method of Sousa et al. (2008) and with the IRFM using either the Kurucz (upper panel) or Phoenix models (bottom panel).

Table 3.1: Characteristics of the sample and the reference star, described in SO08.

	$T_{\rm eff}$ (K)	$\log g$ (dex)	$[Fe/H]$ (dex)	$Mass$ $M_{\odot}$
Lowest value	4556 ± 98	3.68 ± 0.05	-0.84 ± 0.01	0.37
Highest value	6403 ± 65	4.62 ± 0.03	0.39 ± 0.05	1.42
HD 21749	4723 ± 143	4.40 ± 0.33	-0.02 ± 0.08	0.76

is mainly comprised of dwarf FGK stars selected from a volume-limited sample of the CORALIE survey (Udry et al. 2000). Planet hosts from the southern hemisphere were also added to this sample, forming in total a sample of 451 stars. These stars are slowly-rotating, non-evolved, and low-activity stars, with apparent magnitudes that range from 3.5 to 10.2 and have distances of less than 56 parsec. The spectral resolution is of R $\sim$ 110,000 and 90% of the combined spectra have S/N higher than 200. We point to SO08 for more details.

For this sample, SO08 derived stellar parameters by imposing excitation and ionization equilibrium, based on the measurements of weak iron lines. This method is very effective for FGK stars due to the numerous iron lines in their spectra. Iron abundance is used as a proxy for the overall stellar metallicity.

The line list for their spectroscopic analysis, was composed of 263 Fe I and 36 Fe II lines. The EWs of the lines were measured automatically with ARES. The atomic parameters of the iron lines, namely the oscillator strength values ($\log gf$), were computed by an inverted solar analysis, using a solar model with $T_{\rm eff}$ = 5777 K, $\log g$ = 4.44 dex, ξ_t= 1.0 m s^{-1}, $\log_{\epsilon}$(Fe) = 7.47 dex.

The spectroscopic analysis was completed assuming LTE, and using the 2002 version of the abundance determination code MOOG and a grid of Kurucz Atlas 9 model atmospheres. Some characteristics of the sample are depicted in Table 3.1, as described in SO08.

There are different sources of uncertainties that occur in the stellar parameter determination using this method. These errors can be attributed to the uncertainties of the measurements of the EWs, the uncertainties in the atomic parameters and the uncertainties that are intrinsic to the method of ionization and excitation equilibrium. In addition, systematic errors can arise due to the assumptions of the method, such as 1D static atmospheres, NLTE effects (Mashonkina et al. 2011; Bergemann et al. 2012). However, departures from LTE for Fe lines do not affect their abundance determinations for near solar metallicity dwarfs but should be taken into consideration for more evolved or very metal-poor stars (Lind et al. 2012; Ruchti et al. 2013) that are not part of this sample.

Errors in the measurements of the EWs can be minimized by using high quality spectra. In low S/N spectra, weak lines cannot be distinguished from noise and strong

Table 3.2: Mean errors in the parameters when dividing them in temperature ranges.

Temperature range	$T_{\rm eff}$ (K)	$\log g$ (dex)	ξ_t ($\rm km\,s^{-1}$)	$[Fe/H]$ (dex)
$T_{\rm eff} < T_{\rm eff\odot}$ - 300 K	51	0.13	0.23	0.05
$T_{\rm eff\odot}$ - 300K $< T_{\rm eff} < T_{\rm eff\odot} + 300$ K	18	0.05	0.03	0.01
$T_{\rm eff\odot} + 300$ K $< T_{\rm eff}$	30	0.07	0.05	0.02

lines can be underestimated due to the miscalculation of their wings. The high resolution and high S/N spectra used for this sample, are the best solution to deal with such errors. Since in our spectroscopic analysis the atomic data ($\log gf$) are derived with respect to the Sun, we expect small errors for solar analogs but more significant for cooler and hotter stars. For example, if we divide the sample of SO08 in three temperature groups: [$T_{\rm eff} < T_{\rm eff\odot}$ - 300 K], [$T_{\rm eff\odot}$ - 300 K$< T_{\rm eff} < T_{\rm eff\odot} + 300$ K], and [$T_{\rm eff\odot} + 300$ K $< T_{\rm eff}$], the respective mean errors are shown in Table 3.2[1].

The errors in the atmospheric parameters are estimated in a similar way as in Neuforge-Verheecke & Magain (1997) and Gonzalez & Vanture (1998) by varying each parameter (temperature, surface gravity and microturbulence) by their typical error. The error in ξ_t is determined from the standard deviation in the slope of the least-squares fit of Fe I abundance versus reduced equivalent width. The error in $T_{\rm eff}$ is determined from the error in the slope of the least-squares fit of Fe I abundance versus χ derived from the standard deviation in the slope and from the error in ξ_t. The error in $\log g$ comes from the contribution from the error in Fe II abundance due to the error in $T_{\rm eff}$ and the scatter in the Fe II abundances (measured as $\sigma/\sqrt{N}$, σ is the standard deviation and N the number of lines). The error in the Fe abundance is a combination of the errors in Fe I abundance due to $T_{\rm eff}$, ξ_t, and the scatter of the individual Fe I abundances, added in quadrature. The use of many iron lines can reduce this type of uncertainty, assuming that the majority of the lines are of good quality.

3.3 Building a stable line list for the cooler stars

A reliable line list is comprised of lines that can be accurately measured, which usually means unblended lines. In addition, lines must be unsaturated, cover a wide range in excitation potential and have accurate atomic data. Temperature, as well as the other stellar parameters, is strongly correlated with the EW. This sensitivity emerges from the excitation and ionization processes that follow the exponential and power dependencies with temperature that are defined by the well-known Boltzmann and Saha equations.

For the cooler stars line blending is severe, which makes the measurements of the EWs problematic. In particular, blending effects cause an overestimation of the EWs as two blended lines cannot be resolved.

Another bias in the EW measurements may come from the fitting of strong lines.

[1] $T_{\rm eff\odot}$ is the solar temperature.

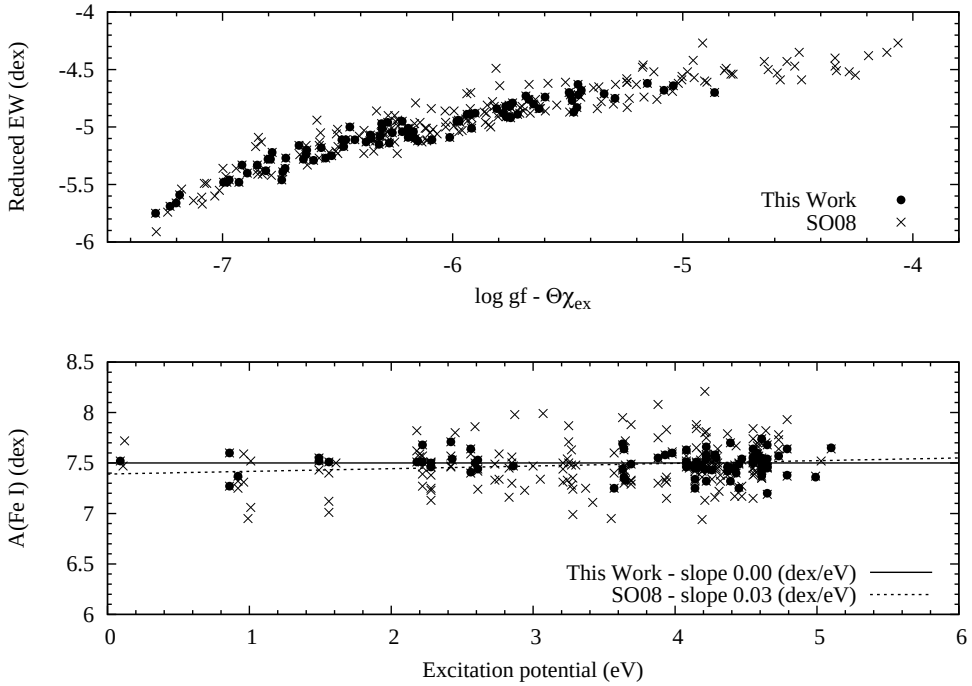

Figure 3.4: Upper panel: Curve of growth for both line lists for the reference star computed for the temperature (Θ=5040/$T_{\rm eff}$) of Tsantaki et al. (2013). Circles represent the reduced EW of the line list of this work and crosses the line list of SO08. Lower panel: The Fe I abundances of the reference star versus the excitation potential. The dashed line shows the positive slope that corresponds to the line list of SO08. The solid line corresponds to the line list of this work and the slope is obviously zero.

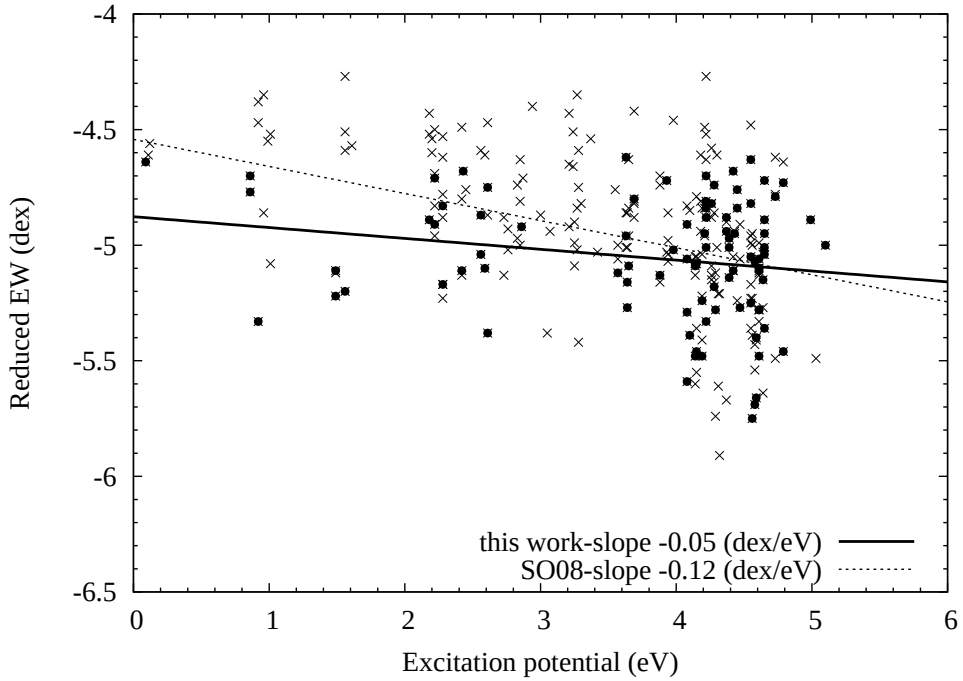

Figure 3.5: Reduced EW versus excitation potential for the line list of Tsantaki et al. (2013) (filled circles) and for SO08 (crosses). The slope of the linear fits is also depicted.

Gaussian fitting is a good approximation for weak lines and it can be reliable up to 150 mÅ based on our experience, whereas a Voigt profile should be used for stronger lines. Saturated lines that deviate significantly from the linear part of the curve of growth should also be avoided in the abundance analysis. The EW predicted by the models of strong lines that are highly saturated, is quite dependent on microturbulence. A wrong estimation of microturbulence, will then produce errors in the abundance of any highly saturated line.

On the other hand, weak lines that are strongly blended can lead to a underestimation of the continuum and consequently of the EW. This effect, however, is less significant. An overestimation in the EW due to blending, as well as the underestimation of very strong lines could be the reason for the systematic raise in temperature that is observed for the cooler stars of SO08. In addition, the reduced EW could also be affected by such biases, leading to correlations with the excitation potential and therefore a degeneracy between $T_{\rm eff}$ and ξ_t. In Fig. 3.5, we show that such correlations with the new line list is reduced considerably when compared with the previous one.

Therefore, our aim is to optimize the iron line list of SO08. With this goal, we use the K-type dwarf HD 21749 with $T_{\rm eff} = 4723$ K (see Table 3.1), as reference in order to check for unblended lines in its high S/N spectrum ($\sim$150 at 6070Å). After visual inspection, we only consider weak, isolated lines that give good estimation for the local continuum. We avoid strong lines (>150 mÅ) in order to apply Gaussian profiles. For the reference

Table 3.3: Sample of the line list used for the spectroscopic analysis with the atomic parameters of Fe I and Fe II as well as the corresponding EWs of the reference star HD 21749.

λ (Å)	χ	$\log gf$	Element	EW(mÅ)
4508.28	2.86	−2.403	Fe II	53.0
4520.22	2.81	−2.563	Fe II	72.4
4523.40	3.65	−1.871	Fe I	101.7
4537.67	3.27	−2.870	Fe I	43.2
4551.65	3.94	−1.928	Fe I	41.9
4556.93	3.25	−2.644	Fe I	57.9
4566.52	3.30	−2.156	Fe I	68.6
4574.22	3.21	−2.353	Fe I	55.1
4576.34	2.84	−2.947	Fe II	29.6
...	...	...	...	...

star we show the curve of growth (see Gray 2005) using both line lists (Fig. 3.4 upper panel). Limiting the EW cut off, we mitigate in large amount the problem of saturated lines and microturbulence. The proof of that mitigation is the fact that the derived temperatures with the new line list agree with other less model-dependent methods (see Sect. 3.6).

Very weak lines (<10 mÅ) were also excluded so that noise is not superposed to these lines. The region of the spectrum below 4500 Å is neglected due to the higher blending. The final line list is compiled with 120 Fe I and 17 Fe II lines, as shown in Table 3.3. The complete list is available in Appendix E and in an online version[2].

As mentioned before, the effective temperature is derived when the correlation coefficient between $\log_\epsilon$(Fe I) and χ is zero. In the lower panel of Fig. 3.4, we demonstrate this correlation for the reference star using the line list of this work and of the work of SO08 using the parameters derived with the line list of this work. The positive slope for the line list of SO08 is translated as an overestimation in temperature of ∼180 K for this star. In addition, the abundances with the new line list show a smaller scatter which corresponds to smaller errors in the final temperature value.

3.4 New stellar parameters for 451 FGK stars in the HARPS GTO sample

To check the effectiveness of the new line list, we re-derive stellar parameters for the 451 stars of the sample. For consistency, we use the same EWs as in SO08 that were measured automatically for all stars with the ARES code. In addition, we use

[2]http://cdsarc.u-strasbg.fr/viz-bin/qcat?J/A+A/555/A150

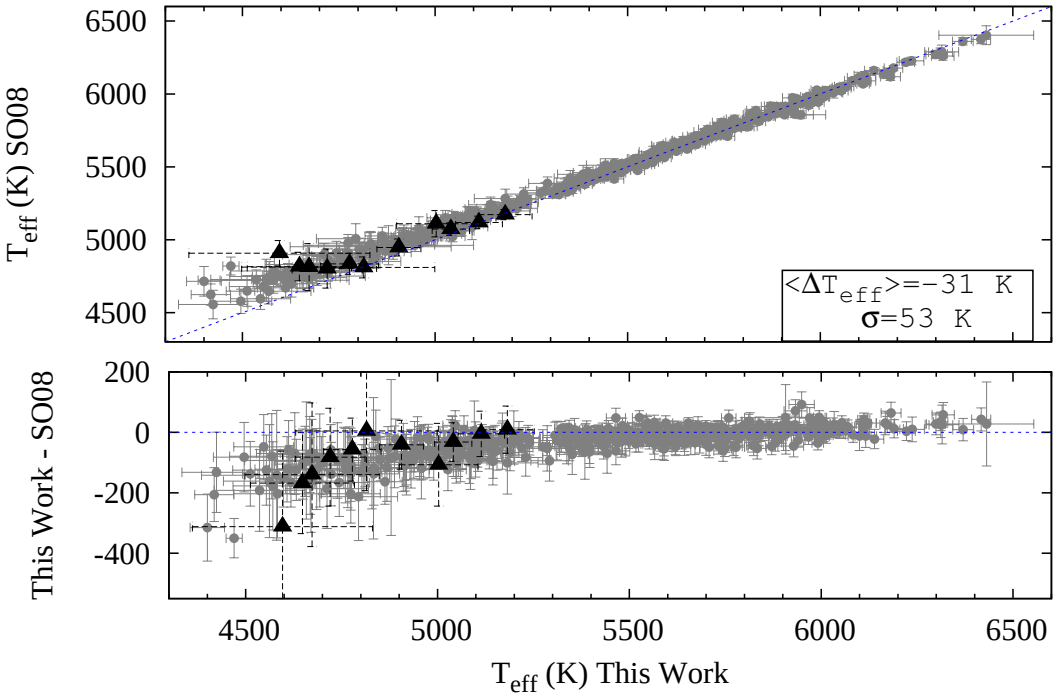

Figure 3.6: Comparison between the temperature derived with the cool line list of this work and the results of SO08. $\Delta T_{\rm eff}$ corresponds to this work minus SO08. Triangles represent stars with planets taken from Table 3.7 (see Sect. 3.7).

the same damping parameters and atomic data for the iron lines. After a preliminary determination of the fundamental parameters, we perform a '3σ clipping' procedure for lines that contribute with abundances higher than 3σ from the average abundance[3]. This procedure was also applied in SO08.

Microturbulence is used as a free parameter and is also derived from this spectroscopic analysis. The correlation of microturbulence with temperature and surface gravity is presented in Appendix A. This calibration can be useful in cases where the value of ξ_t is set fixed. The stellar masses are calculated using the stellar evolutionary models from the Padova group[4]. The errors of the fundamental parameters are internal, attributed to the method. They, thus, represent relative errors and not the absolute accuracy.

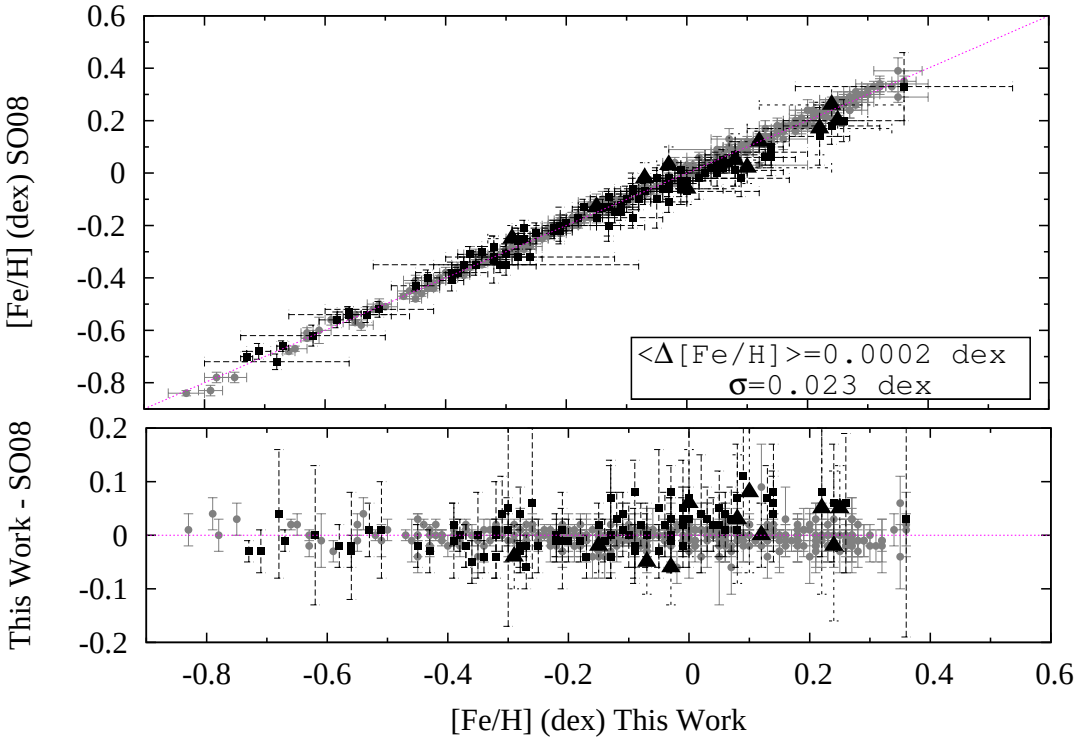

Figure 3.7: Comparison between surface gravity derived with the cool line list of this work and the results of SO08. $\Delta \log g$ corresponds to this work minus SO08. Black squares represent stars with $T_{\rm eff}$<5000 K. Triangles represent stars with planets taken from Table 3.7 (see Sect. 3.7).

Table 3.4: Results of the internal comparison for the whole sample and for stars cooler and hotter than 5000 K.

	$\Delta T_{\rm eff}$ (K)	$\Delta \log g$ (dex)	Δ [Fe/H] (dex)	N
This Work – SO08 whole sample	-31±3	-0.023±0.003	0.0002±0.0011	451
This Work – SO08 $T_{\rm eff}$ <5000 K	-106±6	-0.07±0.01	0.0127±0.0001	90
This Work – SO08 $T_{\rm eff}$ >5000 K	-2±14	0.005±0.010	0.0001±0.0020	361

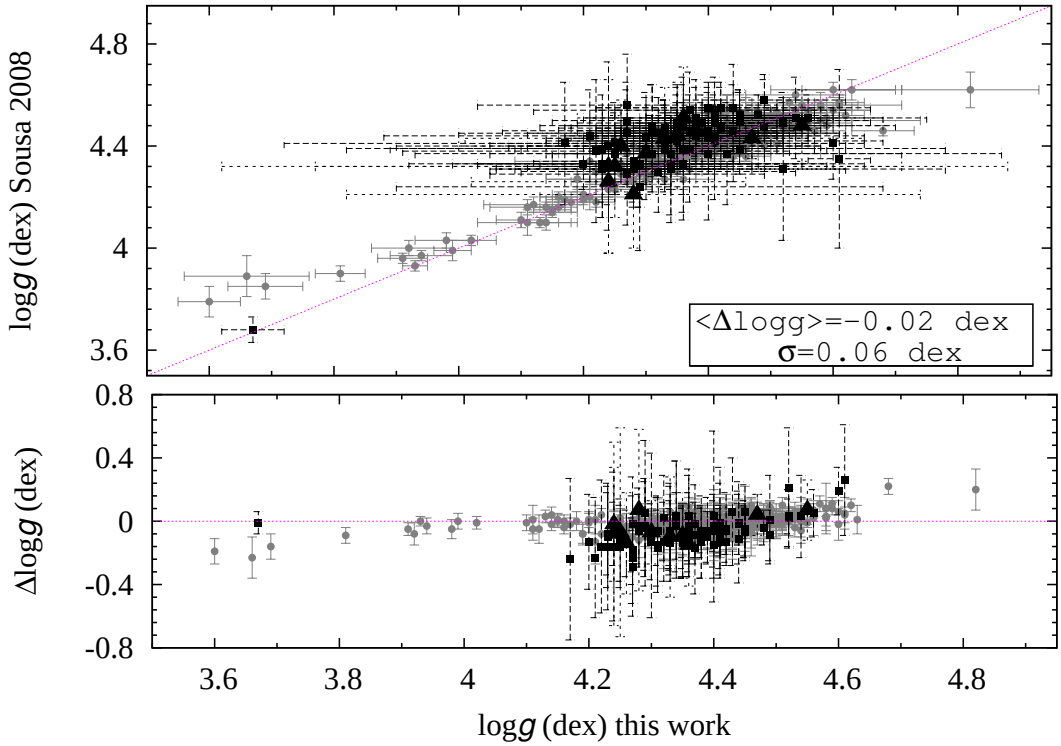

Figure 3.8: Comparison between metallicity derived with the cool line list of this work and the results of SO08. $\Delta[Fe/H]$ corresponds to this work minus SO08. Black squares represent stars with $T_{\rm eff}$<5000 K. Triangles represent stars with planets taken from Table 3.7 (see Sect. 3.7).

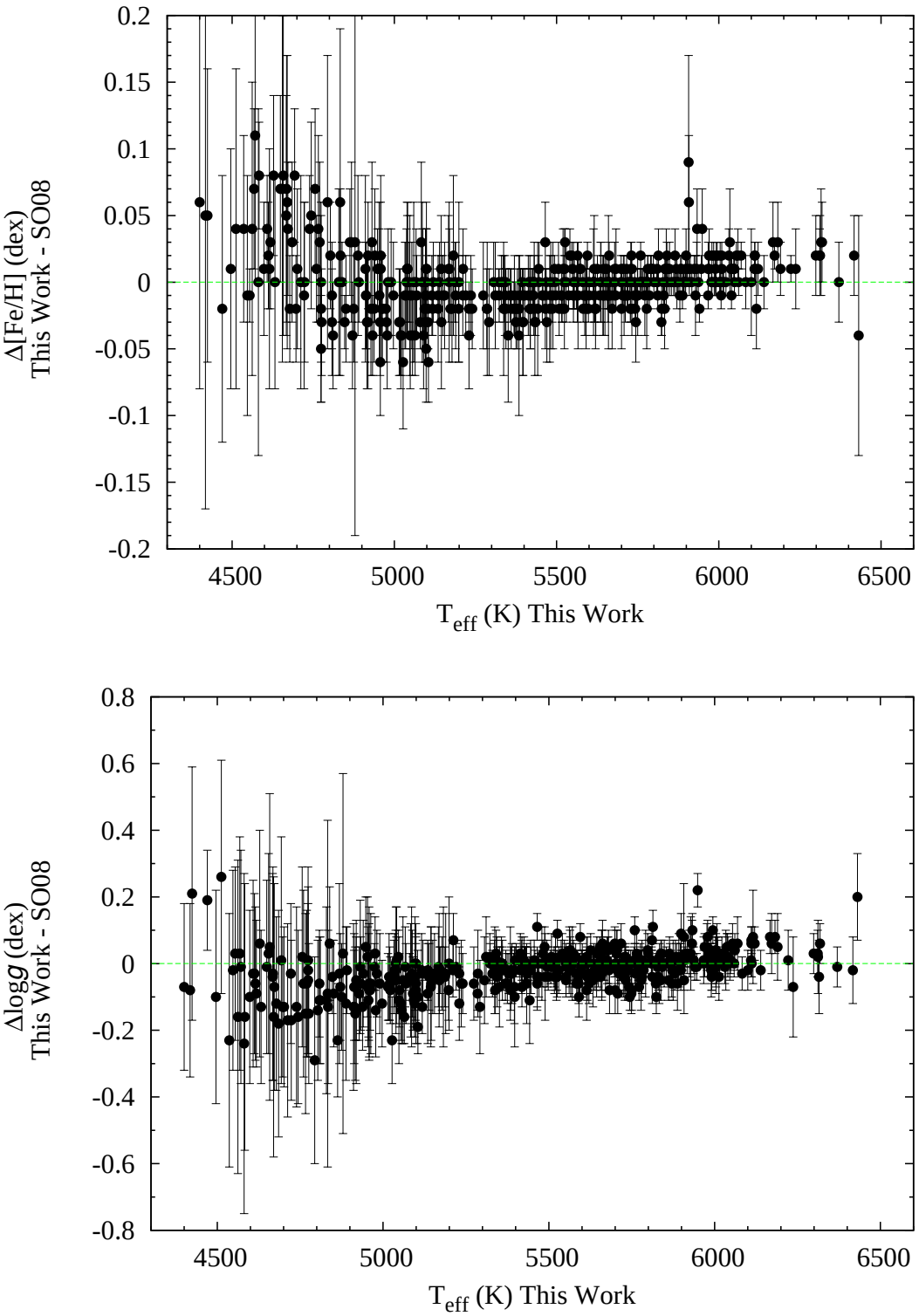

Figure 3.9: The effect of temperature on the other parameters: metallicity (left panel) and surface gravity (right panel). The differences correspond to the values of this work minus the results of SO08.

3.4.1 Internal comparison

We present the comparison results with the work of SO08 for temperature, surface gravity and metallicity, respectively in Figs. 3.6-3.8. Temperatures show very good agreement in the high and intermediate ranges. Table 3.4 shows the mean difference in $T_{\rm eff}$ for the whole sample and for temperatures below 5000 K with their standard errors[5]. The mean difference in $T_{\rm eff}$ is –31±3 (σ=53) K for the whole temperature range. The significant differences appear, as expected, for stars with temperatures below 5000 K with mean difference $\Delta T_{\rm eff}$ = –106±6 (σ=54) K.

One interesting result is that even though we have considerably large differences in the low temperature regime, the values of metallicity remain unaffected with $<\Delta[Fe/H]>$=0.00±0.00 (σ=0.02) dex for the overall sample. The same effect appears for surface gravity with $<\Delta \log g>$=–0.02±0.00 (σ=0.06) dex, even though there is bigger scatter. This result suggests that surface gravity and metallicity are not as sensitive to the selection of the line list as temperature, for this temperature regime and for this method. The same effect appears for the cool stars as seen in Table 3.4.

The impact of the updated effective temperatures on [Fe/H] and on $\log g$ is depicted on Fig. 3.9. The changes in metallicity show almost no correlation, within the errors, with the effective temperature. Only slightly higher metallicities appear for low temperatures, when comparing with SO08, yet within the errors. The surface gravities are also not correlated with temperature, even though there is high dispersion in the low temperature region. This result suggests that using this technique, a potential error in one of the parameters does not propagate to the others, avoiding systematic errors (see also Torres et al. 2012).

Metallicity has a key role in planet formation theories and is correlated with the planet frequency. The stellar sample, as mentioned before, is part of the HARPS GTO planet search program and it contains 102 up-to-date planet hosts. The metallicity distribution of the sample, presented in SO08, shows that the Jovian planets are preferentially found in metal-rich stars, in contrast to Neptune-like planets that do not seem to follow this trend, even though the number of these planets is small. The new metallicities derived with the new line list do not change this trend, making this correlation between stars and planets reliable even before adapting the new temperatures.

3.5 Ionization balance problem in cool stars.

In an LTE abundance analysis for solar type stars the ionization equilibrium should be satisfied. Using the standard spectroscopic method we force the abundance of Fe I and Fe II to agree. Surface gravity is determined from this tuning. However, there are many studies for cluster stars (Yong et al. 2004; Morel & Micela 2004; Schuler et al. 2006) and field stars (Allende Prieto et al. 2004; Ramírez et al. 2007, 2013) showing that

[3]An average number of lines being eliminated from a 3σ clipping is around 5.

[4]Web interface for stellar mass estimation: http://stev.oapd.inaf.it/cgi-bin/param

[5]The standard errors of the mean (σ_M) are calculated with the following formula: $\sigma_M = \frac{\sigma}{\sqrt{N}}$, σ being the standard deviation.

the cooler dwarf stars deviate from the ionization balance, with systematic higher Fe II abundances over Fe I. The authors explain these discrepancies due to possible different scales in the stellar parameters (namely $T_{\rm eff}$ and $\log g$) or due to NLTE effects caused by the simplifications of the model atmospheres. The ionization balance of Fe I and Fe II can be investigated in this work by the behavior of surface gravity. In fact, surface gravity mostly depends on Fe II lines, once the temperature scale is correct.

An essential test for the accuracy of surface gravity derived from spectroscopy is the comparison with surface gravity derived from parallaxes (trigonometric $\log g$), based on the fundamental relation:

$$\log \frac{g}{g_\odot} = \log \frac{M}{M_\odot} + 4 \log \frac{T_{\rm eff}}{T_{\rm eff\odot}} - \log \frac{L}{L_\odot}, \tag{3.1}$$

where L is the stellar luminosity. With the use of basic definitions the above relation becomes:

$$\begin{aligned} \log \frac{g}{g_\odot} = & \log \frac{M}{M_\odot} + 4 \log \frac{T_{\rm eff}}{T_{\rm eff\odot}} + 0.4(V + BC) \\ & -0.4(V_\odot + BC_\odot) + 2 \log \pi + 2 \log d_\odot \end{aligned} \tag{3.2}$$

where V is the visual magnitude, BC the bolometric correction, π the stellar parallax (in arcsec), and $d_\odot$ distance between the Earth and the Sun in parsec. By substituting the typical solar values suggested by Bessell et al. (1998), the formula for the trigonometric gravity becomes:

$$\log \frac{g}{g_\odot} = \log \frac{M}{M_\odot} + 4 \log \frac{T_{\rm eff}}{T_{\rm eff\odot}} + 0.4(V + BC) + 2 \log \pi + 0.108 \tag{3.3}$$

We calculated the trigonometric $\log g$ using the new *Hipparcos* parallaxes (van Leeuwen 2007), V magnitudes, bolometric correction based on Flower (1996) and Torres (2010), the spectroscopic masses and $T_{\rm eff}$. No correction for interstellar reddening is needed since all stars are less than 56 pc in distance.

In Fig. 3.10, we compare the spectroscopic $\log g_{spec}$ with the trigonometric $\log g_{HIP}$. At first glance, the spectroscopic $\log g$ agrees with the trigonometric ($\langle \log g_{HIP} - \log g_{spec} \rangle$ = 0.07 dex). However, a more careful look shows that there is a disagreement especially for the high values of $\log g$ (<4.5 dex) where the spectroscopic gravities are underestimated, which is also observed in the work of SO08.

An interesting fact is that the differences between the trigonometric and spectroscopic $\log g$ are greater for the cooler stars (Fig. 3.11). There is a clear trend between the differences in $\log g$ and $T_{\rm eff}$, where the underestimation of surface gravity in low temperatures becomes higher ($\langle \log g_{HIP} - \log g_{spec} \rangle$=0.22 dex for stars with $T_{\rm eff} < 5000$ K). This is translated into systematically higher Fe II abundances over Fe I for low $T_{\rm eff}$.

Such differences between Fe I and Fe II abundances are difficult to explain with model uncertainties and departures from LTE in the calculations of line formation as they are expected to increase for the warmer stars of our sample where most iron is ionized (Lind et al. 2012). In addition, other model uncertainties related to granulation and activity of

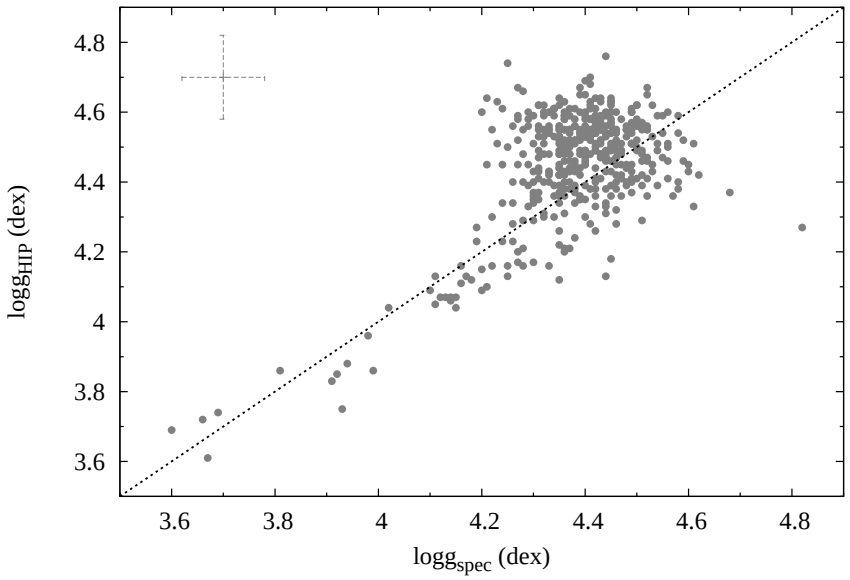

Figure 3.10: Comparison of the surface gravities derived from spectroscopy of this work ($\log g_{spec}$) and from *Hipparcos* parallaxes ($\log g_{HIP}$). A mean error for both axes is given in the upper left part.

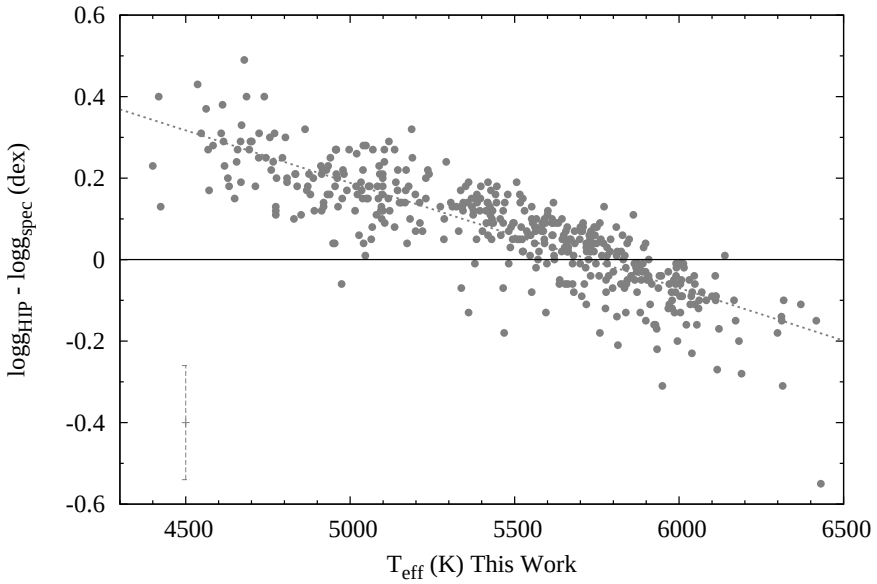

Figure 3.11: Trigonometric $\log g_{HIP}$ minus $logg_{spec}$ as a function of temperature. The dashed line represents a linear fit ($-2.578 \cdot 10^{-4} T_{\rm eff} + 1.477$). The mean error is shown at the bottom left.

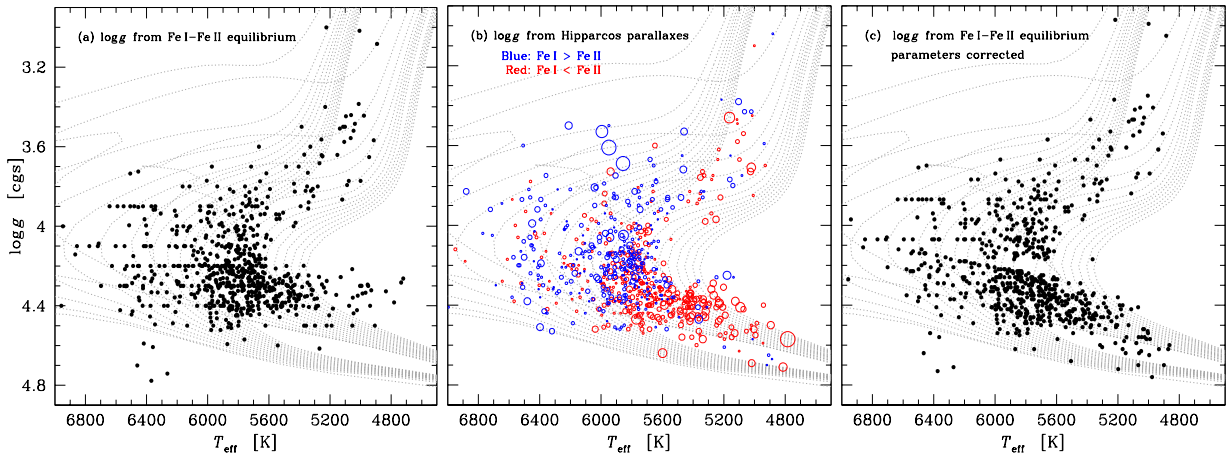

Figure 3.12: HR diagram for the Bensby et al. (2014) sample when a) $\log g$ is based on Fe I–Fe II ionization equilibrium, and b) when $\log g$ is based on Hipparcos parallaxes. In b) the sizes of the circles are scaled with the difference between Fe I and Fe II abundances. Red circles mark those stars where the Fe I abundances are lower than the Fe II abundances, and vice versa for the blue circles. The Yonsei-Yale (Y2) isochrones are shown from 1 to 15 Gyr in steps of 1 Gyr.

K-stars have been proposed to explain these differences even though these effects should be more evident for young stars (Morel & Micela 2004; Schuler et al. 2010).

Other possible explanations for these differences have to do with the iron ionization method itself. We use Fe II lines that strongly depend on surface gravity. For solar-type stars, however, these lines are not weak, leading to poorly constrains of $\log g$. On the other hand, Fe I lines are numerous but insensitive to $\log g$ changes.

We have to note though, that temperatures and metallicities derived using the ionization and excitation equilibrium of iron lines are shown to be mostly independent of the ionization balance (Torres et al. 2012). Hence, the temperatures and metallicities derived with our spectroscopic method are precise, even if the derived spectroscopic surface gravities differ from the trigonometric values (see also Santos et al. 2013).

Recently, Bensby et al. (2014) noted the same ionization problem in their samples. The authors derived surface gravity values using the EW method and compared with the trigonometric ones for FKG stars in their sample. As indicated by their results (see Fig. 3.12), ionization balance has its limitations, and mainly on the lower main sequence for stars with $\log g < 4.2$ dex and $T_{\rm eff} < 5600$ K. After applying a linear correction to the ionization balance parameters (Fig. 3.12c), there is a better match with the isochrone lines.

3.6 Comparison with other methods

To evaluate the consistency of our results, namely for $T_{\rm eff}$, we compare them with other techniques. Here, we present a comparison with two different methods that are

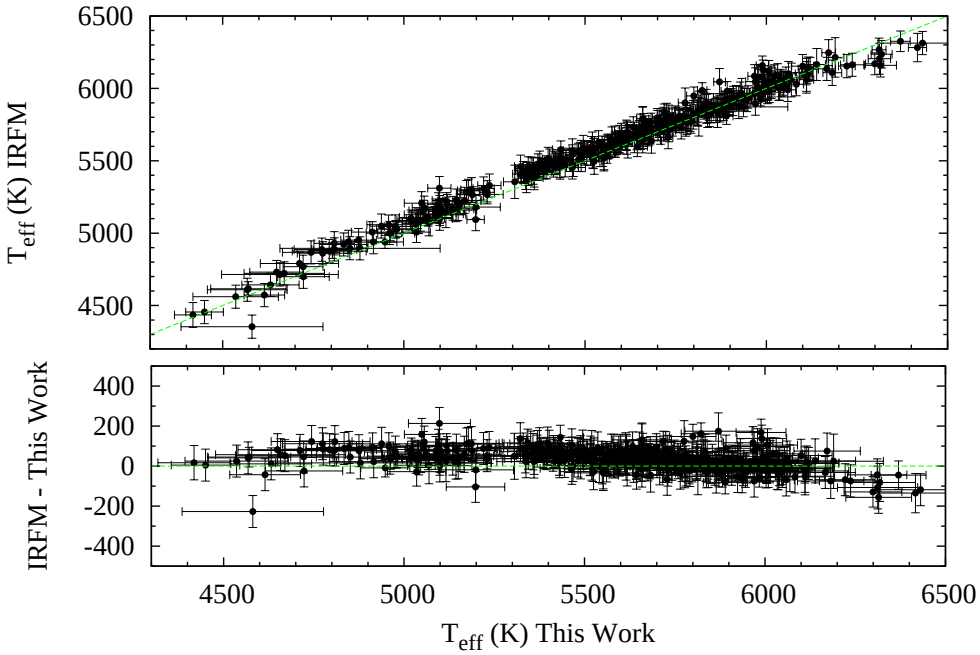

Figure 3.13: Comparison between the temperatures derived from this work and the IRFM for stars in common.

considered to be less model dependent, the infrared flux method (IRFM) and interferometry, respectively.

3.6.1 The infrared flux method - IRFM

The IRFM method (Blackwell & Shallis 1977) is a semi-direct method for determining stellar parameters. The principle of this method relies on the fact that the bolometric flux depends on the angular diameter and the effective temperature, as described by the Stefan-Boltzmann law, whereas the monochromatic flux in the infrared (IR) depends on the angular diameter but weakly on the effective temperature, this way the dependence on the angular diameter disappears, described by Equation 1.3. The IRFM has the advantage that the dependence on the models is limited while the spectroscopic effective temperatures have considerable model dependence.

We compare our results with the work of Casagrande et al. (2010, 2011) that implement the IRFM method for a large sample of stars. The authors estimate the bolometric flux from multi-band photometric measurements in the optical ($BV(RC)_C$) band and in the near-IR (2MASS JHK_S) band. For the missing spectral regions, the flux is calculated by synthetic spectra computed from model atmospheres. The absolute calibration of Vega is based on its synthetic spectrum with an uncertainty of the zero point of $\sim$15 K (Casagrande et al. 2010).

Table 3.5: Comparison between the effective temperatures derived with different methods. σ represents the standard deviation and N the number of stars for the comparison.

Method	$\Delta T_{\rm eff}(K)$	$\sigma(K)$	N
IRFM – this work	$+33 \pm 3$	54	347
IRFM – SO08	$+14 \pm 3$	61	347
IRFM – this work ($T_{\rm eff}$ <5000 K)	$+42 \pm 12$	65	29
IRFM – SO08 ($T_{\rm eff}$ <5000 K)	-86 ± 16	86	29
Interferometry – this work	-4 ± 33	98	9
Interferometry – SO08	-56 ± 35	105	9
Interferometry – IRFM	-98 ± 83	204	6

Figure 3.13 depicts the comparison between the spectroscopic temperatures and the IRFM for the stars in common. Temperatures of 341 stars are taken from Casagrande et al. (2011) using stars with direct application of the IRFM (*irfm* sample) and stars with $T_{\rm eff}$ derived from color calibrations (*clbr* sample). For the *clbr* sample, the effective temperatures and bolometric fluxes were computed using the color calibrations in (b – y), (B_T – V_T), (V_T – J), (V_T – H) and (V_T – K_S) from Casagrande et al. (2010). Moreover, temperatures for six stars were taken from Casagrande et al. (2010). The comparison between the results of this work and the IRFM shows good agreement for all temperature ranges. In particular, for the cooler temperature region, the differences in $T_{\rm eff}$ between this work and the IRFM are much smaller and more homogeneously distributed than between SO08 and the IRFM.

The mean differences in temperature for the comparison samples are shown in Table 3.5. It is clear that the differences in temperature for this work with the IRFM are constant throughout the temperature range, with a small offset of 33 K for the whole sample. For the cooler stars these differences are $\Delta T_{\rm eff}$ = 42 ± 12 K that are much smaller than SO08 with $\Delta T_{\rm eff}$ = -86 ± 16 K. Figure 3.14 shows the comparison of stars with $T_{\rm eff}$<5000 K. It is evident that the trend in $\Delta T_{\rm eff}$ of SO08 mostly disappears with the new temperatures.

3.6.2 Interferometry

Precise measurements of stellar angular diameters are acquired through long baseline interferometry both in the optical and in the infrared (e.g., SUSI - Davis & Tango 1986; Davis et al. 2011, Mark III - Mozurkewich et al. 1991, NPOI - Nordgren et al. 1999, IOTA - Dyck et al. 1996, PTI - Colavita et al. 1999, VLTI - Glindemann et al. 2000, CHARA - McAlister et al. 2005). The standard practice to determine the angular diameter is to fit the observed visibilities as a function of baseline to a uniform disc model. The angular size is connected to the more realistic limb darkened angular size (θ_{LD}) using correction factors from model atmospheres (Claret 2000). The effective temperature is

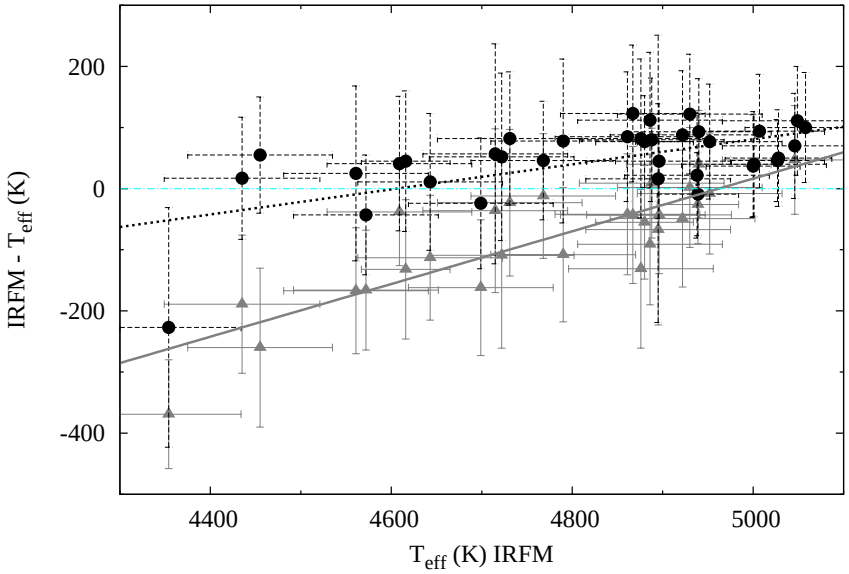

Figure 3.14: Comparison between the difference in temperatures derived from IRFM - This Work (circles) and IRFM - SO08 (triangles). The dashed and the solid line depict the linear fits of the data with slopes: +0.20±0.04 and +0.43±0.05, respectively.

then derived with the standard relation:

$$T_{\rm eff} = \left(\frac{L}{4\pi\sigma R^2}\right)^{1/4} = \left(\frac{4f_{bol}}{\sigma\theta_{LD}^2}\right)^{1/4}, \tag{3.4}$$

where f_{Bol} is usually calculated from the Spectral Energy Distribution.

We compare our results with the temperatures derived from interferometry. Unfortunately, the number of stars with available angular diameters for this sample is only down to a few since these measurements are challenging for dwarfs due to their small photospheric discs that are difficult to resolve. We have 9 stars in common for the comparison with spectroscopy and 6 with the IRFM. We use only direct angular diameters and bolometric fluxes available in the literature from Table 3.6. Our results show better agreement for these stars to interferometry than when comparing with the values of SO08 and the IRFM (see Table 3.5). We have to note though, that the comparison sample is very small and the values of $T_{\rm eff}$ were derived from the *clbr* sample that is not the best representative for the IRFM precision.

The differences in temperatures for the different methods are plotted in Fig. 3.15. For 3 stars (HD 10700, HD 26965, HD 146233) we include angular diameter measurements from different authors that give different $T_{\rm eff}$ and are represented with different symbols. In the same figure, we see that from the stars with multiple measurements, the ones with the smallest uncertainty ($\frac{\Delta\theta}{\theta}\%$) agree better with the temperatures derived with

Table 3.6: Interferometric data and derived temperatures for stars in common with our sample. Stars with alternative angular diameters are also presented here.

Star HD	θ_{LD} (mas)	$\Delta\theta/\theta$ (%)	$T_{\rm eff}^{Int}$ (K)	$T_{\rm eff}^{SO08}$ (K)	$T_{\rm eff}^{thiswork}$ (K)	$T_{\rm eff}^{IRFM}$ (K)	References
10700	2.022 ± 0.011	0.54	5383 ± 47	5310 ± 17	5322 ± 17	5459 ± 80	1, a
...	1.971 ± 0.050	2.54	5449 ± 83	...	...	...	2, a
11964	0.611 ± 0.081	13.25	5413 ± 359	5332 ± 22	5285 ± 21	-	3, b
19994	0.788 ± 0.026	3.30	6109 ± 111	6289 ± 46	6315 ± 44	6159 ± 80	3, b
22049	2.148 ± 0.029	1.35	5107 ± 21	5153 ± 42	5049 ± 48	5207 ± 80	4, c
23249	2.394 ± 0.029	1.21	4986 ± 57	5150 ± 51	5027 ± 48	-	5, a
26965	1.504 ± 0.006	0.40	5143 ± 14	5153 ± 38	5098 ± 32	5311 ± 80	6, d
...	1.650 ± 0.060	3.63	4910 ± 90	...	...	...	4, d
128621	6.001 ± 0.021	0.35	5182 ± 24	5234 ± 63	5168 ± 75	-	7, e
146233	0.676 ± 0.006	0.89	5836 ± 46	5818 ± 13	5810 ± 12	5826 ± 80	8, f
...	0.780 ± 0.017	2.18	5433 ± 69	...	...	...	9, f
209100	1.890 ± 0.020	1.06	4527 ± 29	4754 ± 89	4649 ± 73	4731 ± 80	4, g

References for θ_{LD}: (1) Teixeira et al. (2009); (2) Pijpers et al. (2003); (3) van Belle & von Braun (2009); (4) Kervella & Fouqué (2008); (5) Thévenin et al. (2005); (6) Boyajian et al. (2012b); (7) Kervella et al. (2003); (8) Bazot et al. (2011); (9) Boyajian et al. (2012a). References for f_{bol}: (a) Bruntt et al. (2010); (b) van Belle & von Braun (2009); (c) Cayrel et al. (2011); (d) Boyajian et al. (2012b); (e) Ramírez & Meléndez (2004); (f) Boyajian et al. (2012a); (g) Ramírez & Meléndez (2005).

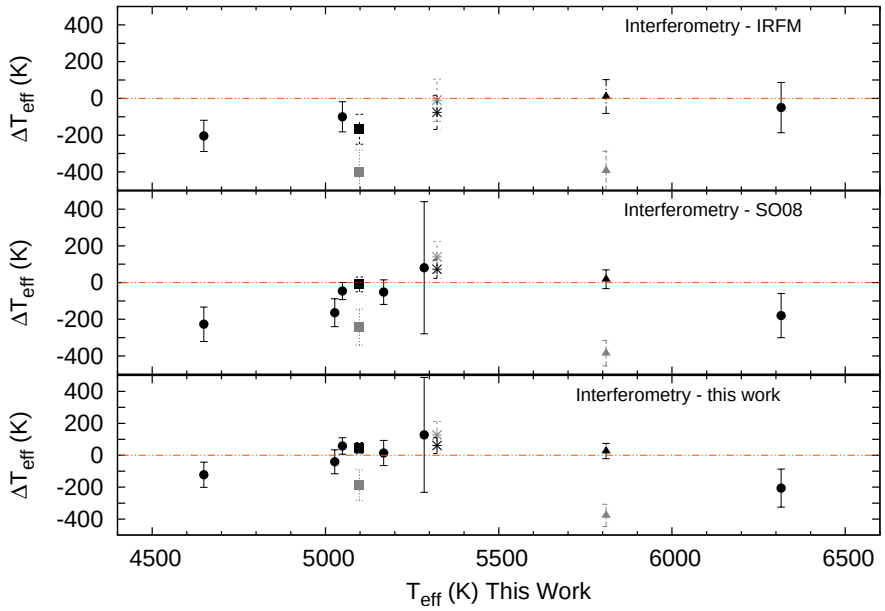

Figure 3.15: Comparison between the spectroscopic, the IRFM and the direct temperature measurements for stars in common with the literature. The x-axis corresponds to temperatures derived from this work. Square symbols are for the different temperatures for HD 26965, stars for HD 10700 and triangles for HD 146233. Stars with grey color represent $T_{\rm eff}$ with high angular diameter uncertainty.

the spectroscopic and photometric methods. A precision better than 2% in the angular diameters corresponds to an accuracy of 1% in the effective temperatures, which is roughly 60 K at solar temperature, assuming no error in the bolometric flux. It is useful thus, to take the uncertainty of the angular diameter into consideration for a reliable determination of temperature.

3.7 New atmospheric parameters for cool planet hosts

The planet-host stars with effective temperature below 5200 K derived using the line list of SO08, imply that they have overestimated temperatures. This has implications for both their mass and radius determination. The lower temperatures imply lower stellar masses as well as lower stellar radii. This means that the derived planetary masses and radii (for transit planet cases) are also lower. As a consequence of the mass reduction, the semi-major axis of the orbits will also be smaller. The expected effects are however small, and no major revisions are expected to occur.

With this new line list, we re-derive the stellar parameters for 10 "cool" planet hosts already published in the literature and are not included in the 451 stellar sample of this work. We only consider GK dwarfs with an effective temperature lower than 5200 K whose planets were detected with the radial velocity technique from the CORALIE and HARPS GTO planet search samples. These planet hosts have been previously analyzed with high S/N spectra following the same procedure as this work but with different line lists.

In Table 3.7, the fundamental parameters based on the new line list are presented. The sixth column gives the reference of the previously published parameters. To explain the effect on mass of these new parameters more quantitative, we calculate the stellar masses from the Padova interface for both with the original and new parameters. We avoid using the published stellar masses in order to compare uniformly. We find the maximum difference in mass to be 1.5% in absolute units which is negligible compared to the standard mass error.

3.8 Ionization balance vs. $T_{\rm eff}$ for other elements

The precise and accurate stellar parameters are, as well, very important for further analyzing stellar chemical abundances. The traditional spectroscopic abundance analysis methods require these parameters as input to compute the atmosphere models, hence the accuracy of the final elemental abundances depends on the accuracy of these input parameters. Different atoms and ions are not equally sensitive to all the stellar parameters. For example, ionized species are more sensitive to gravity variations than neutral species (e.g., Gilli et al. 2006; Neves et al. 2009; Adibekyan et al. 2012c).

Recently, Neves et al. (2009) and Adibekyan et al. (2012c) analyzing chemical abundances of the refractory elements in the HARPS sample stars, observed some unexpected trends with effective temperature. Particularly, they detected systematic trends of [X/H] or [X/Fe] with $T_{\rm eff}$ for some elements at low temperatures and found that [Cr I/Cr II]

Table 3.7: Updated stellar parameters for previously analyzed planet hosts.

Name	$T_{\rm eff}$ (K)	$\log g$ (cm s^{-2})	[Fe/H] (dex)	ξ_t (km s^{-1})	Reference
BD-082823	4648 ± 135	4.33 ± 0.32	0.00 ± 0.08	0.27 ± 0.81	1
HD 3651	5182 ± 79	4.30 ± 0.16	0.12 ± 0.05	0.66 ± 0.15	2
HD 13445	5114 ± 61	4.55 ± 0.13	-0.29 ± 0.04	0.66 ± 0.15	2
HD 20868	4720 ± 91	4.24 ± 0.22	0.08 ± 0.06	0.47 ± 0.31	1
HD 99492	4815 ± 184	4.28 ± 0.46	0.24 ± 0.12	0.50 ± 0.56	4
HD 125595	4596 ± 235	4.25 ± 0.63	0.10 ± 0.14	0.14 ± 1.41	3
HD 128311	4778 ± 75	4.35 ± 0.17	-0.03 ± 0.02	0.82 ± 0.16	2
HD 192263	4906 ± 57	4.36 ± 0.17	-0.07 ± 0.02	0.78 ± 0.12	2
HD 215497	5003 ± 103	4.26 ± 0.26	0.25 ± 0.05	0.61 ± 0.22	1
HIP 5158	4673 ± 175	4.24 ± 0.47	0.22 ± 0.12	0.34 ± 1.09	1

(1) Sousa et al. (2008); (2) Santos et al. (2004); (3) Ségransan et al. (2011); (4) Santos et al. (2005).

and [Ti I/Ti II] abundance ratios gradually increase with decreasing effective temperature when $T_{\rm eff} < 5000$ K. Similar trends for different elements with $T_{\rm eff}$ have been already noted in the literature (see e.g., Valenti & Fischer 2005; Preston et al. 2006; Gilli et al. 2006; Lai et al. 2008; Suda et al. 2011). Different explanations of the mentioned trends are discussed in the literature. The unexpected trends in the low temperature regime may be due to the stronger line blending and may also be connected to either deviations from excitation or ionization equilibrium, or to problems associated with the differential analysis (Neves et al. 2009). A possible explanation for the observed trends with $T_{\rm eff}$ could also be an incorrect T-τ relationship in the adopted model atmospheres (Lai et al. 2008) or NLTE effects (Bodaghee et al. 2003). Summarizing, it can be assumed that the observed trends are probably not an effect of stellar evolution, and uncertainties in atmospheric models are the dominant effect in measurements (see also the discussion in Adibekyan et al. 2012c).

In Fig. 3.16, we plot the [Cr I/Cr II] and [Ti I/Ti II] abundance ratios derived using the stellar parameters of SO08 and this work as a function of the $T_{\rm eff}$ for stars cooler than 5000 K. This plot is useful to ensure that the ionization equilibrium enforced on the Fe II lines is acceptable to other elements. As can be seen the slopes of the abundance ratios with new parameters are very gentle. The new slope of [Cr I/Cr II] per 1000 K is -0.16 ± 0.08, whereas the slope with the parameters of SO08 is -0.49 ± 0.08. The new slope of [Ti I/Ti II] is also improved a lot and is -0.18 ± 0.06 dex per 1000 K. For comparison the slope of SO08 is -0.39 ± 0.08 dex. Although the trend with $T_{\rm eff}$ is weak, there is a shift of about 0.2 dex for the [Ti I/Ti II] ratio. This shift is difficult to connect to the still possible uncertainties in the stellar parameters and its exact nature still remains to be clarified. Probably, one (or more) of the above mentioned effects can be responsible for that. Unfortunately, in the literature there is no available NLTE calculations for the Ti I and Ti II lines used in our study, and it is difficult to estimate

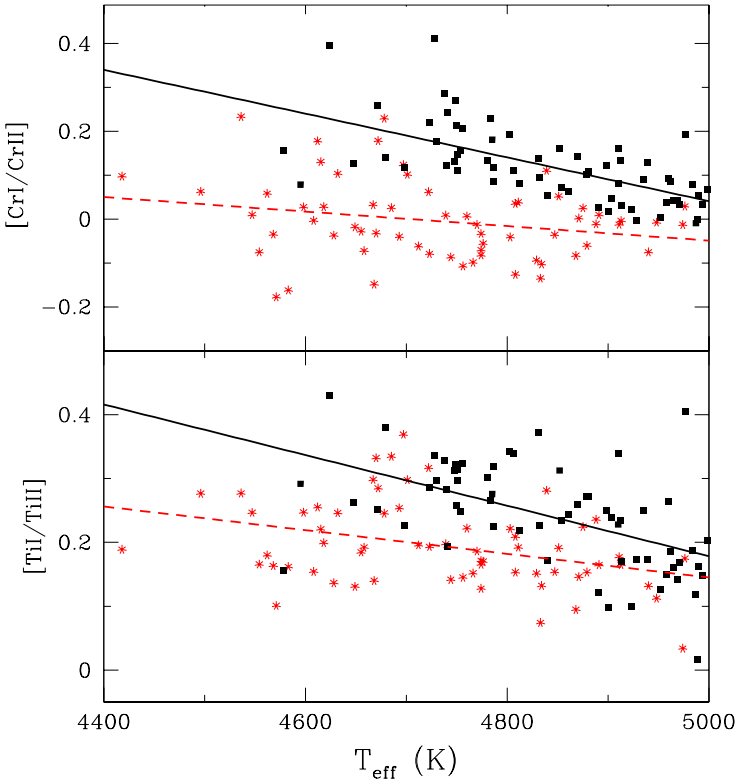

Figure 3.16: [Cr I/Cr II] and [Ti I/Ti II] as a function of effective temperature. The black squares and red asterisks correspond to the abundance ratios derived using the stellar parameters of SO08 and this work, respectively. The solid and dashed lines depict the linear fits of the data.

the NLTE effect for the [Ti I/Ti II] ratio.

Summarizing, this independent test shows that the new stellar parameters derived from the iron lines more carefully chosen for cooler stars make the observed [Cr I/Cr II] and [Ti I/Ti II] trends with $T_{\rm eff}$ much weaker.

3.9 Impact of this work

With the completion of this work (hereafter TS13) we are able to derive precise and accurate parameters for the cooler stars. Our line list has been used for determining stellar parameters for planet-host stars. After almost a decade of gathering high resolution spectra for planet hosts, our team has compiled a catalog with atmospheric parameters derived from a uniform analysis (Santos et al. 2013). This new catalog of stellar parameters for stars with planets (SWEET-Cat), uses the line list of this work for the cooler planet hosts (Fig. 3.17).

Another important application of this work is the determination of stellar parameters

for evolved stars, and especially the cool giant stars in recent work of Mortier et al. (2013a). The authors after using different line list sets, concluded that the optimal line list was the one of this work for evolved stars (Fig. 3.18). In their work, they investigated the correlation between planet frequency and stellar metallicity. The authors found no metallicity enhancement for red giants with planets with respect to red giants without planets.

Finally, Alves et al. (2015; accepted) published a catalog of accurate stellar atmospheric parameters for a sample of 257 K & G field evolved stars that are being surveyed for planets, using precise radial velocity measurements, as part of the CORALIE program to search for planets around giants. The authors compared different line lists and concluded that the line list of TS13 was the optimal for their analysis. The parameters of that work were later used for chemical abundance determinations in the subsequent work of Adibekyan et al. (2015; submitted).

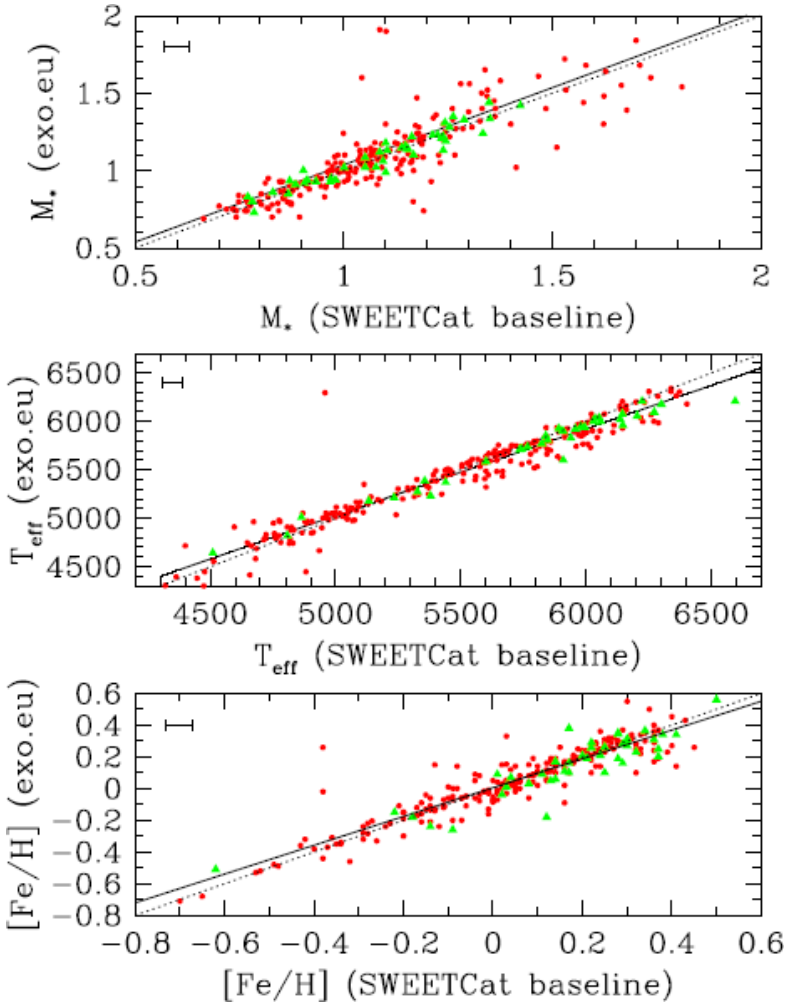

Figure 3.17: Comparison between our baseline stellar parameters with those listed in the Extrasolar Planets Encyclopedia RV planet hosts. Green triangles denote the 48 stars whose parameters are presented in Santos et al. (2013). The dotted line represents a 1:1 relation, and the full line a linear fit to the data. Typical error bars are shown on the upper left part of each panel. Taken from Santos et al. (2013).

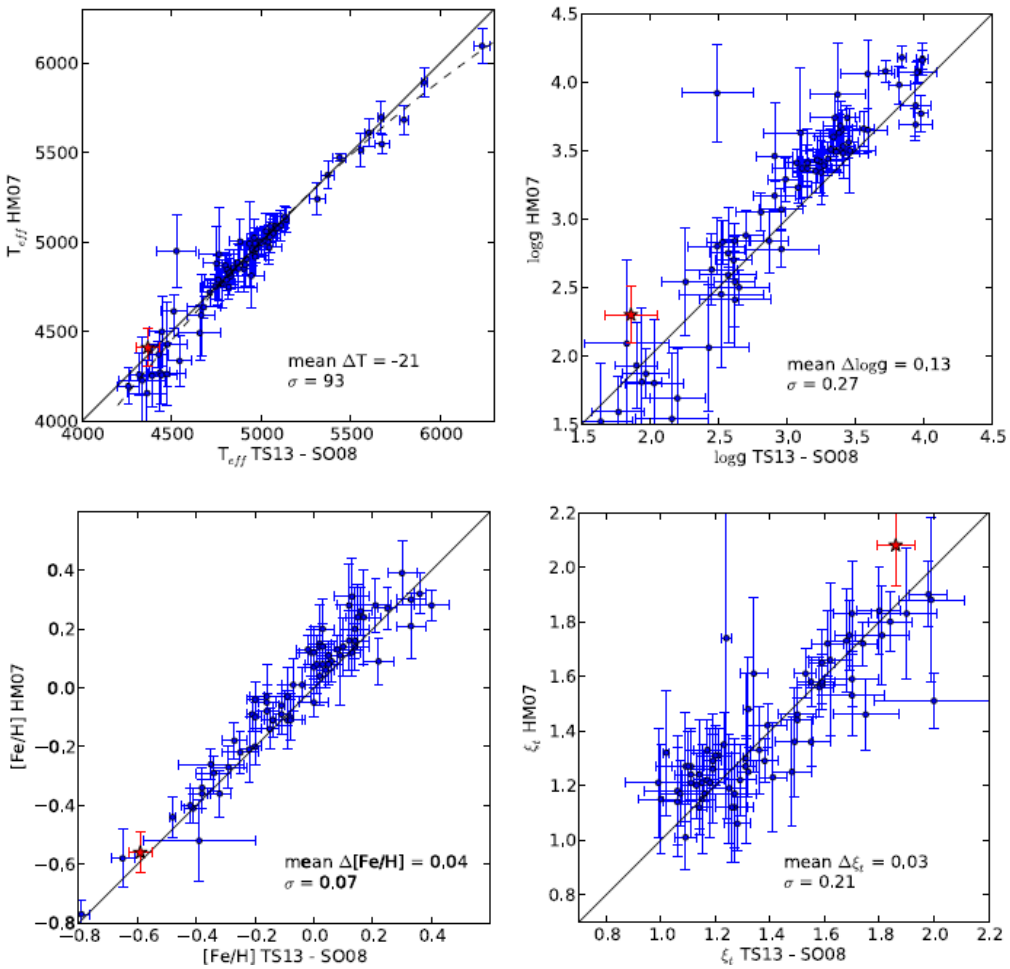

Figure 3.18: Comparisons of the spectroscopic results from the TS13–SO08 line list versus the Hekker & Meléndez (2007) line list for effective temperature, surface gravity, metallicity, and microturbulence. The measurements for the reference star Arcturus are over-plotted with a star symbol. The dashed line in the top-left panel represents a second degree polynomial fit. Taken from Mortier et al. (2013a).

CHAPTER 4

Spectroscopic stellar parameters - Spectral synthesis

"Science. It works b*****!"

R. Dawkins

The principle of the spectral synthesis technique relies on the construction of a model spectrum that represents as precise as possible the atmosphere of a star. The characteristics of the spectrograph should also be taken into consideration to directly compare with observations. The output of such computations is the flux in as a function of wavelength, which can be matched with observations and provide meaningful astrophysical information. The computation of a spectral region requires atomic and molecular data of the lines to be constructed.

There are several programs in the literature that make use of synthetic spectra (e.g., SME - Valenti & Piskunov 1996, VWA - Bruntt et al. 2002, MATISSE - Recio-Blanco et al. 2006, SPC - Buchhave et al. 2012, iSpec - Blanco-Cuaresma et al. 2014). Even though the basic principle is the same for all codes, there are many significant differences in the methodologies. For example, Recio-Blanco et al. (2006) use a grid of pre-computed synthetic spectra to determine a basis allowing the derivation of a particular stellar parameter by projection of an object spectrum. Other differences in the methodologies arise from the choice of model atmospheres, line lists and minimization algorithms.

In this work, we use the package SME (Spectroscopy Made Easy - Valenti & Piskunov

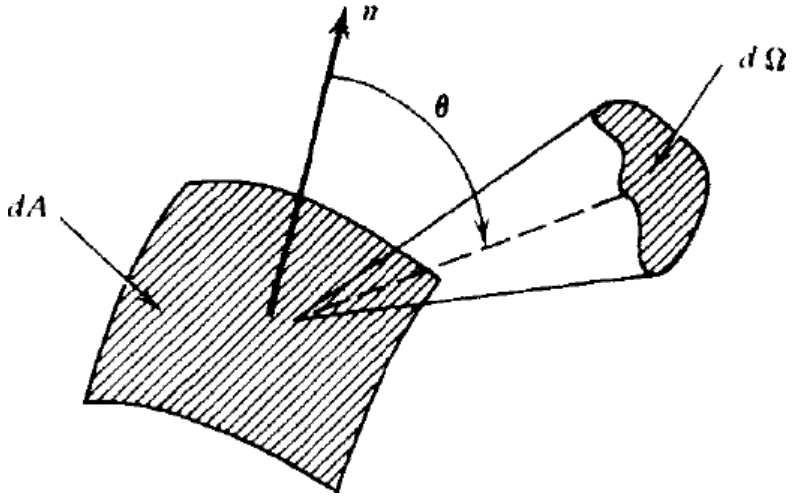

Figure 4.1: Radiation from a surface. Taken from Rybicki & Lightman (1985).

1996) to determine the fundamental stellar parameters. In the following sections we will describe the basic principles of this technique and the code itself.

4.1 Calculation of the synthetic spectrum

SME calculates the radiative transfer equation and generates synthetic spectra using the SYNTH code (Piskunov 1992). The construction of a synthetic spectrum requires some basic assumptions. Only absorption lines are considered and line formation is treated in LTE. A plane parallel and static atmosphere is assumed when the geometrical thickness of the photosphere is very small compared to the stellar radius.

Even though the spectrum is synthesized under the above restrictions, it still gives a detailed enough description of the processes inside the stellar atmosphere. In the following sections, we present a few definitions of the properties that take place in the generation of a synthetic spectrum.

4.1.1 The radiative transfer equation

Any synthesis code has to calculate how the energy is transferred from the bottom of the photosphere to the top, i.e. to solve the radiative transfer equation. In this way, we obtain the flux at the surface of the photosphere and then we can match it with the observations.

Energy is transported through the stellar atmosphere by radiation. Let us consider radiation traveling through thin material from a surface, dA, as shown in Fig. 4.1. The specific density, I_ν, is defined as the amount of energy, dE_ν, passing through the surface dA at the direction of θ per unit of solid angle, $d\omega$, per unit of time, dt, and per unit of

frequency, $d\nu$:

$$I_\nu = \frac{dE_\nu}{\cos\theta dA d\omega dt d\nu} \tag{4.1}$$

The material could either absorb and/or emit photons, changing in either way the specific intensity. In case of absorption, the decrease in I_ν over a path of length, ds, is expressed as:

$$dI_\nu = -K_\nu \rho I_\nu ds, \tag{4.2}$$

where K_ν is the total (mass) absorption coefficient in units of area per mass and ρ is the mass density per unit volume. On the other hand, emission is defined as:

$$dI_\nu = j_\nu \rho ds, \tag{4.3}$$

where j_ν is the emission coefficient in units of $\mathrm{erg\,s^{-1}\,rad^{-2}\,Hz^{-1}\,g^{-1}}$.

To quantify the light removed from a beam by scattering or absorption during its path through a medium, it is usual to define a quantity called the optical depth, τ_ν.

$$\tau_\nu = \int_0^S K_\nu \rho ds \tag{4.4}$$

The optical depth varies not only geometrically, but also as a function of wavelength and it is a measure of transparency of the medium. If the optical depth is large ($\tau_\nu \gg 1$), then a transition is classed as optically thick. Conversely, in the limit of only a few photons being absorbed, the optical depth is small ($\tau_\nu \ll 1$). In this case the line is optically thin.

In total, the change in the specific intensity is expressed by the sum of the absorption and emission processes as:

$$dI_\nu = -K_\nu \rho I_\nu ds + j_\nu \rho ds = -d\tau_\nu I_\nu + d\tau_\nu (j_\nu / K_\nu) \tag{4.5}$$

$$\frac{dI_\nu}{d\tau_\nu} = -I_\nu + S_\nu, \tag{4.6}$$

where the quantity S_ν ($= j_\nu \ / \ K_\nu$) is called the source function. The latter equation describes the **radiative transfer** (RT) in the photosphere.

Now we will try to solve this equation by making some simplifications. One solution could be of the the form of:

$$I_\nu(\tau_\nu) = G e^{b\tau_\nu}, \tag{4.7}$$

where G is a function to be determined. Equation 4.6 is then transformed:

$$\begin{aligned} bGe^{b\tau_\nu} + e^{b\tau_\nu}\frac{dG}{d\tau_\nu} &= -I_\nu + S_\nu \\ bI_\nu + e^{b\tau_\nu}\frac{dG}{d\tau_\nu} &= -I_\nu + S_\nu \end{aligned} \tag{4.8}$$

The terms of right side are equal to the terms of the left side of the equations:

$$b = -1 \tag{4.9a}$$

$$e^{-\tau_\nu} \frac{dG}{d\tau_\nu} = S_\nu \Rightarrow \tag{4.9b}$$

$$G(\tau_2) = G(\tau_1) + \int_{\tau_1}^{\tau_2} S_\nu e^{t_\nu} dt_\nu \Rightarrow \tag{4.9c}$$

$$I_\nu(\tau_2)e^{\tau_2} = I_\nu(\tau_1)e^{\tau_1} + \int_{\tau_1}^{\tau_2} S_\nu(t_\nu)e^{t_\nu} dt_\nu \Rightarrow \tag{4.9d}$$

$$I_\nu(\tau_2) = I(\tau_1)e^{(\tau_1-\tau_2)} + \int_{\tau_1}^{\tau_2} S_\nu(t_\nu)e^{-(\tau_2-t_\nu)} dt_\nu \tag{4.9e}$$

The difficulties in solving the above equation come from the calculation of the source function. In the ideal case of LTE, we can assume that the source function behaves like the Planck function and can be calculated once we derive the temperature as a function of τ_ν.

We can change the coordinate system, where the optical depth is defined along the line of sight, to the direction of the stellar radius. This transformation will make use of the plane-parallel approximation. In spherical coordinates, if we choose the z-axes towards the observer, the radiative transfer equation becomes:

$$\frac{dI_\nu}{K_\nu \rho dz} = -I_\nu + S_\nu \tag{4.10}$$

and transforming to spherical coordinates, we have:

$$\frac{\partial I_\nu}{\partial r}\frac{\cos\theta}{K_\nu\rho} - \frac{\partial I_\nu}{\partial \theta}\frac{\sin\theta}{K_\nu \rho r} = -I_\nu + S_\nu \tag{4.11}$$

In case of thin atmospheres, the thickness of the atmosphere is small compared to the stellar radius and a plane-parallel approximation can be applied, where θ does not depend on z. Although this is not the case of super-giants, it is a very good approximation for solar-type stars. Then:

$$\cos\theta \frac{dI_\nu}{K_\nu \rho dr} = \cos\theta \frac{dI_\nu}{d\tau_\nu} = -I_\nu + S_\nu \tag{4.12}$$

where the optical depth is now defined along $dr(=\text{–}ds)$. Then Equation 4.9 becomes:

$$I_\nu(\tau_2) = I(\tau_1)e^{(\tau_1-\tau_2)\sec\theta} - \int_{\tau_1}^{\tau_2} S_\nu(t_\nu)e^{-(\tau_2-t_\nu)\sec\theta} \sec\theta dt_\nu \tag{4.13}$$

The solution of the RT equation requires boundary conditions, which are different for incoming ($\theta > 90°$) and outgoing ($\theta < 90°$) radiation.

$$\begin{aligned} I_\nu(\tau_\nu) &= I_\nu^{out}(\tau_\nu) + I_\nu^{in}(\tau_\nu) \\ &= \int_{\tau_\nu}^{\infty} S_\nu(t_\nu) e^{-(t_\nu - \tau_\nu)\sec\theta} \sec\theta dt_\nu \\ &\quad - \int_{0}^{\infty} S_\nu(t_\nu) e^{-(t_\nu - \tau_\nu)\sec\theta} \sec\theta dt_\nu \end{aligned} \tag{4.14}$$

At the stellar surface ($\tau_\nu = 0$), the incoming radiation is assumed zero and the outgoing radiation becomes:

$$I_\nu(\tau_\nu = 0) = I_\nu^{out}(\tau_\nu) = \int_0^\infty S_\nu(t_\nu) e^{-t_\nu \sec\theta} \sec\theta dt_\nu \tag{4.15}$$

We can now calculate the flux at the surface of the star from the specific intensity. From the definition of the flux in spherical coordinates with no azimuthal dependence, we have:

$$F_\nu = 2\pi \int_0^\pi I_\nu \cos\theta \sin\theta d\theta \tag{4.16}$$

Following the same analogy as with intensity, we consider only the outgoing flux.

$$\begin{aligned} F_\nu &= 2\pi \int_0^{\pi/2} I_\nu \cos\theta \sin\theta d\theta \\ &= 2\pi \int_0^{\pi/2} \int_0^\infty S_\nu(t_\nu) e^{-t_\nu \sec\theta} \sin\theta dt_\nu d\theta, \text{ if } S_\nu \text{ is isotropic} \\ &= 2\pi \int_0^\infty S_\nu(t_\nu) \int_0^{\pi/2} e^{-t_\nu \sec\theta} \sin\theta d\theta dt_\nu \\ &= 2\pi \int_0^\infty S_\nu(t_\nu) E_2(t_\nu) dt_\nu, \end{aligned} \tag{4.17}$$

where

$$E_2(t_\nu) = \int_0^{\pi/2} e^{-t_\nu \sec\theta} \sin\theta d\theta \quad = \int_1^\infty \frac{e^{-xw}}{x^2} dw. \tag{4.18}$$

Finally, assuming LTE for small volumes in the photosphere, the monochromatic flux is calculated:

$$F_\nu = 2\pi \int_0^\infty B_\nu(t_\nu) E_2(t_\nu) dt_\nu, \tag{4.19}$$

where B_ν is the Planck function. The above equation can be treated in many ways and different spectral synthesis codes have different approaches.

The spectral synthesis code of this work solves the RT equation numerically, using a Gaussian quadrature:

$$F_\nu = \sum_{n=1,N} B_\nu(\tau_i) w_i, \tag{4.20}$$

where τ_i and w_i are the quadrature nodes and weights respectively, calculated for orthogonal polynomials, for i=1, ..., 10. We have to note that B_ν is a function of temperature. The temperature in each depth scale can be obtained by the model atmospheres. Model atmospheres are calculated on a standard optical depth scale (usually at 5000Å). The problem can be solved if we convert the τ_i scale to the one of the model atmosphere (τ_{std}).

The conversion is accomplished by solving the first order equation:

$$\frac{d\tau_{std}}{d\tau_\nu} = \frac{K_{\lambda_{std}}(\tau_{std})}{K_{\lambda_\nu}(\tau_{std})} \tag{4.21}$$

The total absorption coefficients ($K_{\lambda_{std}}$ and K_{λ_ν}) are calculated from the model atmospheres (see next Section). The above equation is solved by SME iteratively with a Feautrier technique (Mihalas 1982).

To sum up, the monochromatic flux is derived at the surface of the photosphere, i.e. at $\tau_i = 0$. Next, the corresponding τ_{std} is calculated for each of the quadrature nodes i, from Equation 4.21. The Planck function is then calculated for the τ_i and with the temperature that is obtained from the model atmosphere. The $B_\nu(\tau_i)w_i$ is calculated for each increment till the 10^{th} order and summed for the total flux as in Equation 4.20.

4.1.2 Absorption coefficients

The transformation from τ_ν to τ_{std} requires the calculation of the absorption coefficients in the atmosphere of the star (Equation 4.21). The values of $K_{\tau_{std}}$ are directly provided from the model atmosphere. The absorption coefficient for other optical depth scales (K_{τ_ν}) has to be calculated separately.

Firstly, we need to define the two processes of absorption: 1) the continuous opacity absorption and 2) the line opacity absorption. Both the continuous opacity absorption coefficient (κ_{τ_ν}) and the line opacity absorption coefficient (α_{τ_ν}) are calculated for every optical depth increment and wavelength.

4.1.3 Line absorption coefficient

The line absorption coefficient is defined as the amount of energy absorbed from a beam of radiation with specific intensity I_ν, in a bound-bound transition process. This process involves: natural atomic absorption, pressure broadening, and thermal Doppler broadening.

Natural atomic absorption is caused by the interaction of light with dipoles. Due to that, the electrons oscillate as a harmonic oscillator with a damping constant. The shape of the line absorption coefficient for natural broadening per atom, α is described as:

$$\alpha_\nu = \frac{e^2}{mc} \frac{\gamma_{rad}/4\pi}{\Delta\nu^2 + (\gamma_{rad}/4\pi)^2} \tag{4.22}$$

The width of the broadening is described by the damping constant, γ_{rad}, that is also called radiation damping. The total energy absorbed for a quantum mechanical treatment is expressed:

$$\int_0^\infty \alpha d\nu = \frac{\pi e^2}{mc} f, \tag{4.23}$$

where f is the oscillator strength that is different for each transition and is related to the transition probability.

Pressure broadening is caused by the interaction between the atoms absorbing light and other particles such as ions, electrons, atoms or molecules. The atomic levels of the transitions of the absorbers are altered due to the perturbers. This distortion is a function of their separation, R. The change in energy induced by collision can be expressed in the form:

$$\Delta W = \text{constant}/\mathrm{R^n}, \tag{4.24}$$

where n depends on the type of interaction.

In case the perturbers are charged particles (ions, electrons), the collision process is called Quadratic Stark effect ($n = 4$). The numerical value of this collision is expressed:

$$\log \gamma_4 \approx 19 + \frac{2}{3} \log C_4 + \log P_e - \frac{5}{6} \log T, \tag{4.25}$$

where P_e is the electron pressure density and T the temperature (Gray 2005).

If the perturber is a neutral particle, such as neutral hydrogen that is dominant in cool stars, the perturbations are called van der Waals ($n = 6$) and is expressed by:

$$\log \gamma_6 \approx 20 + 0.4 \log C_6 + \log P_g - 0.7 \log T, \tag{4.26}$$

where P_g is the gas pressure density (Gray 2005). These approximations often underestimate the value of γ_6 and in these cases, an enhancement factor is introduced. In this work, we use the Unsöld factor that equals to 2.5 (Unsöld 1955).

We have to note that the pressure and thermal damping coefficient depends on the optical depth, whereas the radiation damping is constant throughout the atmosphere.

Thermal broadening is caused due to the motions of the atoms along the line of sight. These thermal motions are described by the Boltzmann velocity fields and cause Doppler shifts. The energy absorbed from a unit intensity is:

$$\alpha_\nu d\nu = \frac{\pi^{1/2}e^2}{mc} f \frac{1}{\Delta\nu_D} e^{-(\Delta\nu/\Delta\nu_D)^2} d\nu, \tag{4.27}$$

where ν_D is the Doppler frequency shift. Since the thermal motions are caused by Boltzmann velocities, v_0, the shift $\Delta\nu_D$ becomes:

$$\Delta\nu_D = \frac{v_0}{c}\nu_0 = \frac{\nu_0}{c}\left(\frac{2kT}{m}\right)^{1/2}, \tag{4.28}$$

with c the speed of light, and k the Boltzmann constant.

Other small scale motions can produce the same Doppler shifts as thermal motions. These effects are included in the above expression of the absorption coefficient by adding a velocity distribution of dispersion to the $\Delta\nu_D$ value. This velocity field is called microturbulence, ξ_t, as we saw in Sect. 2.5, and is described as following: $\Delta\nu_D = \frac{\nu_0}{c}(\frac{2kT}{m} + \xi^2)^{1/2}$.

To put everything in context, the line absorption coefficient is a result of the following processes: natural broadening, Stark broadening, van der Waals broadening, thermal, and microturbulence broadening. The first three broadening mechanisms show the same dispersion profile, which means that their damping constants can be combined in one profile: $\gamma = \gamma_{rad} + \gamma_4 + \gamma_6$. Therefore, we can convolve the new dispersion profile with the Gaussian profile of the ν_D dispersion. The convolution gives:

$$\begin{aligned} \alpha_\nu &= \frac{\pi e^2}{mc} f \frac{\gamma/4\pi^2}{\Delta\nu^2 + (\gamma/4\pi)^2} * \frac{1}{\pi^{1/2}\Delta\nu_D} e^{-(\Delta\nu/\Delta\nu_D)^2} \\ &= \frac{\pi^{1/2}e^2}{mc}\frac{f}{\Delta\nu_D} H(u,\alpha) \end{aligned} \tag{4.29}$$

where $H(u,\alpha)$ is the Hjerting function (Hjerting 1938) with

$$\begin{aligned} u &= \frac{\Delta\nu}{\Delta\nu_D} \\ \alpha &= \frac{\gamma}{4\pi}\frac{1}{\Delta\nu_D} \end{aligned} \tag{4.30}$$

The Hjerting function is similar to a Voigt function, $V(u,\alpha) = H(u,\alpha)/(\pi^{1/2}\Delta\nu_D)$, which is most often used.

4.1.4 Continuous absorption coefficient

The main processes that invoke continuous absorption in a stellar atmosphere are bound-free, free-free transitions and scattering. The main sources of absorption for both transition types are neutral hydrogen, negative hydrogen ion, hydrogen molecule, helium, and other metals (such as Si, Al, Ca, C, N, O).

In the visible region of cool stars, the continuous absorption coefficient (κ_ν) is dominated by the absorption of the negative hydrogen ion (H^-). The description of κ_ν due to H^- is:

$$\kappa \propto \text{constant}\, \mathrm{T}^{-5/2} \mathrm{P_e}\, \mathrm{e}^{0.75/\mathrm{kT}}, \tag{4.31}$$

where P_e is the electron pressure.

4.1.5 Disc integration

In order to match the flux of the synthetic spectrum with the observed one, additional steps have to be made. A necessary step is to integrate the above specific intensities over the stellar surface to construct the total disc flux.

SME divides the stellar disc into annuli of the same intensity and calculates the integration weights for each of them. The weight is just given by the relative area of each annulus, normalized such that the sum of all weights is unity. Each annulus is defined with a different angle, μ[1], of in total seven μ angles. Each intensity spectrum is convolved with a kernel which describes the distribution of rotational velocities present in the current annulus.

4.2 Convolution with velocity fields

The large scale velocity fields that introduce line broadening are macroturbulence (υ_{mac}) and the projected rotational velocity ($\upsilon \sin i$). In both cases, the υ_{mac} and $\upsilon \sin i$ profiles are convolved with the flux spectrum. Macroturbulence, in contrast to microturbulence, describes the motion in cells that are larger than the unit optical depth. There are several empirical correlations of υ_{mac} with other stellar parameters, such as temperature and surface gravity in the literature (e.g., Valenti & Fischer 2005; Doyle et al. 2014).

Another broadening mechanism not related with stellar physics, but the spectrograph itself, is the instrumental broadening. In our case, we use a Gaussian profile that is also convolved with the flux spectrum. Instrumental broadening depends on the resolution of the spectrograph. Now the final spectrum is ready to match the observations.

[1] μ is the $\cos\theta$, where θ is the angle between the outward intensity and the line of sight.

4.3 Best-fit parameters

SME includes the minimization procedure to find the best-fit parameters. In the spectral synthesis approach, the stellar parameters one can derive are the following: temperature, surface gravity, overall metallicity, microturbulence, macroturbulence, rotational velocity, radial velocity, and chemical abundances of individual elements. To do so, SME uses the Levenberg-Marquardt algorithm to solve for the least-squares problem:

$$\chi^2 = \sum \left(\frac{Obs - Model}{Unc} \right)^2 \frac{1}{N}, \tag{4.32}$$

where Obs is the observed spectrum, Unc is the uncertainty on the flux of the Obs, and N are the degrees of freedom (N = number of data points minus the free parameters). The Levenberg-Marquardt technique combines the gradient search for searches that approach the minimum from far away and the expansion method as the search converges.

4.4 Stellar parameters with synthesis

SME has been widely used in the community for the parameter determination of FGK and M stars. For instance, Valenti & Fischer (2005) analyzed a sample of 1040 solar-type stars of high-resolution spectra, using wavelength intervals as in Fig. 4.2. Additionally, the same code is used in the analysis of large samples for the GES.

Apart from large samples, SME is used in the characterization of numerous planet hosts (e.g., Pál et al. 2010; Bakos et al. 2012; Van Eylen et al. 2014). An interesting study of Torres et al. (2012) presents a uniform analysis of transit planet hosts. The stellar parameters are derived using the methodology of Valenti & Fischer (2005). The authors constrain surface gravity with the one derived directly from the transit light curve. A comparison between constrained and unconstrained parameters shows biases that come mainly from strong correlations between the constrained and unconstrained values of $T_{\rm eff}$, [Fe/H] with $\log g$ (see Fig. 4.3).

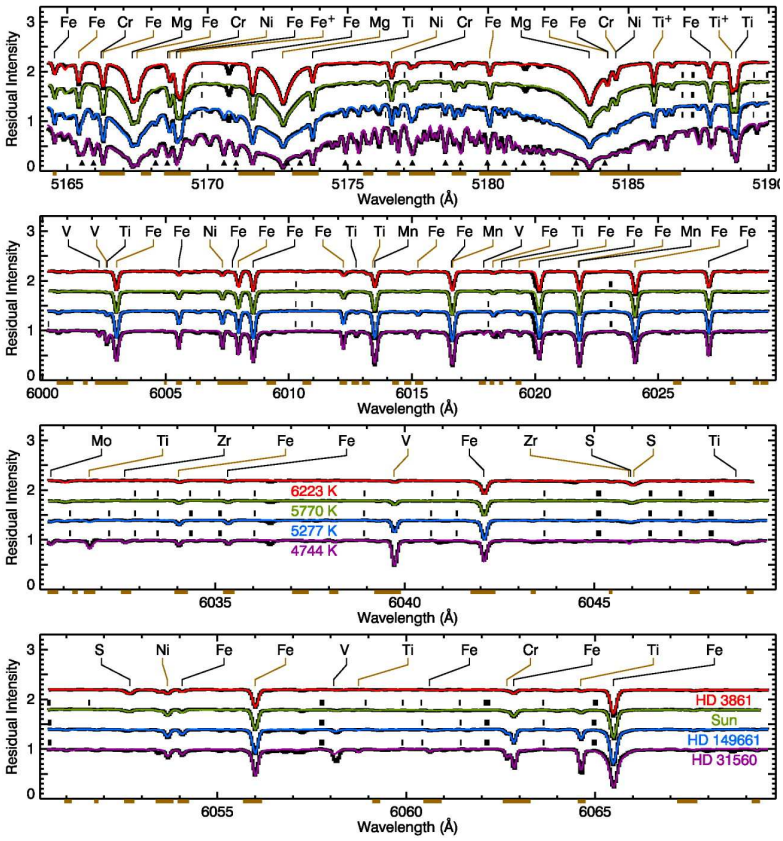

Figure 4.2: Observed and over-plotted synthetic spectra for some wavelength intervals. Bold horizontal line segments along the bottom axis demarcate spectral segments used to constrain synthetic spectrum fits. Taken from Valenti & Fischer (2005).

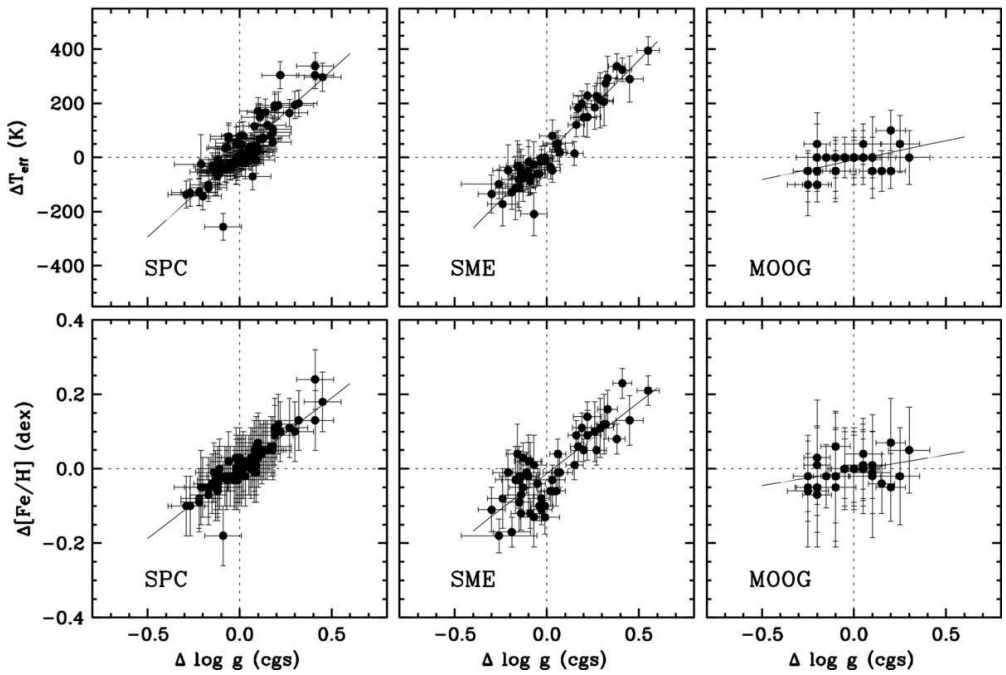

Figure 4.3: Impact on the temperatures and metallicities of fixing $\log g$ to the photometric values, for three different methods. The panels show the differences in the sense 'constrained minus unconstrained' as a function of the change in $\log g$. Taken from Torres et al. (2012).

CHAPTER 5

Stellar parameters for stars with moderate and fast rotation

"Waka waka waka waka waka waka waka waka waka."

Pacman

In this Chapter, I describe a new methodology specially designed to treat spectra of stars with moderate and fast rotation. I used the spectral package SME for this analysis and created a complete automatic procedure to derive precise stellar parameters for FGK dwarfs and giants. This work was published in Tsantaki et al. (2014).

5.1 Stars with moderate and fast rotation

The high quality stellar spectra obtained from RV planet search programs (e.g., Sousa et al. 2008, 2010), make spectroscopy a powerful tool for deriving the fundamental parameters in absence of more direct measurements. Direct measurements of stellar mass and radius can be derived from detached eclipsing binaries that are often accurate to 1-2%, providing direct $\log g$ determinations. Direct determinations of temperature are restricted only to stars with measurements of their angular diameter using the interferometric technique.

A typical method of deriving stellar parameters for solar-type stars, as we saw in previous Chapters, is based on the excitation and ionization equilibrium by measuring the EW of iron lines (hereafter the EW method). This method has successfully been applied to RV targets that are restricted to low rotational velocities ($v \sin i$) to increase the precision of the RV technique (Bouchy et al. 2001). High rotational velocities also limit the precision of the EW method. Spectral lines are broadened by rotation and therefore neighboring lines become blended, often unable to be resolved. Even though the EW is preserved, its correct measurement is not yet possible.

On the other hand, the transit planet hosts have a wider dispersion in rotational rates when comparing to the slowly rotating FGK hosts observed with the RV technique. For moderate and fast rotating stars, which may be the case of the transit targets, spectral synthesis is required for the parameter determination. This technique yields stellar parameters by fitting the observed spectrum with a synthetic one (e.g., Valenti & Fischer 2005; Malavolta et al. 2014) or with a library of pre-computed synthetic spectra (e.g., Recio-Blanco et al. 2006).

In this chapter, we propose a refined approach based on the spectral synthesis technique to derive stellar parameters for slowly rotating stars (Sect. 5.2), yielding results on the same scale with the homogeneous analysis of our previous works (Sect. 5.3). Our method is tested for a sample of moderate-to-high rotators (Sect. 5.4) and also to a number of planet hosts providing new stellar parameters. Their planetary properties are also revised (Sect. 5.5).

5.2 Spectroscopic analysis

Due to severe blending, measuring the EW of stars with high rotational velocity is very difficult, if not impossible (see Fig. 5.1). An approximate limit of the rotational velocity where the EW method provides reliable results, is up to $v \sin i$ ~12-15 $\mathrm{km\,s^{-1}}$ (depending on the choice of lines and spectral type).

5.2.1 Line list

For an accurate spectral synthesis, atomic and molecular data of all lines in the wavelength intervals where the synthesis is conducted must be as accurate as possible. The choice of intervals for our analysis is based on the line list of iron lines, as described in Tsantaki et al. (2013) (see also Chapter 3). This list is comprised of weak, isolated iron lines, specifically chosen from the extended line list of Sousa et al. (2008) to exclude blended lines that are commonly found in K-type stars. Effective temperatures derived with this line list are in agreement with the IRFM for the whole temperature regime of FGK dwarfs.

The spectral window around each iron line is set wide enough to include broadened lines of $v \sin i \sim 50\,\mathrm{km\,s^{-1}}$. Following the Doppler law, such a rotational velocity causes a broadening of ± 1 Å, around a line in the middle of the optical wavelength range (~ 5500 Å).

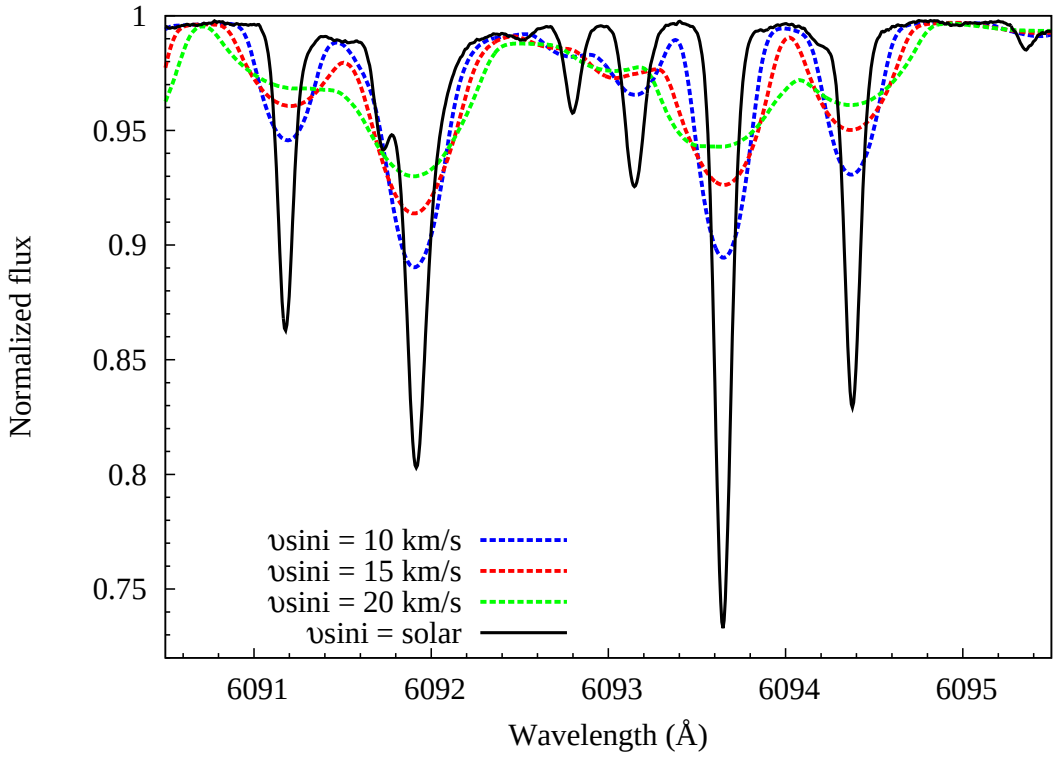

Figure 5.1: Solar absorption lines (black), broadened by different rotational profiles: $10\,\mathrm{km\,s^{-1}}$ (blue), $15\,\mathrm{km\,s^{-1}}$ (red), and $20\,\mathrm{km\,s^{-1}}$ (green). Blending at these rates due to rotation makes the accurate measurement of the EW very difficult.

The original line list contains 137 Fe I and Fe II lines where we set intervals of 2 Å around them. The atomic data for these intervals were obtained from the VALD (Piskunov et al. 1995; Kupka et al. 1999). We extracted atomic data for all the expected transitions for a star with solar atmospheric parameters for our wavelength intervals. We also included lines predicted for a K-type star with $T_{\mathrm{eff}} = 4400\,\mathrm{K}$. The two line lists that correspond to atomic transitions for the two different spectral types were merged into one after removing duplicates. Molecular data of the most abundant molecules in solar-type stars (C_2, CN, OH, and MgH) were also obtained from VALD using the same requests as for the atomic data.

From the above intervals we selected the optimal ones according to the following procedure. From the first analyses, we noticed that K-type stars show the highest residuals between the observed and the best-fit synthetic spectrum compared to the F and G spectral types. The main reason is that the spectra of K-type stars include numerous lines, but not all appear in our line list after the requested atomic data queries. Therefore, we discarded lines in the bluer part (below 5000 Å) where lines are more crowded. Lines within overlapping intervals were merged into one.

In addition, we checked the behaviour of the remaining lines due to rotation by using the Sun as a reference star convolved with moderate rotation of $20\,\mathrm{km\,s^{-1}}$ (see Sect. 5.4). We excluded lines by eye when there was strong contamination by neighboring lines due to broadening and chopped the intervals were the contamination in the edges was weak. We also excluded lines that showed high residuals between the spectrum and the synthesized one for the solar parameters. The initial choice of spectral windows was double the length, i.e. 4 Å where the iron lines were placed in the center. For this length, the best-fit parameters for the Sun (low rotation) were accurate. However, the parameters for the solar spectrum convolved with rotation (again of $20\,\mathrm{km\,s^{-1}}$) showed higher deviation ($T_{\rm eff}$ = 5728 K, $\log g$ = 4.39 dex, [Fe/H] = –0.03 dex) compared to the standard solar values. For this reason we limited the length of the intervals to 2 Å.

In addition to blending caused by high rotation, another considerable problem that limits this procedure is the difficulty in distinguishing between the line and the continuum points when the lines become very shallow. In this case, the wings of the lines are miscalculated as continuum, leading to the biases discussed in Sect. 5.4.

Taking all the above into consideration, the final line list is comprised of 47 Fe I and 4 Fe II lines into 42 wavelength intervals, summing a total of 537 lines of different species. The wavelength intervals and the atomic data of the iron lines are presented in Table 5.1.[1]

Atomic data are usually calculated from laboratory or semi-empirical estimates. To avoid uncertainties that may arise from these estimations, we determine astrophysical values for the basic atomic and molecular line data, namely for the oscillator strengths ($\log gf$) and the van der Waals damping parameters (γ_6). We used the National Solar Observatory Atlas (Kurucz et al. 1984) to improve the transition probabilities and the broadening parameters of our line list in an inverted analysis using fixed the typical solar parameters (as adopted by Valenti & Fischer 2005): $T_{\rm eff} = 5770\,\mathrm{K}$, $\log g = 4.44\,\mathrm{dex}$, $[Fe/H] = 0.0\,\mathrm{dex}$, $\xi_t = 0.87\,\mathrm{km\,s^{-1}}$, $\upsilon_{mac} = 3.57\,\mathrm{km\,s^{-1}}$, $\log_\epsilon(\mathrm{Fe}) = 7.50\,\mathrm{dex}$).

5.2.2 Initial conditions

All minimization algorithms depend on the initial conditions. In order to make sure that the convergence is achieved for the global minimum, we set the initial conditions as close to the expected ones as possible. For temperature, we use the calibration of Valenti & Fischer (2005) as a function of $B-V$ color. Surface gravities are calculated using *Hipparcos* parallaxes (van Leeuwen 2007), V magnitudes, bolometric corrections based on Flower (1996) and Torres (2010), and solar magnitudes from (Bessell et al. 1998). In cases the parallaxes are not available, we use the literature values. Masses are set to solar value.

Microturbulence is used to remove possible trends in parameters due to model deficiencies. It has been shown that ξ_t correlates mainly with $T_{\rm eff}$ and $\log g$ for FGK stars (e.g., Nissen 1981; Adibekyan et al. 2012b; Ramírez et al. 2013). We therefore, set ξ_t

[1]The complete line list is uploaded online in SME format at http://mariatsantaki.weebly.com/sme-line-list.html.

Table 5.1: Spectral wavelength intervals and line data used for the spectroscopic analysis.

Intervals Å	λ Å	Species	χ_{ex} (eV)	$\log gf$	γ_6
5521.45 - 5523.45	5522.45	Fe I	4.21	-1.484	-7.167
5559.22 - 5561.11	5560.22	Fe I	4.43	-0.937	-7.507
5632.95 - 5634.95	5633.95	Fe I	4.99	-0.186	-7.391
5648.99 - 5652.47	5649.99	Fe I	5.10	-0.649	-7.302
...	5651.47	Fe I	4.47	-1.641	-7.225
...	5652.32	Fe I	4.26	-1.645	-7.159
5678.03 - 5680.97	5679.03	Fe I	4.65	-0.657	-7.320
...	5680.24	Fe I	4.19	-2.347	-7.335
5719.90 - 5721.90	5720.90	Fe I	4.55	-1.743	-7.136
5792.92 - 5794.92	5793.92	Fe I	4.22	-2.038	-7.304
5810.92 - 5812.92	5811.92	Fe I	4.14	-2.323	-7.951
5813.81 - 5815.45	5814.81	Fe I	4.28	-1.720	-7.269
...	5815.22	Fe I	4.15	-2.521	-7.038
5852.15 - 5854.15	5852.22	Fe I	4.55	-1.097	-7.201
...	5853.15	Fe I	1.49	-5.006	-6.914
5861.36 - 5863.36	5862.36	Fe I	4.55	-0.186	-7.572
5986.07 - 5988.07	5987.07	Fe I	4.79	-0.428	-7.353
6004.55 - 6006.55	6005.55	Fe I	2.59	-3.437	-7.352
6088.57 - 6090.57	6089.57	Fe I	4.58	-1.165	-7.527
6119.25 - 6121.25	6120.25	Fe I	0.92	-5.826	-7.422
6126.91 - 6128.78	6127.91	Fe I	4.14	-1.284	-7.687
6148.25 - 6150.25	6149.25	Fe II	3.89	-2.786	-7.478
6150.62 - 6152.62	6151.62	Fe I	2.18	-3.188	-7.729
6156.73 - 6158.73	6157.73	Fe I	4.08	-1.097	-7.691
6172.65 - 6174.19	6173.34	Fe I	2.22	-2.775	-7.829
6225.74 - 6227.40	6226.74	Fe I	3.88	-2.021	-7.423
6231.65 - 6233.65	6232.65	Fe I	3.65	-1.161	-7.552
6237.00 - 6239.38	6238.39	Fe II	3.89	-2.693	-7.359
6321.69 - 6323.69	6322.69	Fe I	2.59	-2.314	-7.635
6334.34 - 6336.34	6335.34	Fe I	2.20	-2.323	-7.735
6357.68 - 6359.68	6358.68	Fe I	0.86	-4.225	-7.390
6431.83 - 6433.05	6432.69	Fe II	2.89	-3.650	-7.391
6455.39 - 6457.02	6456.39	Fe II	3.90	-2.175	-7.682
6480.88 - 6482.88	6481.88	Fe I	2.28	-2.866	-7.627
6626.55 - 6628.55	6627.55	Fe I	4.55	-1.400	-7.272
6645.94 - 6647.50	6646.94	Fe I	2.61	-3.831	-7.141
6698.15 - 6700.15	6699.15	Fe I	4.59	-2.004	-7.162
6704.11 - 6706.11	6705.11	Fe I	4.61	-1.088	-7.539
6709.32 - 6711.32	6710.32	Fe I	1.49	-4.732	-7.335
6724.36 - 6727.67	6725.36	Fe I	4.10	-2.093	-7.302
...	6726.67	Fe I	4.61	-0.951	-7.496
6731.07 - 6732.50	6732.07	Fe I	4.58	-2.069	-7.130
6738.52 - 6740.52	6739.52	Fe I	1.56	-4.797	-7.685
6744.97 - 6746.97	6745.11	Fe I	4.58	-2.047	-7.328
...	6745.97	Fe I	4.08	-2.603	-7.422
6839.23 - 6840.84	6839.84	Fe I	2.56	-3.304	-7.567
6854.72 - 6856.72	6855.72	Fe I	4.61	-1.885	-7.253
6856.25 - 6859.15	6857.25	Fe I	4.08	-1.996	-7.422
...	6858.15	Fe I	4.61	-0.941	-7.344
6860.94 - 6862.94	6861.94	Fe I	2.42	-3.712	-7.580
...	6862.50	Fe I	4.56	-1.340	-7.330

according to the correlation discussed in the work of Tsantaki et al. (2013) for a sample of FGK dwarfs. For the giant stars in our sample, we use the empirical calibration of Mortier et al. (2013a) based on the results of Hekker & Meléndez (2007).

Macroturbulence is a broadening mechanism that also correlates with $T_{\rm eff}$ (e.g., Saar & Osten 1997). We set υ_{mac} in our analysis following the relation of Valenti & Fischer (2005). Initial metallicity ($[M/H]$) is set to solar and initial rotational velocity to $0.5\,{\rm km\,s^{-1}}$.

5.2.3 Spectral synthesis

The spectral synthesis package we use for this analysis is Spectroscopy Made Easy (SME), version 3.3 (Valenti & Piskunov 1996). Modifications from the first version are described in Valenti et al. (1998) and Valenti & Fischer (2005). The adopted model atmospheres are generated by the ATLAS9 program (Kurucz 1993) and LTE is assumed. In our case, the free parameters are: $T_{\rm eff}$, $\log g$, $[M/H]$, and $\upsilon \sin i$. Metallicity in this work refers to the average abundance of all elements producing absorption in our spectral regions. We can safely assume that $[M/H]$ approximately equals to $[Fe/H]$ for our sample of stars as the dominant lines in our regions are the iron ones. Additionally, these stars are not very metal-poor ($>$ –0.58 dex). The overall metallicity in metal-poor stars is enhanced by other elements (relative to iron) and in that case the previous assumption does not hold (e.g., Adibekyan et al. 2012c).

After a first iteration with the initial conditions described above, we use the output set of parameters to derive stellar masses using the Padova models (da Silva et al. 2006). Surface gravity is then re-derived with the obtained mass and temperature. The values of ξ_t and υ_{mac} are also updated by the new $T_{\rm eff}$ and $\log g$. The final results are obtained after a second iteration with the new initial values. Additional iterations were not required, as the results between the first and second iteration in all cases were very close (for instance the mean differences for the sample in Sect. 5.4 are: $\Delta T_{\rm eff} = 24\,{\rm K}$, $\Delta \log g = 0.06\,{\rm dex}$, $\Delta[{\rm Fe/H}] = 0.003\,{\rm dex}$, and $\Delta \upsilon \sin i = 0.18\,{\rm km\,s^{-1}}$).

5.2.4 Internal error analysis

Estimation of the errors is a complex problem for this analysis. One approach is to calculate the errors from the covariance matrix of the best fit solution. Usually these errors are underestimated and do not include deviations depending on the specific choice of initial parameters nor the choice of the wavelength intervals. On the other hand, Monte Carlo approximations are computational expensive when we are dealing with more than a handful of stars. In this section we explore the contribution of different type of errors for reference stars of different spectral types. The errors of these stars will be representative of the errors of the whole group that each one belongs.

We select 3 slow rotating stars of different spectral types: F (HD 61421), G (Sun), and K (HD 20868) as our references. We convolve each of these stars with different rotational profiles (initial, 15, 25, 35, 45, and $55\,{\rm km\,s^{-1}}$) to quantitatively check the errors attributed to different $\upsilon \sin i$ (see also Sect. 5.4).

Our aim is to calculate the errors from two different sources: 1) the initial conditions, and 2) the choice of wavelength intervals. Firstly, we check how the initial parameters affect the convergence to the correct ones. For each star we set different initial parameters by changing: $T_{\rm eff}$ $\pm$ 100 K, $\log g$ $\pm$ 0.20 dex, $[Fe/H]$ $\pm$ 0.10 dex, and $\upsilon \sin i$ $\pm$ 0.50 $\mathrm{km\,s^{-1}}$. We calculate the parameters for the total 81 permutations of the above set of initial parameters. This approach is also presented in Valenti & Fischer (2005) for their solar analysis.

The choice of wavelength intervals is also important for the precise determination of stellar parameters. The spectral range of different instruments varies and therefore not all wavelength intervals of a specific line list can be used for the parameter determination. Moreover, there are often other reasons for which discarding a wavelength interval would be wise, such as the presence of cosmic rays. In these cases, the errors which are attributed to the discarded wavelength intervals from a defined line list can give an estimation on the homogeneity of our parameters.

We account for such errors by randomly excluding 10% of our total number of intervals (that leaves us with 38 intervals). This percentage is approximately expected for the above cases. Stellar parameters are calculated for the shortened list of intervals and this procedure is repeated 100 times (each time discarding a random 10%). The error of each free parameter is defined as the standard deviation of the results of all repetitions.

For our analysis, we do not include the errors derived from the convariance matrix. The primary reason is that the flux errors of each wavelength element that are required for the precise calculation of the convariance matrix, unfortunately, are not provided for our spectra. Therefore, in such cases one has to be careful with the interpretation of the values of the covariance matrix.

Table 5.2 shows the errors derived from the two different sources described above. The errors in $T_{\rm eff}$ and $\log g$ due to the different initial parameters are slightly more significant, whereas for $[Fe/H]$ and $\upsilon \sin i$ both type of errors are comparable. Finally, we add Quadratically the 2 sources of errors that are described above (see Table 5.3). We notice that for higher $\upsilon \sin i$, the uncertainties in all parameters become higher as one would expect. K-type stars have also higher uncertainties compared to F- and G-types. In particular, the uncertainties in $\upsilon \sin i$, for K-type stars, are significantly high for $\upsilon \sin i > 45\,\mathrm{km\,s^{-1}}$. Fortunately, K-type stars are typically low rotators since rotational velocity decreases with the spectral type for FGK stars (e.g., Gray 1984; Nielsen et al. 2013).

Table 5.2: Internal error analysis for each spectral type and different rotational velocities. Two sources of errors were considered: Initial parameters and Wavelength choice (dependence on the choice of the 90% of the total intervals). Rotational velocity $0\,\mathrm{km\,s^{-1}}$ refers to the intrinsic $v \sin i$ of the star.

Parameters	F-type (HD 61421)											
	Initial parameters						Wavelength choice					
$v \sin i$	$0\,\mathrm{km\,s^{-1}}$	$15\,\mathrm{km\,s^{-1}}$	$25\,\mathrm{km\,s^{-1}}$	$35\,\mathrm{km\,s^{-1}}$	$45\,\mathrm{km\,s^{-1}}$	$55\,\mathrm{km\,s^{-1}}$	$0\,\mathrm{km\,s^{-1}}$	$15\,\mathrm{km\,s^{-1}}$	$25\,\mathrm{km\,s^{-1}}$	$35\,\mathrm{km\,s^{-1}}$	$45\,\mathrm{km\,s^{-1}}$	$55\,\mathrm{km\,s^{-1}}$
T_{eff} (K)	27	43	48	54	97	108	13	9	17	48	16	85
$\log g$ (dex)	0.11	0.15	0.21	0.25	0.20	0.17	0.02	0.02	0.08	0.16	0.03	0.05
$[Fe/H]$ (dex)	0.03	0.04	0.05	0.07	0.06	0.07	0.01	0.01	0.02	0.04	0.01	0.01
$v \sin i$ ($\mathrm{km\,s^{-1}}$)	0.20	0.25	0.98	1.00	1.57	2.60	0.08	0.14	0.91	0.89	0.93	2.13
	G-type (Sun)											
	Initial parameters						Wavelength choice					
$v \sin i$	$0\,\mathrm{km\,s^{-1}}$	$15\,\mathrm{km\,s^{-1}}$	$25\,\mathrm{km\,s^{-1}}$	$35\,\mathrm{km\,s^{-1}}$	$45\,\mathrm{km\,s^{-1}}$	$55\,\mathrm{km\,s^{-1}}$	$0\,\mathrm{km\,s^{-1}}$	$15\,\mathrm{km\,s^{-1}}$	$25\,\mathrm{km\,s^{-1}}$	$35\,\mathrm{km\,s^{-1}}$	$45\,\mathrm{km\,s^{-1}}$	$55\,\mathrm{km\,s^{-1}}$
T_{eff} (K)	12	5	18	86	86	147	13	9	21	36	43	116
$\log g$ (dex)	0.06	0.05	0.09	0.16	0.11	0.14	0.01	0.03	0.07	0.07	0.07	0.12
$[Fe/H]$ (dex)	0.02	0.01	0.04	0.07	0.07	0.07	0.02	0.01	0.03	0.02	0.02	0.04
$v \sin i$ ($\mathrm{km\,s^{-1}}$)	0.25	0.09	0.32	0.36	2.47	3.67	0.11	0.99	0.26	0.17	2.29	3.49
	K-type (HD 20868)											
	Initial parameters						Wavelength choice					
$v \sin i$	$0\,\mathrm{km\,s^{-1}}$	$15\,\mathrm{km\,s^{-1}}$	$25\,\mathrm{km\,s^{-1}}$	$35\,\mathrm{km\,s^{-1}}$	$45\,\mathrm{km\,s^{-1}}$	$55\,\mathrm{km\,s^{-1}}$	$0\,\mathrm{km\,s^{-1}}$	$15\,\mathrm{km\,s^{-1}}$	$25\,\mathrm{km\,s^{-1}}$	$35\,\mathrm{km\,s^{-1}}$	$45\,\mathrm{km\,s^{-1}}$	$55\,\mathrm{km\,s^{-1}}$
T_{eff} (K)	20	52	54	77	130	127	15	47	45	68	110	110
$\log g$ (dex)	0.09	0.16	0.17	0.20	0.14	0.18	0.03	0.11	0.12	0.16	0.10	0.09
$[Fe/H]$ (dex)	0.02	0.06	0.09	0.09	0.09	0.09	0.02	0.05	0.07	0.07	0.02	0.01
$v \sin i$ ($\mathrm{km\,s^{-1}}$)	0.46	0.72	0.86	2.38	6.92	7.54	0.45	0.69	0.77	2.12	6.98	7.36

Table 5.3: Errors summed Quadratically for each spectral type and for the different rotational velocities.

Parameters	F-type (HD 61421)					
$v \sin i$	0 km s^{-1}	15 km s^{-1}	25 km s^{-1}	35 km s^{-1}	45 km s^{-1}	55 km s^{-1}
$T_{\rm eff}$ (K)	30	44	51	72	98	137
$\log g$ (dex)	0.11	0.15	0.22	0.30	0.20	0.18
$[Fe/H]$ (dex)	0.03	0.04	0.05	0.03	0.08	0.06
$v \sin i$ (km s^{-1})	0.22	0.29	1.34	1.34	1.82	3.36
	G-type (Sun)					
$v \sin i$	0 km s^{-1}	15 km s^{-1}	25 km s^{-1}	35 km s^{-1}	45 km s^{-1}	55 km s^{-1}
$T_{\rm eff}$ (K)	18	10	28	93	96	187
$\log g$ (dex)	0.06	0.06	0.11	0.17	0.13	0.18
$[Fe/H]$ (dex)	0.03	0.01	0.05	0.07	0.07	0.08
$v \sin i$ (km s^{-1})	0.27	0.99	0.41	0.40	3.37	5.06
	K-type (HD 20868)					
$v \sin i$	0 km s^{-1}	15 km s^{-1}	25 km s^{-1}	35 km s^{-1}	45 km s^{-1}	55 km s^{-1}
$T_{\rm eff}$ (K)	25	70	70	103	170	168
$\log g$ (dex)	0.09	0.19	0.21	0.26	0.17	0.20
$[Fe/H]$ (dex)	0.03	0.08	0.11	0.11	0.09	0.09
$v \sin i$ (km s^{-1})	0.64	0.99	1.15	3.19	9.83	10.54

5.3 Spectroscopic parameters for slowly rotating FGK stars

To test the effectiveness of the line list, we used a sample of 48 FGK stars (40 dwarfs and 8 giants) with low rotation rates, high S/N, and high resolution spectra, most of them taken from the archival data of HARPS (R $\sim$ 110000) and the rest with UVES (R $\sim$ 110000), and FEROS (R $\sim$ 48000) spectrographs. Their stellar parameters range from $4758 \leq T_{\rm eff} \leq 6666$ K, $2.82 \leq \log g \leq 4.58$ dex, and –0.58 $\leq$ [Fe/H] $\leq$ 0.33 dex, and they are derived following the method described in Sect. 5.2. Figure 5.2 depicts the comparison between the parameters derived in this work and the EW method. All parameters from the EW method were taken from Sousa et al. (2008), Mortier et al. (2013a,b), Tsantaki et al. (2013), and Santos et al. (2013) using the same methodology to provide the best possible homogeneity for the comparison. The differences between these methods are presented in Table 5.4 and the stellar parameters in Tables C.1- C.2.

Table 5.4: Differences in stellar parameters between this work and the EW method for the 48 sample stars. MAD values correspond to the median average deviation and are indicated in parenthesis. N is the number of stars used for the comparison.

This Work – EW	$\Delta T_{\rm eff}$[a] ($\pm$ MAD) K	$\Delta \log g$ ($\pm$ MAD) dex	Δ [Fe/H] ($\pm$ MAD) dex	N
Whole sample	–26 ± 14 (± 55)	–0.19 ± 0.04 (± 0.14)	0.000 ± 0.010 (± 0.041)	48
F-type	–97 ± 22 (± 68)	–0.34 ± 0.07 (± 0.18)	0.006 ± 0.014 (± 0.014)	12
G-type	7 ± 16 (± 36)	–0.07 ± 0.05 (± 0.04)	0.019 ± 0.021 (± 0.032)	18
K-type	–5 ± 27 (± 32)	–0.18 ± 0.05 (± 0.16)	–0.027 ± 0.016 (± 0.042)	18

[a]The standard errors of the mean (σ_M) are calculated with the following formula: $\sigma_M = \frac{\sigma}{\sqrt{N}}$, σ being the standard deviation.

The effective temperatures derived with the spectral synthesis technique and the EW method are in good agreement. The greatest discrepancies appear for $T_{\rm eff} > 6000\,{\rm K}$, where the effective temperature derived from this work is systematically cooler. The same systematics are also presented in Molenda-Żakowicz et al. (2013), where the authors compare the EW method with other spectral synthesis techniques but the explanation for these discrepancies is not yet clear.

The values of metallicity are in very good agreement between the two methods with zero mean differences and 0.04 dex median average deviation.

Surface gravity is a parameter that is the most difficult to constrain with spectroscopy. The comparison of the two methods shows a considerable offset of 0.19 dex, where $\log g$ is underestimated compared to the EW method. Interestingly, this offset is smaller for giant stars ($\Delta \log g = 0.07\,{\rm dex}$) than for dwarfs ($\Delta \log g = -0.24\,{\rm dex}$).

To further investigate these differences, we compare the spectroscopic $\log g$ with surface gravity derived with another method that is less model dependent. For 16 dwarf stars in our sample that have a transiting planet, surface gravity can be derived from the analysis of the transit light curve (see also Sect. 5). We compare $\log g$ derived from the transit light curve with the spectroscopic $\log g$ from the EW method (both values are taken from Mortier et al. (2013b)) and this work (see Fig. 5.3).

We show that $\log g$ from the EW analysis is overestimated for low $\log g$ values and underestimated for high $\log g$ values. Fortunately, this trend does not affect $T_{\rm eff}$ and $[Fe/H]$, as shown in the recent work of Torres et al. (2012). The same systematics were also found between the $\log g$ from the EW method and the $\log g$ derived with the *Hipparcos* parallaxes for solar-type stars in Tsantaki et al. (2013) and Bensby et al. (2014). These results imply that $\log g$ from the EW method using iron lines suffers from biases, but the explanation is not clear.

On the other hand, $\log g$ derived from this work is in very good agreement with the transit $\log g$, for values lower than 4.5 dex. Stars with $\log g > 4.5\,{\rm dex}$ correspond to the cooler stars and are also underestimated. The reason for this underestimation is not yet known, so further investigation is required to understand this behavior.

Despite the differences for the $\log g$ values of mainly the F-type stars, the results listed in Table 5.4 show that for slowly rotating FGK stars, stellar parameters derived from both methods are on the same scale. This means that for the whole sample, the residuals between both methods are small and of the same order of magnitude as the errors of the parameters.

5.4 Spectroscopic parameters for fast rotating FGK stars

Testing our method for slow FGK rotators does not necessary imply that it will work for higher $\upsilon \sin i$ where spectral lines are much more broadened and shallower. Our goal is to examine how efficient our method is for stars with moderate-to-high rotation rates. For this purpose, we derived stellar parameters for reference stars of different spectral type and with low $\upsilon \sin i$. Second, these stars are convolved with a set of rotational

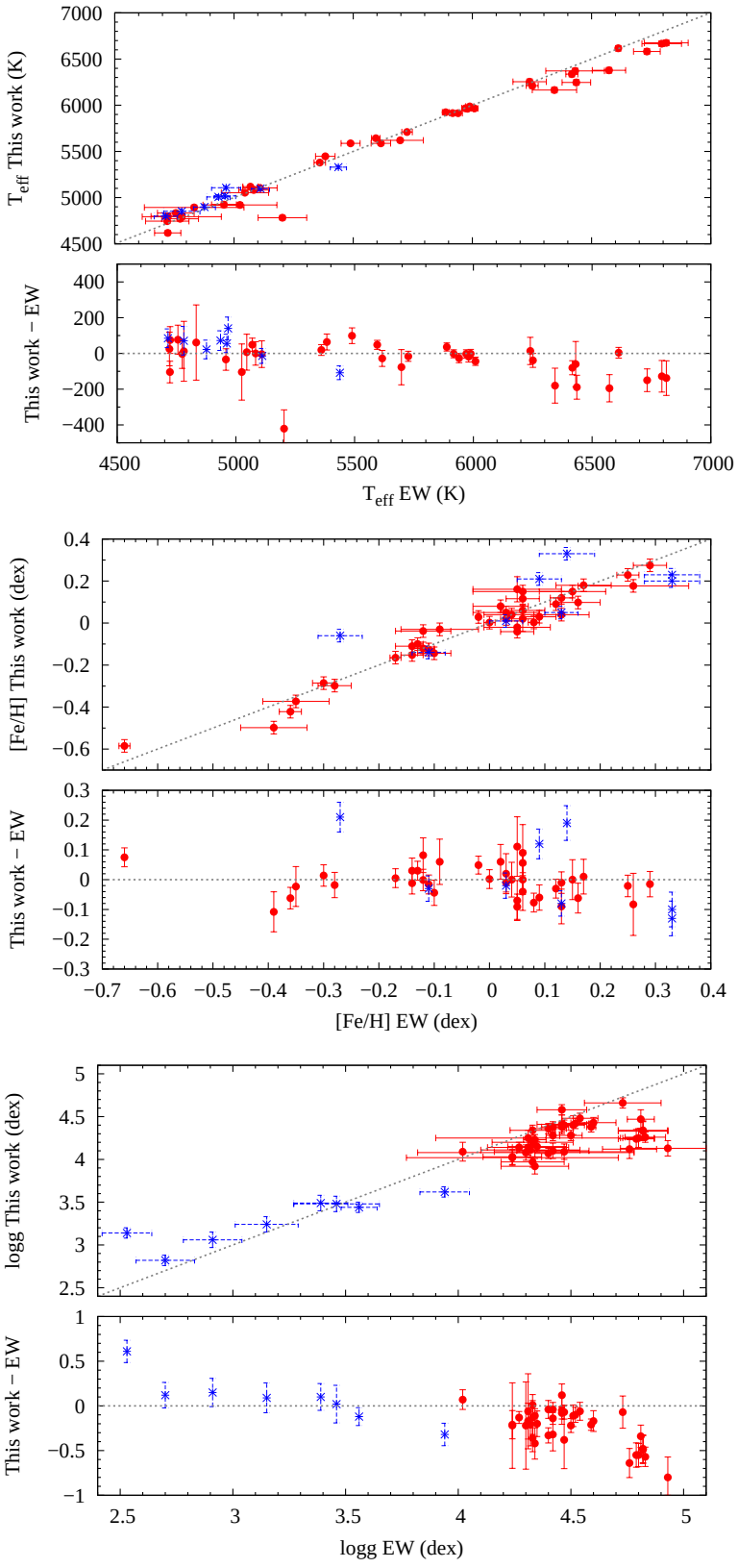

Figure 5.2: Comparison between the parameters derived using the spectral synthesis method (This Work) and the results of our EW method: temperature (top panel), metallicity (middle panel) and surface gravity (bottom panel). Filled circles represent dwarf stars and asterisks giants.

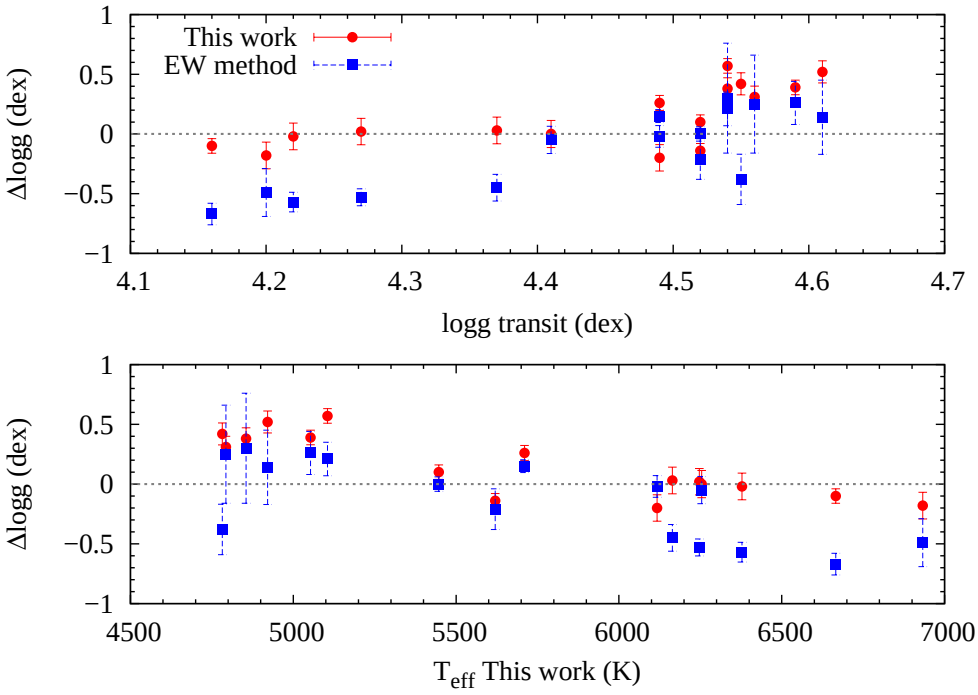

Figure 5.3: Comparison of surface gravity derived from the transit fit with this work and the EW method. $\Delta \log g$ represents 'transit minus this work' (red circles) and 'transit minus EW method' (blue squares).

profiles using the `rotin3` routine as part of the SYNSPEC synthesis code[2] (Hubeny et al. 1994). As a result, each star has eight different rotational velocities (initial, 5, 10, 15, 20, 25, 30, 40, 50 $\mathrm{km\,s^{-1}}$). Stellar parameters of all rotational profiles were calculated to investigate how they differ from the non-broadened (unconvolved) star. This test is an indication of how the accuracy of our method is affected by adding a rotational profile.

The selected reference stars are two F-type, one G-type, and four K-type stars, and they are presented in boldface in Table C. Probably one star per spectral type would be enough, but we included more F- and K-type stars because they showed higher uncertainties (especially the K-type stars). In Figs. 5.4- 5.6, we show the differences of stellar parameters between the stars with the unconvolved values (original $v \sin i$), and the convolved ones for the eight different rotational velocities.

As $v \sin i$ increases, K-type stars show the highest differences in the stellar parameters compared to the non-broadened profile. These deviations for high $v \sin i$ are also shown in the error analysis of Sect. 5.2.4. The temperatures of these stars are systematically underestimated with increasing $v \sin i$. On the other hand, the parameters of F- and G-type stars are very close to the ones with low rotation, and no distinct trends are observed with rotation. Even for very high $v \sin i$, temperature and metallicity can be

[2]http://nova.astro.umd.edu/Synspec43/

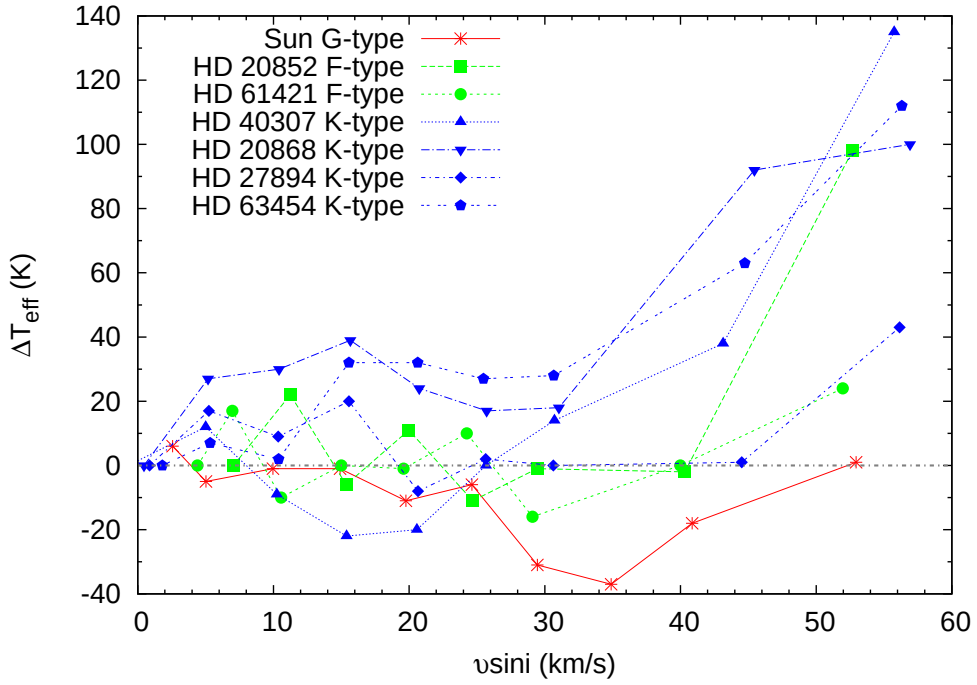

Figure 5.4: Differences in temperature (initial $v \sin i$ minus the different rotational profiles) versus $v \sin i$. Each star is represented with different symbol and each spectral type is represented with different colour. Blue for K-type, red for G-type and green F-type. The initial $v \sin i$ is different for each star.

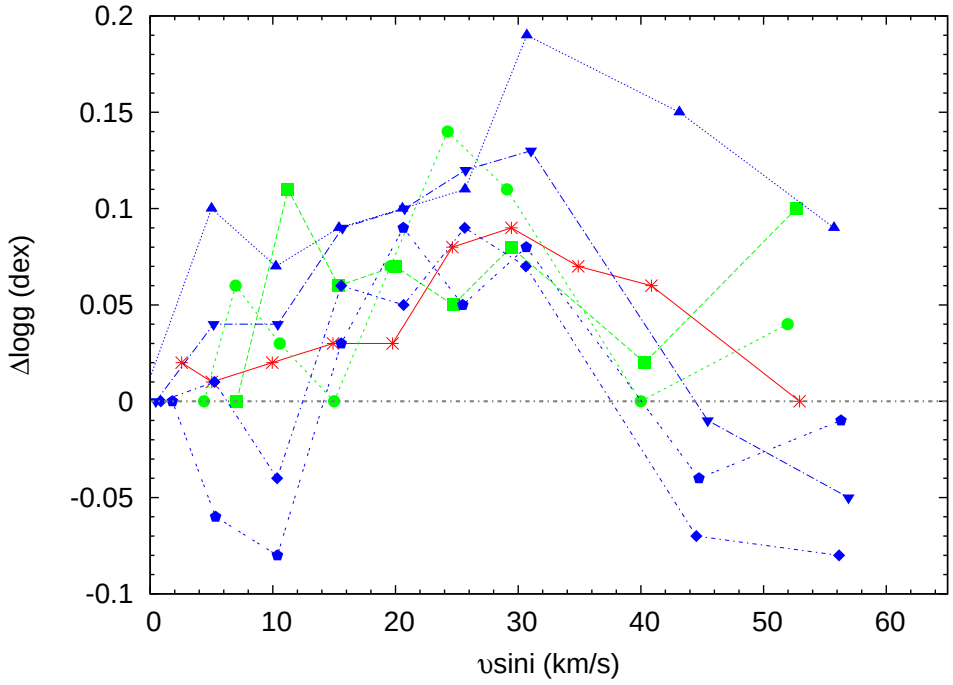

Figure 5.5: Differences in surface gravity (initial $v \sin i$ minus the different rotational profiles) versus $v \sin i$. Each star is represented with different symbol and each spectral type is represented with different colour. Blue for K-type, red for G-type and green F-type. The initial $v \sin i$ is different for each star.

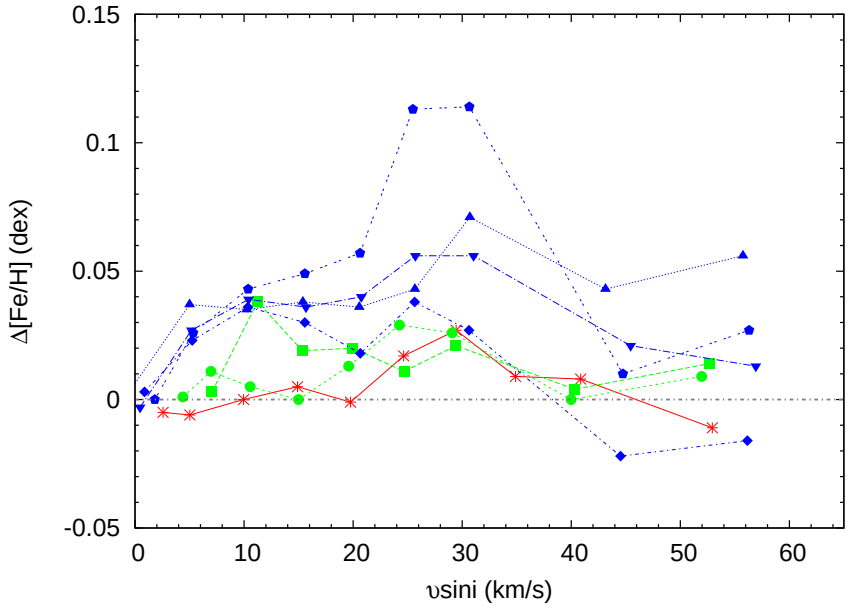

Figure 5.6: Differences in metallicity (initial $v \sin i$ minus the different rotational profiles) versus $v \sin i$. Each star is represented with different symbol and each spectral type is represented with different colour. Blue for K-type, red for G-type and green F-type. The initial $v \sin i$ is different for each star.

derived with differences in values of less than 100 K and 0.05 dex respectively. Surface gravity, however, shows large differences that reach up to ∼0.20 dex.

The above discrepancies in the parameters in turn affect the stellar mass and radius. To investigate these offsets, we calculate the mass and radius for all the rotational velocities using the calibration of Torres et al. (2010) but corrected for small offsets to match masses derived from isochrone fits by Santos et al. (2013). The results in Fig. 5.7 show that the mass hardly changes as $v \sin i$ increases. The stellar radius, however, is affected in the same manner as surface gravity with greater radius differences. For example, the maximum difference in $\log g$ (∼0.20 dex) causes a deviation in radius of $0.39\,R_{\odot}$.

5.4.1 Application to FGK fast rotators

We selected a sample of FGK dwarfs with moderate-to-high $v \sin i$, which have available several estimates of their parameters with $v \sin i$ up to $54\,km\,s^{-1}$ that have spectra available in the public archives of different high resolution instruments (HARPS, FEROS, ELODIE, and CORALIE). The spectra were already processed with their standard pipeline procedures. We corrected for the radial velocity shifts and in cases of multiple observations, the spectra were summed using the `IRAF` tools, `dopcor` and `scombine`.

We derived the stellar parameters with the method in this work, and the results and literature values of the sample are presented in methods used: other spectral synthesis

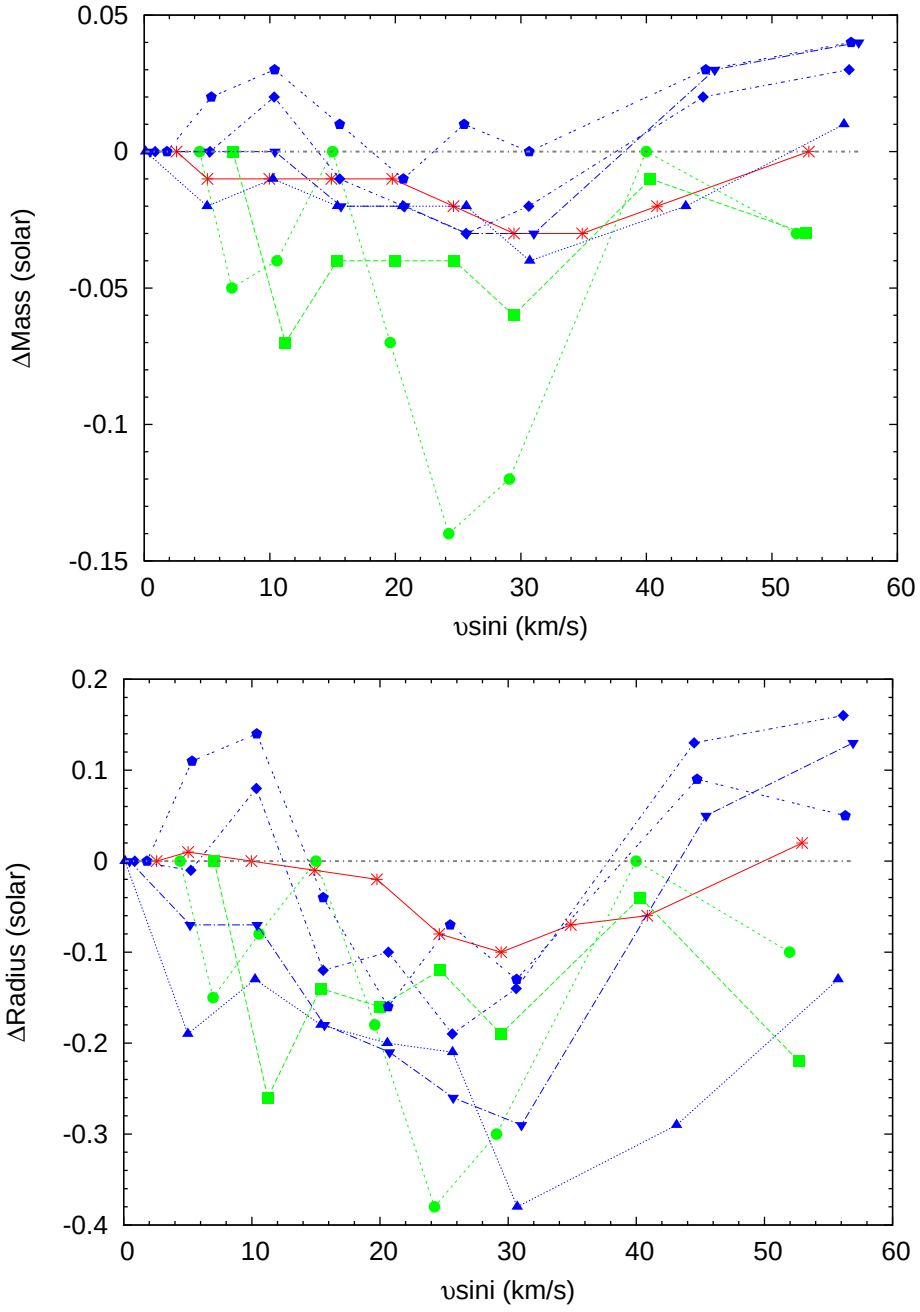

Figure 5.7: Differences in stellar mass (top panel) and radius (bottom panel) vs. $v \sin i$. The symbols are the same as in Fig. 5.4.

Table 5.5: Differences in parameters derived with different methods. N indicates the number of stars used for the comparison.

	$\Delta T_{\rm eff}$ (K)	$\Delta \log g$ (dex)	Δ [Fe/H] (dex)	N
This Work – EW	3 ± 48 (MAD = 80)	–0.11 ± 0.07 (MAD = 0.24)	0.04 ± 0.03 (MAD = 0.03)	11
This Work – Synthesis	32 ± 29 (MAD = 64)	0.03 ± 0.05 (MAD = 0.15)	0.05 ± 0.02 (MAD = 0.04)	29
This Work – Photometry	-12 ± 25 (MAD = 44)	0.06 ± 0.02 (MAD = 0.04)	– –	18

techniques, the EW method (up to $v \sin i \sim 10\,{\rm km\,s^{-1}}$), and the photometric technique, namely IRFM. The differences between this work and other methods are very small for all parameters.

In Fig. 5.8, we plot the comparison between the literature values and our results. Figure 5.9 shows each stellar parameter in dependence of rotational velocity for the different methods and for this work. Even though the mean differences in temperature are close to zero, a slight overestimation of our method appears for high $v \sin i$. Surface gravity shows the lowest dispersion when compared to trigonometric $\log g$ from all methods. Metallicity is also in agreement, excluding perhaps an outlier (HD 49933). Some examples of spectral fitting are given in Figs. 5.10- 5.11 for two stars with moderate rotation.

5.5 Data and spectroscopic parameters for planet hosts

We have identified spectra for ten confirmed planet hosts that show relatively high $v \sin i$, and we were unable to apply our standard EW method for their spectroscopic analysis. We use the procedure of this work to derive their stellar parameters to update the online SWEET-Cat catalog where stellar parameters for FGK and M planet hosts[3] are presented (Santos et al. 2013). These stars were observed with high resolution spectrographs (Table 5.6) gathered by our team (these spectra have never been analyzed before) and from the archive (for the NARVAL spectra). Their spectral type varies from F to G.

The spectra were reduced with the standard pipelines and are corrected with the standard IRAF tools for the radial velocity shifts and their spectra are added in cases of multiple exposures of individual observed stars. Following the procedure presented in this work, we derived their fundamental parameters, which are included in Figs. 5.8 and 5.9 and presented in Table 5.7. The stellar masses and radii are calculated using the calibration of Torres et al. (2010) with the corrections of Santos et al. (2013).

[3]https://www.astro.up.pt/resources/sweet-cat/

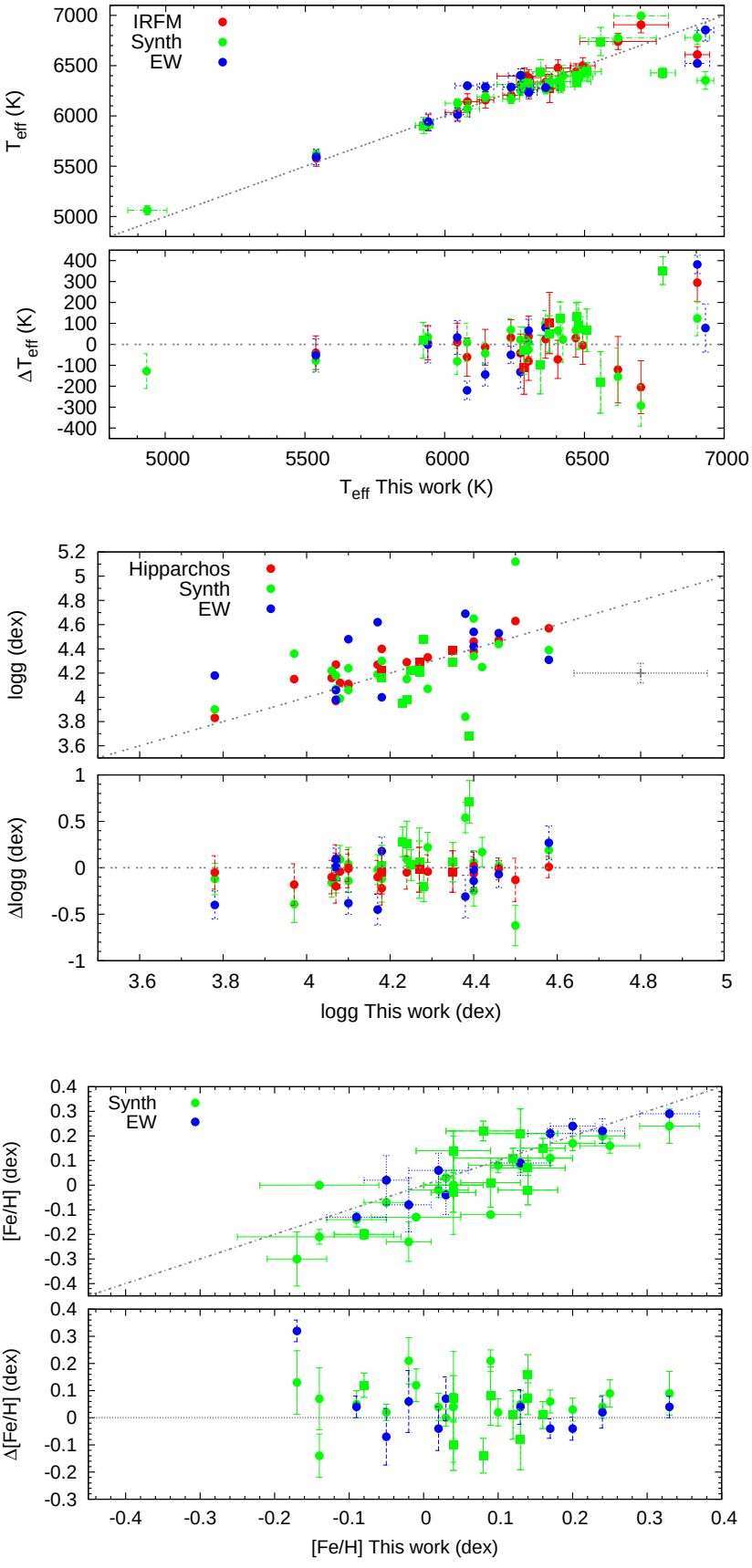

Figure 5.8: Temperature (top panel), surface gravity (middle panel), and metallicity (bottom panel). Different colors represent different techniques. Square symbols represent planet hosts analyzed in this work. In the middle panel, the average error is plotted. In each panel, the upper plot compares the data and the lower plot compares the residual differences from perfect agreement.

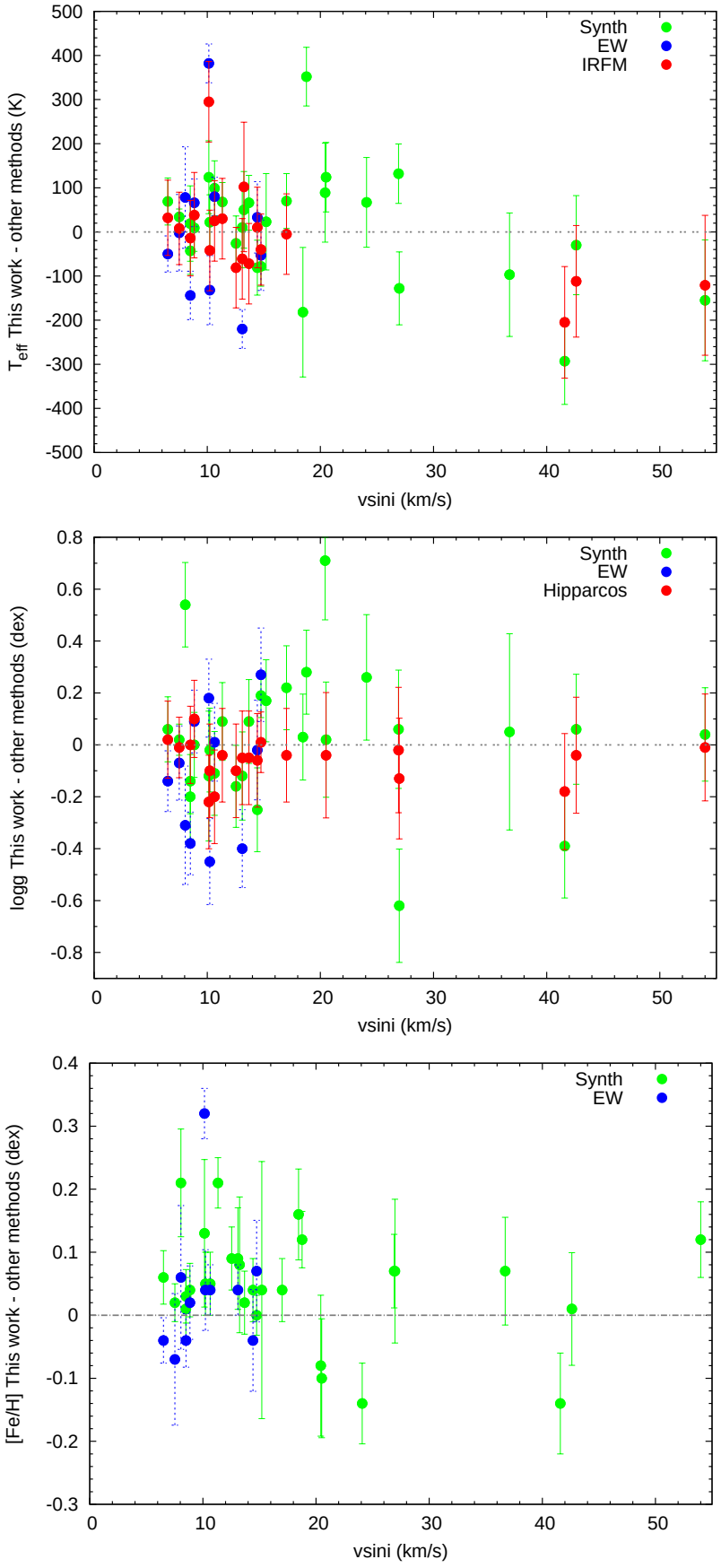

Figure 5.9: Differences in temperature (top panel), surface gravity (middle panel) and metallicity (bottom panel) versus rotational velocity for moderate/high rotators.

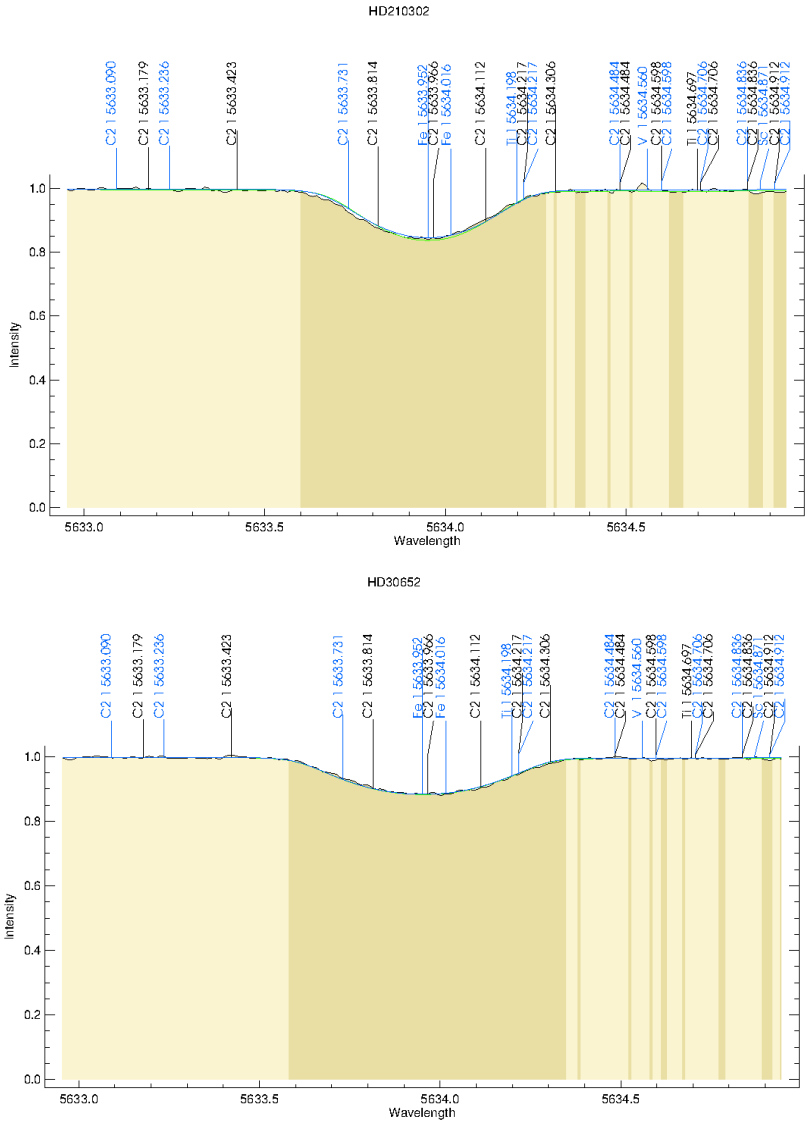

Figure 5.10: Examples of synthesis fitting of HD 210302 ($\upsilon \sin i = 13.68\,\mathrm{km\,s^{-1}}$) and HD 30652 ($\upsilon \sin i = 17.01\,\mathrm{km\,s^{-1}}$).

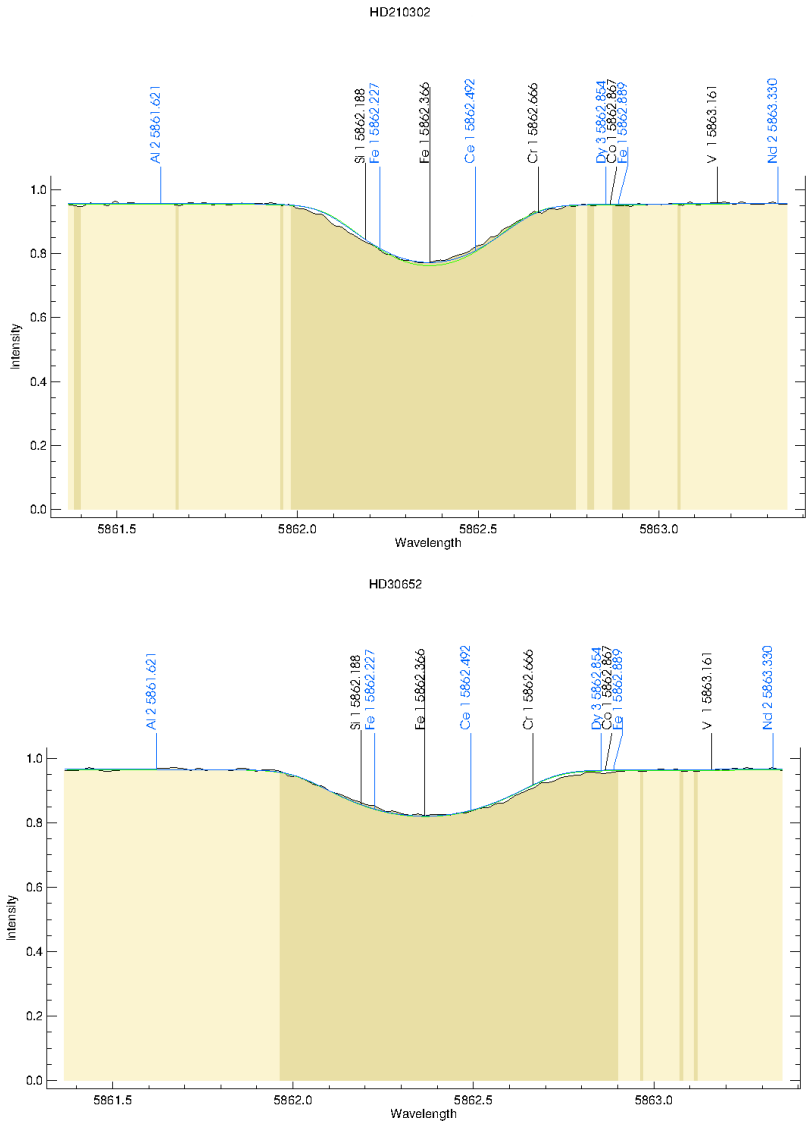

Figure 5.11: Same as Fig. 5.10.

Table 5.6: Observation log of the transit hosts analyzed in this work. V magnitudes are taken from SIMBAD. S/N is estimated at 6070 Å.

Star	V (mag)	Spectrograph	Resolution	S/N
30 Ari B	7.09	FEROS	48000	270
HAT-P-23	13.05	FEROS	48000	65
HAT-P-34	10.40	FEROS	48000	145
HAT-P-41	11.36	FEROS	48000	135
HAT-P-2	8.69	SOPHIE	75000	250
XO-3	9.85	SOPHIE	75000	130
HD 8673	6.31	NARVAL	75000	222
Kepler-410A	9.50	NARVAL	75000	72
CoRoT-11	12.80	HARPS	110000	116
CoRoT-3	13.29	HARPS	110000	84

Table 5.7: Spectroscopic parameters of planet hosts derived in this work and surface gravities derived from the transit light curve are found in the literature for all transiting planet hosts of our sample.

Star	$T_{\rm eff}$ K	$\log g$ dex	$[Fe/H]$ dex	$v \sin i$ km s^{-1}	$\log g_{transit}$ dex	Ref.	Mass $M_\odot$	Radius $R_\odot$
HAT-P-23	5924 ± 30	4.28 ± 0.11	0.16 ± 0.03	8.50 ± 0.22	4.33 ± 0.05	(1)	1.13 ± 0.05	1.29 ± 0.05
Kepler-410A	6375 ± 44	4.25 ± 0.15	0.09 ± 0.04	13.24 ± 0.29	4.13 ± 0.11	(2)	1.30 ± 0.07	1.41 ± 0.07
CoRoT-3	6558 ± 44	4.25 ± 0.15	0.14 ± 0.04	18.46 ± 0.29	4.25 ± 0.07	(3)	1.41 ± 0.08	1.44 ± 0.08
XO-3	6781 ± 44	4.23 ± 0.15	–0.08 ± 0.04	18.77 ± 0.29	4.24 ± 0.04	(4)	1.41 ± 0.08	1.49 ± 0.08
HAT-P-41	6479 ± 51	4.39 ± 0.22	0.13 ± 0.05	20.11 ± 1.34	4.22 ± 0.07	(5)	1.28 ± 0.09	1.19 ± 0.08
HAT-P-2	6414 ± 51	4.18 ± 0.22	0.04 ± 0.05	20.50 ± 1.34	4.14 ± 0.03	(6)	1.34 ± 0.09	1.54 ± 0.12
HAT-P-34	6509 ± 51	4.24 ± 0.22	0.08 ± 0.05	24.08 ± 1.34	4.21 ± 0.06	(7)	1.36 ± 0.10	1.45 ± 0.11
HD 8673	6472 ± 51	4.27 ± 0.22	0.14 ± 0.05	26.91 ± 1.34	–	–	1.35 ± 0.10	1.39 ± 0.10
CoRoT-11	6343 ± 72	4.27 ± 0.30	0.04 ± 0.03	36.72 ± 1.34	4.26 ± 0.06	(8)	1.56 ± 0.10	1.36 ± 0.13
30 Ari B	6284 ± 98	4.35 ± 0.20	0.12 ± 0.08	42.61 ± 1.82	–	–	1.22 ± 0.08	1.23 ± 0.07

(1) Bakos et al. (2011); (2) Van Eylen et al. (2014); (3) Deleuil et al. (2008); (4) Johns-Krull et al. (2008); (5) Hartman et al. (2012); (6) Pál et al. (2010); (7) Bakos et al. (2012); (8) Gandolfi et al. (2010)

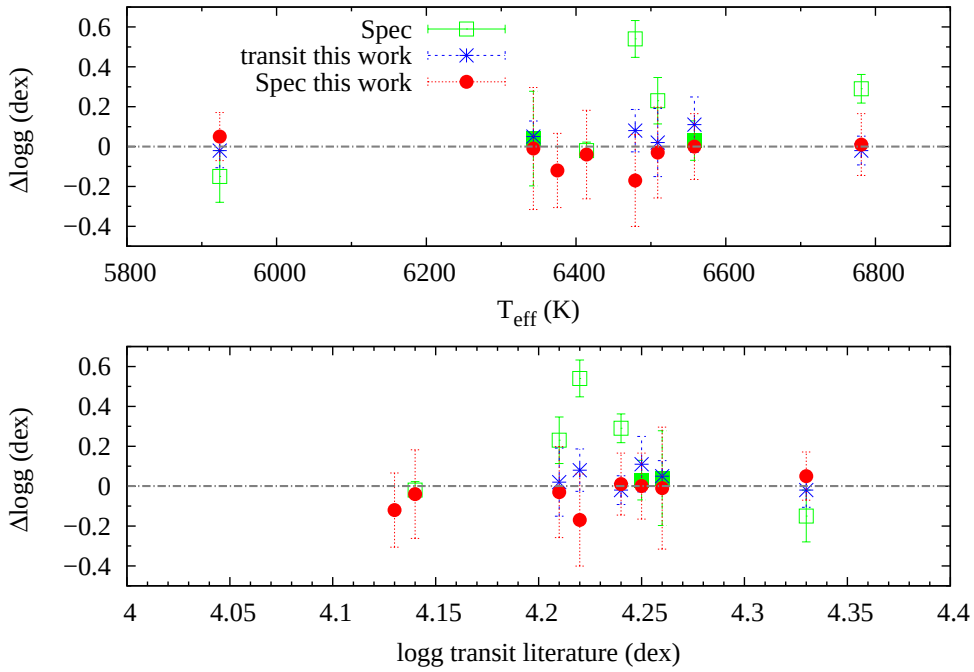

Figure 5.12: The differences refer to surface gravity derived from a transit light curve analysis minus other methods from Table 5.7. Circles correspond to the comparison of $\log g$ derived in this work. Squares correspond to the methodology applied by Valenti & Fischer (2005) and filled squares to other spectral synthesis methods. Asterisks show the comparison between $\log g$ derived from the light curve analysis on the literature and of this work.

5.5.1 Transit analysis

From the literature we retrieved available photometric data for our stars with transiting planets. Our aim was to perform a homogeneous analysis of these objects using our redetermined stellar parameters to guess limb darkening coefficients and average stellar density. The limb darkening coefficients were linearly interpolated in the four dimensions of the new stellar parameters ($T_{\rm eff}$, $\log g$, $[Fe/H]$, and υ_{mac}) from the tables of Claret & Bloemen (2011) to match our stellar parameter values. We also obtained the stellar density from the mass and radius as described in the previous section. Transit duration and transit depth were initially taken from the values quoted in the literature. The light curves were all folded with the period known from the literature, and out of transit measurements normalized to one.

Since some of the planets in our sample are in eccentric orbits, we adopted the expansion to the fourth order for the normalized projected distance of the planet with respect to the stellar center reported in Pál et al. (2010) and express it as a function of the stellar mean density ($\rho_\star$) and the transit duration (T_d).

For each folded light curve, we fit a transiting planet model using the Mandel & Agol (2002) model and the Levemberg-Marquardt algorithm (Press et al. 1992). For eccentric

Table 5.8: Transit fit parameters: planet-to-star radius ratio ($R_p/R_\star$), transit duration (T_d), stellar density ($\rho_\star$), and the linear limb darkening coefficient (g_1).

Star	$R_p/R_\star$	T_d days	$\rho_\star$ g cm^{-3}	g_1
HAT-P-23	$0.1209^{+0.0015}_{-0.0011}$	$0.0822^{+0.0005}_{-0.0008}$	$0.976^{+0.068}_{-0.102}$	$0.281^{+0.037}_{-0.056}$
HAT-P-34	$0.0842^{+0.0015}_{-0.0015}$	$0.1323^{+0.0013}_{-0.0015}$	$0.505^{+0.097}_{-0.119}$	$0.037^{+0.111}_{-0.019}$
HAT-P-41	$0.1049^{+0.0011}_{-0.0004}$	$0.1523^{+0.0004}_{-0.0009}$	$0.452^{+0.003}_{-0.054}$	$0.211^{+0.019}_{-0.044}$
XO-3	$0.0915^{+0.0006}_{-0.0007}$	$0.1043^{+0.0010}_{-0.0008}$	$0.649^{+0.060}_{-0.060}$	$0.343^{+0.030}_{-0.090}$
CoRoT-3	$0.0641^{+0.0007}_{-0.0005}$	$0.1410^{+0.0010}_{-0.0008}$	$0.431^{+0.074}_{-0.055}$	$0.202^{+0.041}_{-0.062}$
CoRoT-11	$0.0999^{+0.0006}_{-0.0005}$	$0.0799^{+0.0010}_{-0.0012}$	$0.581^{+0.034}_{-0.023}$	$0.347^{+0.062}_{-0.092}$

planets we adopted the values of the eccentricity and argument of periastron reported in the literature and add a Gaussian prior condition on both during our error analysis (see below), considering the reported uncertainties.

The uncertainties of the measurements were first expanded by the reduced χ^2 of the fit. We accounted for correlated noise by creating a mock sample of the fit residuals (using the measurement uncertainties) and by comparing the scatter in the artificial and in the real light curves. The residuals were re-binned on increasing time intervals (up to 30 min). If the ratio of the expected to the real scatter was found to be greater than one, we expanded the uncertainties further by this factor. Finally, we determined the distributions of the parameter best-fit values by bootstrapping the light curves and derived the mode of the resulting distributions and the 68.3 per cent confidence limits defined by the 15.85th and the 84.15th percentiles in the cumulative distributions.

The results are reported in Table 5.8. The photometric densities appear lower than the values implied by theoretical models. The discrepancy is greatest for the case of Kepler-410A where models predict $\rho_\star \sim 1\,\mathrm{g\ cm^{-3}}$, whereas the measured value is $0.0937^{+0.0070}_{-0.0052}$ g cm^{-3}. The dilution caused by the contamination of a stellar companion (Kepler-410B) and the small size of the planet ($2.838\,\mathrm{R_\oplus}$, Van Eylen et al. (2014)) are the main reasons for the difference in the density derived from the transit fit. Considering the above, we have excluded this star from the comparison of the transit fit results.

5.5.2 Discussion

For stars with a transiting planet, it has been proposed that surface gravity is independently derived from the light curve with better precision than from spectroscopy (Seager & Mallén-Ornelas 2003; Sozzetti et al. 2007). In Torres et al. (2012), it has been shown that $\log g$ derived using SME and the methodology of Valenti & Fischer (2005) is systematically underestimated for hotter stars ($T_{\rm eff} > 6000\,\mathrm{K}$) when compared with the $\log g$ from transit fits. According to the authors, constraining $\log g$ to the transit values, as presumably more reliable, leads to significant biases in the temperature and

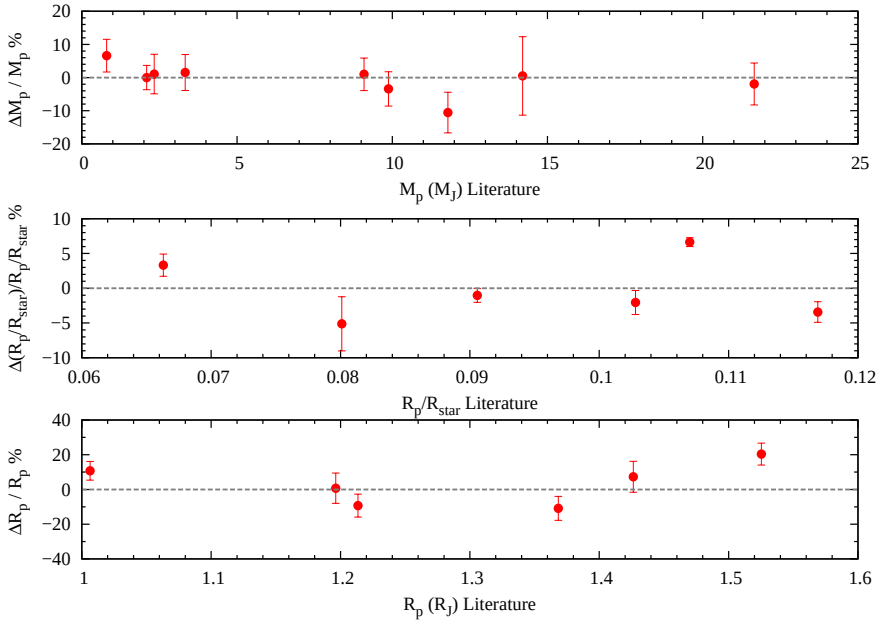

Figure 5.13: Comparison between the literature data of planetary mass, the radii ratio (R_p/R_{star}), and planetary radius and this work, respectively in absolute units.

metallicity which consequently propagates to biases in stellar (and planetary) mass and radius.

From the planet hosts in our work, there are eight stars with transit data and available $\log g$ from a light curve analysis. We therefore compare the $\log g$ derived from our spectroscopic analysis with the $\log g$ from the transit fits as taken from the literature (Fig. 5.12). The differences of this comparison are very small ($\Delta \log g$ = –0.04 with σ= 0.07 dex). On the other hand, a comparison between the $\log g$ from the transit light curve and the $\log g$ using only the unconstrained methodology of Valenti & Fischer (2005) shows an average difference of 0.18 (σ= 0.27) dex for five stars with available measurements. For completeness, we also plot the $\log g$ from our light curve analysis of the previous section, using the stellar density and mass.

Even though the number of stars for this comparison is very small, these results suggest that fixing $\log g$ to the transit value is not required with the analysis of this work, avoiding the biases that are described in Torres et al. (2012). The different approach we adopt in this work, mainly because of the different line list, shows that we obtain a better estimate on surface gravity. However, since our sample is small and limited to hotter stars, further investigation is advised to check whether following the unconstrained approach is the optimal strategy. The unconstrained analysis is also suggested in Gómez Maqueo Chew et al. (2013) as preferable, after analyzing the transit host WASP-13 with SME but following different methodology (line list, initial parameters, convergence criteria, fixed parameters) from Valenti & Fischer (2005).

We explored how the literature values of planetary mass and radius are affected with

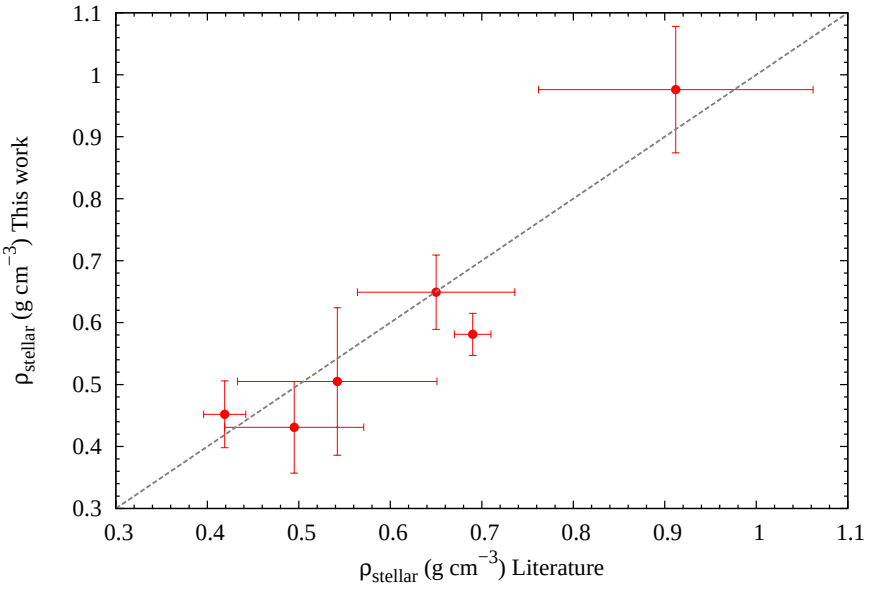

Figure 5.14: Comparison between stellar density derived from the transit light curve analysis and literature data.

the new stellar parameters. From our analysis we find that the dispersion between the planetary mass derived with our stellar parameters and the literature is 4% (Fig. 5.13, top panel). The planet-to-star radius ratio derived from the transit light curve shows the same dispersion of 4% (Fig. 5.13, middle panel). This consistency with the literature values confirms the accuracy of the transit light curve analysis for deriving the planet-to-star radius ratio. The planetary radius is calculated from this ratio and the stellar radius that is inferred from our spectroscopic values. The comparison of the planetary radius with the literature values shows the highest dispersion of 14% (Fig. 5.13, bottom panel). Since we have shown the consistency of the planet-to-star radius ratio, the main source of uncertainty in the derivation of planetary radius is the calculation of the stellar value.

We also compare the stellar density derived from the transit analysis with the respective ones from the literature (Fig. 5.14). In Fig. 5.15, we show the new mass and radius from this work in comparison with the literature values. Planetary radius shows higher discrepancies mainly because of the uncertainties in the stellar radius calculations.

The study of planet hosts with higher rotational velocities is essential because they expand the planet sample around stars of earlier types (F- and A-type) that are more massive than the Sun. Precise stellar parameters for these stars are necessary to study the frequency of planets around intermediate mass stars and explore their planet formation mechanisms. Additionally, precise (and if possible accurate) stellar parameters are essential for a detailed characterization of the planets to be discovered by the upcoming high precision transit missions such as CHEOPS, TESS, and PLATO 2.0.

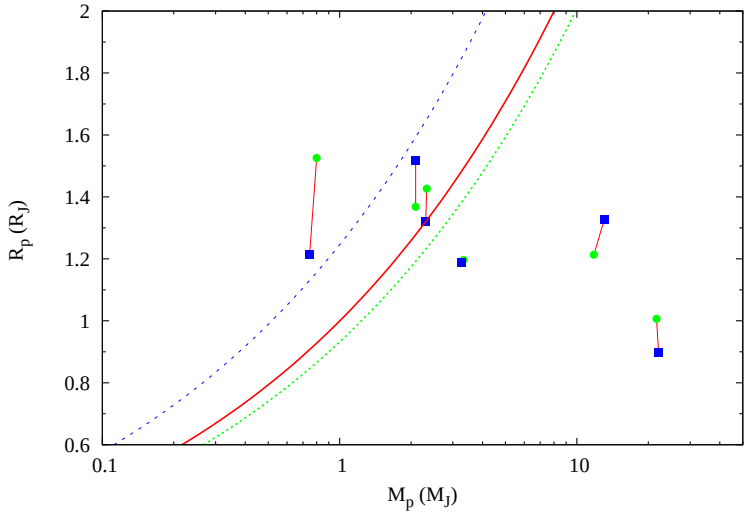

Figure 5.15: Blue squares represent planetary mass and radius derived in this work in comparison with literature values (green circles). Characteristic isodensity curves are plotted for the densities of Saturn (dashed), Jupiter (solid) and Neptune (dotted).

CHAPTER 6

Conclusions and future prospects

"I'll see you on the dark side of the moon"

Pink Floyd

6.1 Conclusions

This thesis was divided into two main projects, both related to optimizing the methods of deriving precise and accurate stellar parameters. Our work can be summarized as:

- We used the EW method and the existing tools by our team (e.g. ARES) to derive stellar parameters for 451 FGK stars. We fixed the discrepancies between our method and other more model-independent methods for the case of cool stars ($T_{\rm eff}$ <5000 K). These discrepancies were mainly due to the strong blending effects in the spectra of cool stars. After we carefully defined a line list with isolated lines, we achieved better parameters in the low temperature regime.

- The stellar parameters for stars with rotation cannot be derived using the standard EW method. For these stars we provided new methodology with the spectral

synthesis technique, based on the code SME in an automatic analysis. We used our experience on line lists to create the most effective wavelength intervals to deal with fast rotating stars.

- For this project, we used observational data to determine the stellar parameters of planet hosts with moderate and fast rotation. Their parameters were added to the online catalog of planet-host stars.

6.2 Future work

Our methods are proven to be powerful tools to analyze stars of spectral types from F to K. However, there are some issues we would like to address for future work.

- It has been shown that EW method systematically overestimates temperature only in the cases of hot stars when compared to other methods (Fig. 6.1). In the future, we aim to solve this problem by designing a line list specially for F-type stars, following the same procedure as for cool stars. Another possible reason for this disagreement could be because of the atomic data. As mentioned in Chapter 2, the atomic data are derived after an inverted solar analysis. Therefore, we expect stars far from the solar parameters to be affected by not precise values in the atomic data.

- Surface gravity is a parameter that is the most difficult to constrain with spectroscopy. In our recent work, we compared surface gravities from the EW method and the spectral synthesis technique with the one derived from the transit fit. The transit surface gravity is described as more reliable compared to the spectroscopic. From our analysis, we show that the difference $\log g_{transit} - \log g_{EW}$ correlates with temperature while the differences of our spectral synthesis values appear only for the cool stars. Mortier et al. (2013b) made the same analysis by comparing $\log g_{transit}$ with $\log g_{EW}$, and reported the same results (Fig. 6.2). An interesting study is to understand why the EW method gives $\log g$ systematically higher for cool stars and lower for hotter.

- We used the spectral synthesis tools to derive the fundamental stellar parameters for stars with moderate-to-high rotation. However, there is more information to obtain from the spectra, i.e. to measure the chemical abundances. The chemical content of a star is important. We can use our experience of iron lines to create intervals around the most important elements. A complete line list to start with is the one of Neves et al. (2009) that included 12 elements (Si, Ca, Sc, Ti, V, Cr, Mn, Co, Ni, Na, Mg, and Al) but it can also be expanded to volatile elements.

- SME is a powerful package that includes all the procedures for an automatic parameter derivation. However, there is a variety of procedures in the literature that we would like to test using exactly the same methodology. An interesting

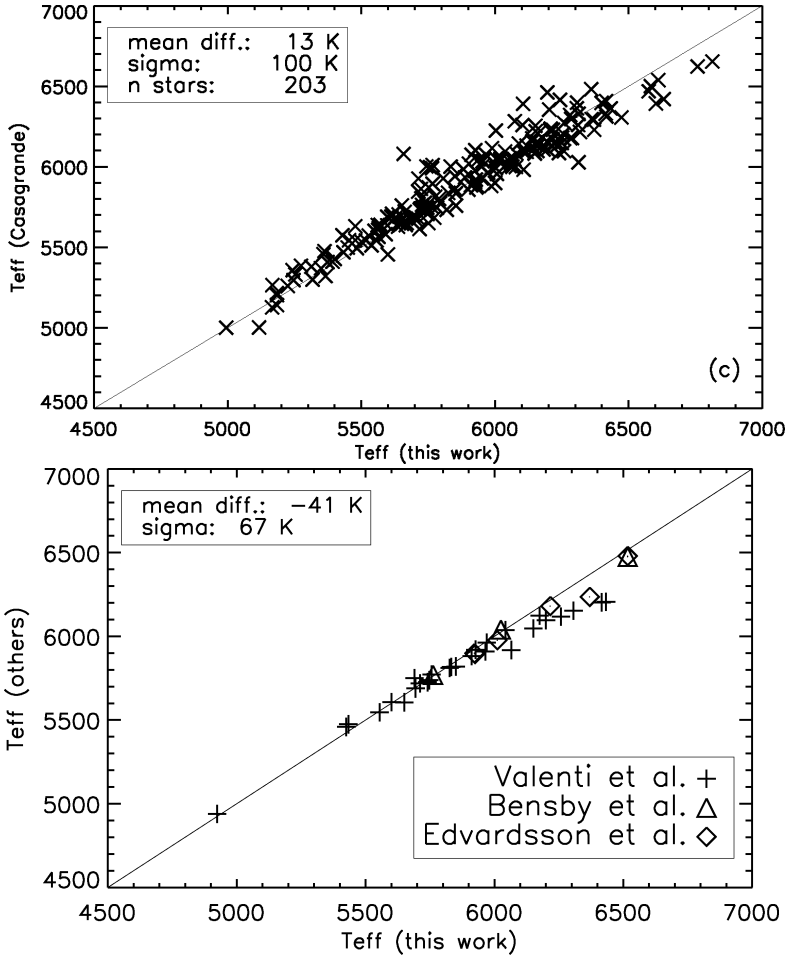

Figure 6.1: Top panel: Comparison between the effective temperature derived from Sousa et al. (2010) (This work) and Casagrande et al. (2010). Bottom panel: Comparison between the effective temperature derived from Sousa et al. (2010) (This work) and the measurements of other authors. The crosses, triangles, and diamonds represent the comparison points with the values determined by Valenti & Fischer (2005), Bensby et al. (2003), and Edvardsson et al. (1993), respectively. Taken from Sousa et al. (2010).

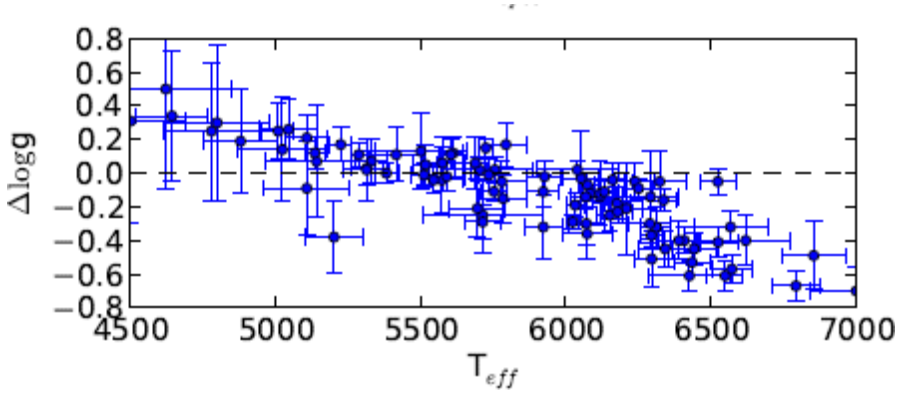

Figure 6.2: Differences in $\log g$ (defined as 'photometric - spectroscopic') as a function of the effective temperature. Taken from Mortier et al. (2013b).

test would be the comparison of different spectral synthesis codes, such as iSpec (Blanco-Cuaresma et al. 2014).

In addition, we can check our procedure with the line list provided by the GES (early results are presented in Appendix D). The GES is making an great effort to optimize the line lists with precise atomic data. The use of the GES line list will follow the purpose of homogenizing stellar parameters from different working groups for the huge sample of stars observed for the survey.

- There is still a large amount of data from follow-up observations for the characterization of planet hosts. I am participating as PI and Co-I in ongoing observing missions at ESO facilities. Once the stellar parameters are derived, we plan to address the question how stellar parameters correlate with the planetary properties. One interesting project is to study the connection of planet hosts with the Galactic parameters, such as the galactocentric distance of the stars (e.g. Adibekyan et al. 2014).

Appendices

APPENDIX A

The microturbulence relationship

Microturbulence is taken into consideration for abundance analyses to reconcile differences between the observed and predicted from models EWs of strong lines. Previous studies of FGK dwarfs have shown that ξ_t depends on $T_{\rm eff}$ and $\log g$ (e.g., Nissen 1981; Reddy et al. 2003; Allende Prieto et al. 2004; Adibekyan et al. 2012a; Ramírez et al. 2013). Using a linear regression analysis to the new parameters of the sample, we derive the following expression:

$$\xi_t = 6.932(\pm0.125) \times 10^{-4} T_{\rm eff} - 0.348(\pm0.042) \log g - 1.437(\pm0.182). \quad \text{(A.1)}$$

Here, ξ_t is in $\rm km\,s^{-1}$, $T_{\rm eff}$ and $\log g$ are in their traditional units. The parameters of the stars in the sample range:

$4400 < T_{\rm eff} < 6400$ K,

$3.6 < \log g < 4.8$ dex,

$-0.8 <$ [Fe/H] < 0.4 dex.

The new derived parameters indicate a linear dependence on temperature for a set value of surface gravity. In Fig. A.1, we see the dependence of microturbulence on temperature for a set of $\log g$ values. Microturbulence clearly increases with temperature and decreases with surface gravity.

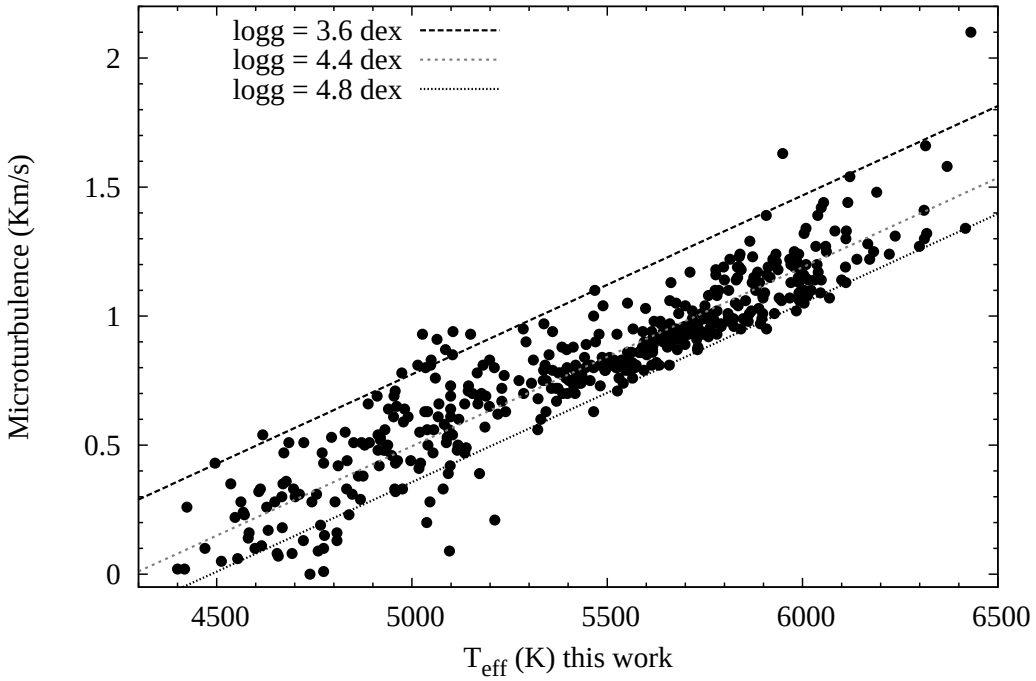

Figure A.1: Correlation of microturbulence with temperature and surface gravity as described by Equation A.1. We set $\log g$ to the highest, average and lowest values of the sample.

APPENDIX B

SME tutorial

SME is a complete package for generating synthetic spectra from atomic and molecular line lists and comparing them with observed spectra. The interface is written in IDL and the synthesis construction is implemented in C++. SME can perform several tasks including 1) construction of synthetic spectra, 2) solving for the atomic and molecular line parameters ($\log gf$ and Van Der Waals broadening), 3) perform radial velocity correction for the observed spectrum, 4) find the best-fit parameters ($T_{\rm eff}$, $\log g$, [M/H], ξ_t, υ_{mac}, $\upsilon \sin i$, and chemical abundances) between the synthetic and the observed spectrum with a χ^2 minimization procedure.

In the following sections, I will present a small tutorial on the procedure I use to determine $T_{\rm eff}$, $\log g$, [Fe/H], and $\upsilon \sin i$.

B.1 Calibrating the atomic parameters

For this analysis, SME requires a line list in VALD format where the wavelength intervals where the synthesis is conducted, are specified in the header. The selection on the line list and the intervals is described in Tsantaki et al. (2014). We used the *extract stellar* query from VALD with the following criteria:

- Detection threshold: 0.001
- Microturbulence : $0.9\,{\rm km\,s^{-1}}$
- $T_{\rm eff}$: 5777 and 4500 K
- $\log g$: 4.44 dex

If we use the standard atomic (and molecular) data to fit the spectrum of the Sun, one can notice that the fit is far from good and the best-fit parameters are not accurate enough (Fig. B.1). Since we know the solar parameters with high accuracy and precision,

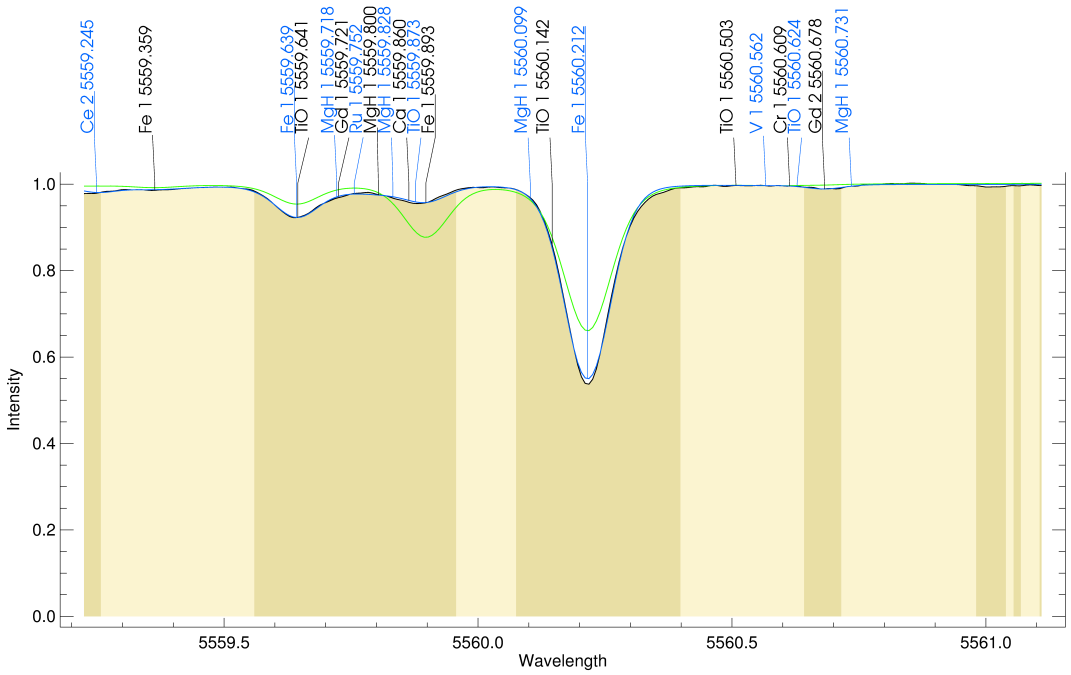

Figure B.1: Spectral synthesis for solar values using atomic data from VALD (green line) and after solar calibration (blue line). Black line indicates the solar atlas.

Figure B.2: SME main menu.

we can set the atomic data free for the set of solar values. The best-fit parameters are derived after a χ^2 minimization. The complete calibrated line list in SME readable format can be found here: http://mariatsantaki.weebly.com/sme-line-list.html.

B.2 Calculating the best-fit parameters

Once we have the line list, we can generate an initial synthetic spectrum. To do so, these are the following tasks, using the SME interface (Fig. B.2):

1. Input the line list with the regions and lines that SME will create:

   Line Data / Add all / OK

2. Create the initial synthetic spectrum for a set of initial values. These are the starting values for the minimization procedure to find the best-fit parameters. To input the initial parameters:

   Controls / Global parameters / Done

   The initial parameters should be as close to the real values as possible. The available Global parameters are: $T_{\rm eff}$, $\log g$, [M/H], ξ_t, υ_{mac}, $\upsilon \sin i$, υ_{rad}, cscale, and Γ_6 factor.

   In our analysis, we set the initial values for $T_{\rm eff}$, $\log g$, [M/H], ξ_t, υ_{mac}, and $\upsilon \sin i$ according to Section 5.2.2. The lest of the values are set fixed throughout the analysis. All our spectra were corrected for radial velocity shifts, so this value is set to zero. The cscale value is the continuum normalization parameter and it is calculated for each segment (interval). Finally, the Γ_6 factor is the enhancement parameter is a correction that affects all lines globally. We use the value 2.5 that fits the solar spectrum better in Valenti & Piskunov (1996).

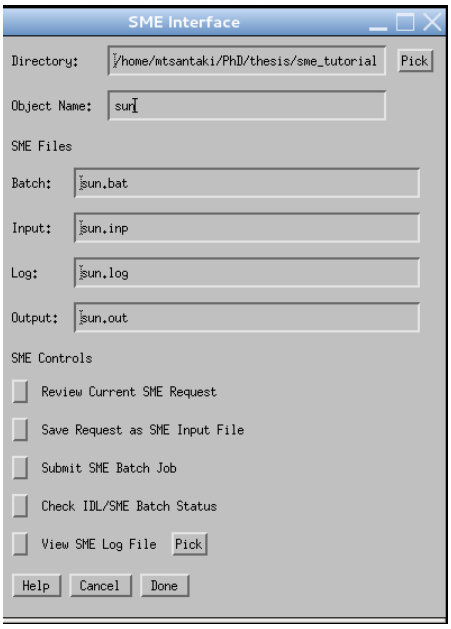

Figure B.3: SME interface for setting the minimization procedure.

3. We set which parameters we want to set free. SME includes a variety of parameters to define. One has to be careful which parameters to set free because there may be a degeneracy between them that leads in biased results. For instance, $\upsilon \sin i$ and υ_{mac} could be degenerate for slowly rotating stars. In our analysis, we set free: $T_{\rm eff}$, $\log g$, [M/H], and $\upsilon \sin i$.

   Controls / Free Parameters / Done

4. To match a synthetic spectrum with the observed we have to introduce instrumental broadening. This parameter depends on the spectral resolution of the spectrograph (R $\sim \lambda$ / $\Delta\lambda$). We fill with the value R for a Gaussian profile.

   Controls / Instrumental profile / Gaussian / Done

5. Once the initial parameters are defined, we can input the observed spectrum. SME accepts a variety of formats for the input observed spectra, e.g. ASCII, fits, dat, IDL inputs, and a solar atlas.

   Observations / Read observations from disk / Done

6. Finally, we have defined all the necessary inputs to determine the stellar parameters. The last task performs the minimization procedure based on a χ^2 algorithm that produces the best-fit parameters. In the task Jobs, the user defines the name for a series of output files (Fig. B.3).

   Batch: an IDL script file for automatic run of the input file

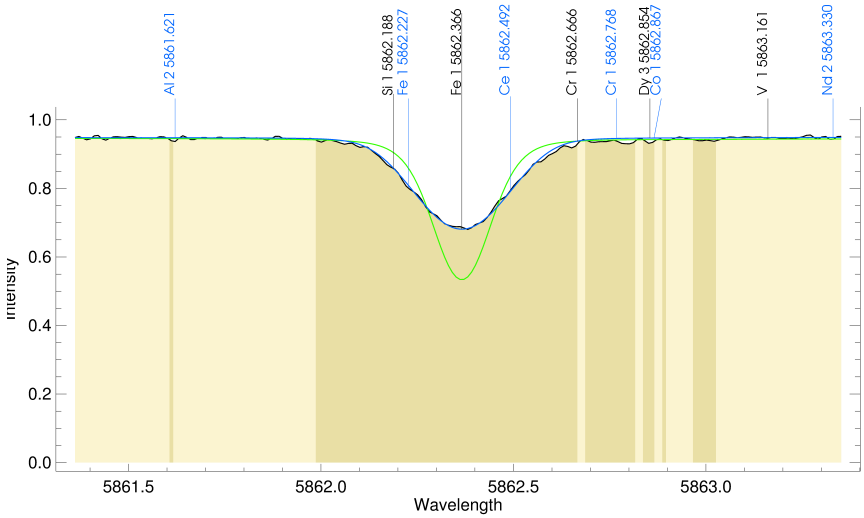

Figure B.4: An example of the SME output for HD103774. The green line indicates the spectrum with the initial parameters, the blue line the fit with the final parameters, and the black the observed one. The grey area shows what SME recognizes as line points and the pink area shows the continuum points.

Input: contains all the input information we inserted in the format of IDL structure

Log: file that keeps the records of the calculations. The final parameters with the χ^2 values are also listed.

Output: contains the output information with all the SME calculations

In summary, the procedure is the following for this task:

Jobs / Save Request as SME Input File / Submit SME Batch Job

B.3 Evaluating the results

After SME computes the free parameters, we can visually evaluate the results by checking the final synthetic spectrum with the best-fit parameters. First, we choose the output file (*.out) from the following menu items:

Examine / Read SME structure from disk / Done

Examine / Plot Flux Profiles

In Fig. B.4 there is an example of the initial and final synthesis that provide the best-fit parameters. To list the values of the free parameters:

Examine / Print free parameters

APPENDIX C

Stellar parameters with synthesis

Table C.1: Results of the comparison between this work and the EW method for dwarf stars. The stars in boldface are analyzed in Sect. 5.3.

	This work				EW method		
Star	$T_{\rm eff}$ (K)	$\log g$ (dex)	[Fe/H] (dex)	$v \sin i$ ($\mathrm{km\,s^{-1}}$)	$T_{\rm eff}$ (K)	$\log g$ (dex)	[Fe/H] (dex)
CoRoT-2	5620 ± 18	4.66 ± 0.06	-0.03 ± 0.03	9.97	5697 ± 97	4.73 ± 0.17	-0.09 ± 0.07
CoRoT-10	4921 ± 25	4.09 ± 0.09	0.15 ± 0.03	2.19	5025 ± 155	4.47 ± 0.31	0.06 ± 0.09
CoRoT-4	6164 ± 30	4.34 ± 0.11	0.15 ± 0.03	7.03	6344 ± 93	4.82 ± 0.11	0.15 ± 0.06
CoRoT-5	6254 ± 30	4.41 ± 0.11	0.04 ± 0.03	1.43	6240 ± 70	4.46 ± 0.11	0.04 ± 0.05
HD 101930	5083 ± 18	4.15 ± 0.06	0.10 ± 0.03	0.10	5083 ± 63	4.35 ± 0.13	0.16 ± 0.04
HD 102365	5588 ± 18	4.07 ± 0.06	-0.30 ± 0.03	0.10	5616 ± 41	4.40 ± 0.06	-0.28 ± 0.03
HD 103774	6582 ± 30	4.47 ± 0.11	0.27 ± 0.03	8.93	6732 ± 56	4.81 ± 0.06	0.29 ± 0.03
HD 1237	5588 ± 18	4.58 ± 0.06	0.11 ± 0.03	4.62	5489 ± 40	4.46 ± 0.11	0.06 ± 0.03
HD 134060	5914 ± 18	4.28 ± 0.06	0.09 ± 0.03	1.44	5940 ± 18	4.42 ± 0.03	0.12 ± 0.01
HD 1388	5967 ± 18	4.38 ± 0.06	0.00 ± 0.03	1.27	5970 ± 15	4.42 ± 0.05	0.00 ± 0.01
HD 148156	6212 ± 30	4.40 ± 0.11	0.23 ± 0.03	5.73	6251 ± 25	4.51 ± 0.05	0.25 ± 0.02
HD 162020	4798 ± 25	4.14 ± 0.09	-0.14 ± 0.03	1.46	4723 ± 71	4.31 ± 0.18	-0.10 ± 0.03
HD 20852	6675 ± 30	4.12 ± 0.11	-0.37 ± 0.03	7.06	6813 ± 92	4.76 ± 0.12	-0.35 ± 0.06
HD 20868	4745 ± 25	4.02 ± 0.09	0.00 ± 0.03	0.46	4720 ± 91	4.24 ± 0.47	0.08 ± 0.01
HD 221287	6337 ± 30	4.43 ± 0.06	0.02 ± 0.06	3.92	6417 ± 25	4.60 ± 0.10	0.06 ± 0.02
HD 222237	4618 ± 25	3.92 ± 0.09	-0.50 ± 0.03	0.10	4722 ± 55	4.34 ± 0.15	-0.39 ± 0.06
HD 23079	5965 ± 18	4.28 ± 0.06	-0.13 ± 0.03	0.10	6009 ± 14	4.50 ± 0.05	-0.11 ± 0.01
HD 27894	4894 ± 25	4.08 ± 0.09	0.18 ± 0.03	0.87	4833 ± 209	4.30 ± 0.48	0.26 ± 0.10
HD 31527	5915 ± 18	4.40 ± 0.06	-0.17 ± 0.03	2.36	5917 ± 13	4.47 ± 0.05	-0.17 ± 0.01
HD 330075	4924 ± 30	4.03 ± 0.09	-0.04 ± 0.03	0.10	4958 ± 52	4.24 ± 0.13	0.05 ± 0.03
HD 361	5924 ± 18	4.48 ± 0.06	-0.10 ± 0.03	0.10	5888 ± 14	4.54 ± 0.08	-0.13 ± 0.01
HD 38283	5962 ± 18	4.14 ± 0.06	-0.15 ± 0.03	4.51	5980 ± 24	4.27 ± 0.03	-0.14 ± 0.02
HD 40307	4771 ± 25	4.10 ± 0.09	-0.42 ± 0.03	0.10	4774 ± 77	4.42 ± 0.16	-0.36 ± 0.02
HD 61421	6616 ± 30	4.09 ± 0.11	0.03 ± 0.03	4.40	6612	4.02	-0.02
HD 63454	4833 ± 25	4.11 ± 0.09	0.04 ± 0.03	1.81	4756 ± 77	4.32 ± 0.22	0.13 ± 0.05
HD 750	5118 ± 18	4.34 ± 0.06	-0.29 ± 0.03	0.10	5069 ± 32	4.33 ± 0.1	-0.30 ± 0.02
HD 870	5379 ± 18	4.36 ± 0.06	-0.12 ± 0.03	0.10	5360 ± 24	4.40 ± 0.08	-0.12 ± 0.02
HD 93385	5987 ± 18	4.38 ± 0.06	0.02 ± 0.03	1.06	5989 ± 17	4.46 ± 0.03	0.03 ± 0.01
HD 967	5643 ± 18	4.38 ± 0.06	-0.59 ± 0.03	0.10	5595 ± 18	4.59 ± 0.02	-0.66 ± 0.01
OGLE-TR-113	4793 ± 25	4.25 ± 0.09	0.05 ± 0.03	5.02	4781 ± 166	4.31 ± 0.41	0.03 ± 0.06
WASP-29	4782 ± 25	4.13 ± 0.09	0.18 ± 0.03	0.10	5203 ± 102	4.93 ± 0.21	0.17 ± 0.05
WASP-15	6378 ± 30	4.24 ± 0.11	0.03 ± 0.03	5.13	6573 ± 70	4.79 ± 0.08	0.09 ± 0.03
WASP-16	5710 ± 18	4.23 ± 0.06	0.12 ± 0.03	0.47	5726 ± 22	4.34 ± 0.05	0.13 ± 0.02
WASP-17	6666 ± 30	4.26 ± 0.06	-0.04 ± 0.03	9.93	6794 ± 83	4.83 ± 0.09	-0.12 ± 0.05
WASP-2	5105 ± 18	3.97 ± 0.06	0.08 ± 0.03	2.90	5109 ± 72	4.33 ± 0.14	0.02 ± 0.05
WASP-23	5053 ± 18	4.20 ± 0.06	-0.02 ± 0.03	0.46	5046 ± 99	4.33 ± 0.18	0.05 ± 0.06
WASP-38	6247 ± 30	4.25 ± 0.11	0.06 ± 0.03	8.05	6436 ± 60	4.80 ± 0.07	0.06 ± 0.04
WASP-6	5447 ± 18	4.42 ± 0.06	-0.11 ± 0.03	0.10	5383 ± 41	4.52 ± 0.06	-0.14 ± 0.03
Sun	5771 ± 18	4.42 ± 0.06	0.00 ± 0.03	2.57	–	–	–

The values of the Sun were calculated from observations of the reflected light from Ganymede with S/N of 150.

Table C.2: Results of the comparison between this work and the EW method for giant stars. The stars in boldface are analyzed in Sect. 5.3.

	This work				EW method		
Star	$T_{\rm eff}$ (K)	$\log g$ (dex)	[Fe/H] (dex)	$v \sin i$ ($\rm km\,s^{-1}$)	$T_{\rm eff}$ (K)	$\log g$ (dex)	[Fe/H] (dex)
HD 148427	5018 ± 25	3.49 ± 0.09	0.01 ± 0.03	0.45	4962 ± 45	3.39 ± 0.12	0.03 ± 0.03
HD 175541	5097 ± 18	3.44 ± 0.06	-0.14 ± 0.03	2.45	5111 ± 38	3.56 ± 0.08	-0.11 ± 0.03
HD 27442	4852 ± 25	3.48 ± 0.09	0.23 ± 0.03	2.65	4781 ± 76	3.46 ± 0.19	0.33 ± 0.05
HD 62509	5007 ± 25	3.06 ± 0.09	0.21 ± 0.03	3.76	4935 ± 49	2.91 ± 0.13	0.09 ± 0.04
HD 88133	5330 ± 18	3.62 ± 0.06	0.20 ± 0.03	3.39	5438 ± 34	3.94 ± 0.11	0.33 ± 0.05
HD 142091	4898 ± 25	3.24 ± 0.09	0.05 ± 0.03	4.38	4876 ± 46	3.15 ± 0.14	0.13 ± 0.03
HD 188310	4799 ± 18	3.14 ± 0.06	-0.06 ± 0.03	5.28	4714 ± 49	2.53 ± 0.11	-0.27 ± 0.04
HD 163917	5107 ± 18	2.82 ± 0.06	0.33 ± 0.03	4.21	4967 ± 61	2.70 ± 0.13	0.14 ± 0.05

Table C.3: Stellar parameters for a sample of fast rotating FGK dwarfs.

Star	$T_{\rm eff}{}_{IRFM}$ K	Ref.	$\log g_{HIP}$ dex	$T_{\rm eff}$ K	$\log g$ dex	$[Fe/H]$ dex	Ref.	$T_{\rm eff}{}_{Synth}$ K	$\log g_{Synth}$ dex	$[Fe/H]_{Synth}$ dex	Ref.	$T_{\rm eff}{}_{EW}$ K	$\log g_{EW}$ dex	$[Fe/H]_{EW}$ dex	Ref.	$\upsilon \sin i$ km s^{-1}
HD 179949	6205 ± 80	(1)	4.38 ± 0.10	6237 ± 30	4.40 ± 0.11	0.17 ± 0.03	This work	6168 ± 44	4.34 ± 0.06	0.11 ± 0.03	(3)	6287 ± 28	4.54 ± 0.04	0.21 ± 0.02	(18)	6.52
HD 165185	5932 ± 80	(1)	4.47 ± 0.10	5940 ± 18	4.46 ± 0.06	-0.05 ± 0.03	This work	5906	4.44	-0.07	(4)	5942 ± 85	4.53 ± 0.13	0.02 ± 0.10	19	7.53
HAT-P-6	–	–	–	6933 ± 30	4.38 ± 0.11	-0.02 ± 0.03	This work	6353 ± 88	3.84 ± 0.12	-0.23 ± 0.08	(5)	6855 ± 111	4.69 ± 0.20	-0.08 ± 0.11	(20)	8.06
HAT-P-23	–	–	–	5924 ± 30	4.28 ± 0.11	0.16 ± 0.03	This work	5905 ± 80	4.48 ± 0.12	0.15 ± 0.04	(10)	–	–	–	–	8.50
HD 19994	6159 ± 80	(1)	4.10 ± 0.10	6145 ± 30	4.10 ± 0.11	0.20 ± 0.03	This work	6188 ± 44	4.24 ± 0.06	0.17 ± 0.03	(3)	6289 ± 46	4.48 ± 0.05	0.24 ± 0.03	(18)	8.51
HD 89744	6262 ± 92	(1)	3.97 ± 0.10	6300 ± 30	4.07 ± 0.11	0.24 ± 0.03	This work	6291 ± 44	4.07 ± 0.06	0.20 ± 0.03	(3)	6234 ± 45	3.98 ± 0.05	0.22 ± 0.05	(21)	8.86
HD 49933	6609 ± 80	(1)	4.40 ± 0.10	6904 ± 44	4.18 ± 0.15	-0.17 ± 0.04	This work	6780 ± 70	4.30 ± 0.20	-0.30 ± 0.11	(6)	6522	4.00	-0.49	22	10.14
HD 142	6313 ± 80	(1)	4.27 ± 0.10	6271 ± 44	4.17 ± 0.15	0.13 ± 0.04	This work	6249 ± 44	4.19 ± 0.06	0.08 ± 0.03	(3)	6403 ± 65	4.62 ± 0.07	0.09 ± 0.05	(18)	10.22
HD 142860	6336 ± 80	(1)	4.27 ± 0.10	6361 ± 44	4.07 ± 0.15	-0.09 ± 0.04	This work	6262 ± 44	4.18 ± 0.06	-0.14 ± 0.03	(3)	6281	4.06	-0.13	(22)	10.65
HD 89569	6439 ± 80	(1)	4.12 ± 0.10	6469 ± 44	4.08 ± 0.15	0.09 ± 0.04	This work	6401	3.99	-0.12	(4)	–	–	–	–	11.33
HD 86264	6381 ± 80	(1)	4.16 ± 0.10	6300 ± 44	4.06 ± 0.15	0.25 ± 0.04	This work	6326 ± 44	4.22 ± 0.05	0.16 ± 0.03	(3)	6596 ± 78	4.47 ± 0.15	0.37 ± 0.06	(23)	12.55
HD 121370	6141 ± 80	(1)	3.83 ± 0.10	6080 ± 44	3.78 ± 0.15	0.33 ± 0.04	This work	6030 ± 80	3.90 ± 0.08	0.24 ± 0.07	(7)	6300	4.18	0.29	(22)	13.10
Kepler-410A	6273 ± 140	(2)	–	6375 ± 44	4.25 ± 0.15	0.09 ± 0.04	This work	6325 ± 75	–	0.01 ± 0.10	8	–	–	–	–	13.24
HD 210302	6477 ± 80	(1)	4.29 ± 0.10	6405 ± 44	4.24 ± 0.15	0.10 ± 0.04	This work	6339 ± 44	4.15 ± 0.06	0.08 ± 0.03	(3)	–	–	–	–	13.68
HD 105	6035 ± 80	(1)	4.46 ± 0.10	6045 ± 44	4.40 ± 0.15	0.02 ± 0.04	This work	6126 ± 44	4.65 ± 0.06	-0.02 ± 0.03	(3)	6012 ± 68	4.42 ± 0.12	0.06 ± 0.07	(24)	14.43
HD 202917	5579 ± 80	(1)	4.57 ± 0.10	5539 ± 10	4.58 ± 0.06	0.03 ± 0.01	This work	5617 ± 44	4.39 ± 0.06	0.03 ± 0.03	(3)	5592 ± 79	4.31 ± 0.17	-0.04 ± 0.08	(24)	14.75
WASP-3	–	–	–	6423 ± 44	4.42 ± 0.15	0.04 ± 0.04	This work	6400 ± 100	4.25 ± 0.05	0.00 ± 0.20	(9)	6448 ± 123	4.49 ± 0.08	-0.02 ± 0.08	(25)	15.21
HD 30652	6499 ± 80	(1)	4.33 ± 0.10	6494 ± 44	4.29 ± 0.15	0.04 ± 0.04	This work	6424 ± 44	4.07 ± 0.06	0.00 ± 0.03	(3)	–	–	–	–	17.01
CoRoT-3	–	–	–	6558 ± 44	4.25 ± 0.15	0.14 ± 0.04	This work	6740 ± 140	4.22 ± 0.07	-0.02 ± 0.06	(11)	–	–	–	–	18.46
XO-3	–	–	–	6781 ± 44	4.23 ± 0.15	-0.08 ± 0.04	This work	6429 ± 50	3.95 ± 0.06	-0.20 ± 0.02	(12)	–	–	–	–	18.77
HAT-P-41	–	–	–	6479 ± 51	4.39 ± 0.22	0.13 ± 0.05	This work	6390 ± 100	3.68 ± 0.06	0.21 ± 0.10	(13)	–	–	–	–	20.11
HAT-P-2	–	–	4.22 ± 0.10	6414 ± 51	4.18 ± 0.22	0.04 ± 0.05	This work	6290 ± 60	4.16 ± 0.03	0.14 ± 0.08	(14)	–	–	–	–	20.50
HAT-P-34	–	–	–	6509 ± 51	4.24 ± 0.22	0.08 ± 0.05	This work	6442 ± 88	3.98 ± 0.10	0.22 ± 0.04	(15)	–	–	–	–	24.08
HD 8673	–	–	4.29 ± 0.10	6472 ± 51	4.27 ± 0.22	0.14 ± 0.05	This work	6340 ± 44	4.21 ± 0.06	0.07 ± 0.03	(3)	–	–	–	–	26.91
HD 82558	–	–	4.63 ± 0.11	4934 ± 70	4.50 ± 0.21	-0.14 ± 0.11	This work	5062 ± 44	5.12 ± 0.06	-0.21 ± 0.03	(3)	–	–	–	–	26.97
CoRoT-11	–	–	–	6343 ± 72	4.27 ± 0.30	0.04 ± 0.03	This work	6440 ± 120	4.22 ± 0.23	-0.03 ± 0.08	(16)	–	–	–	–	36.72
HD 64685	6907 ± 80	(1)	4.15 ± 0.12	6702 ± 98	3.97 ± 0.20	-0.14 ± 0.08	This work	6995	4.36	0.00	(4)	–	–	–	–	41.59
30 Ari B	6396 ± 80	(1)	4.39 ± 0.12	6284 ± 60	4.35 ± 0.25	0.12 ± 0.06	This work	6314 ± 55	4.29 ± 0.07	0.11 ± 0.04	(17)	–	–	–	–	42.61
HD 219877	6741 ± 80	(1)	4.11 ± 0.13	6620 ± 137	4.10 ± 0.18	-0.01 ± 0.06	This work	6775	4.06	-0.13	(4)	–	–	–	–	54.00

(1) Casagrande et al. (2011); (2) Van Eylen et al. (2014); (3) Valenti & Fischer (2005); (4) Gray et al. (2006); (5) Noyes et al. (2008); (6) Bruntt et al. (2004); (7) Bruntt et al. (2010); (8) Huber et al. (2013); (9) Pollacco et al. (2008); (10) Bakos et al. (2011); (11) Deleuil et al. (2008); (12) Johns-Krull et al. (2008); (13) Hartman et al. (2012); (14) Pál et al. (2010); (15) Bakos et al. (2012); (16) Gandolfi et al. (2010) (17) Prugniel et al. (2011); (18) Sousa et al. (2008); (19) Santos et al. (2005); (20) Ammler-von Eiff et al. (2009); (21) Santos et al. (2004); (22) Takeda (2007); (23) Santos et al. (2013); (24) Viana Almeida et al. (2009); (25) Montalto et al. (2012)

APPENDIX D

The Gaia-ESO line list

Gaia-ESO (GES) is a public spectroscopic survey, targeting 10^5 stars, systematically covering all major components of the Milky Way, from halo to star forming regions, providing the first homogeneous overview of the distributions of kinematics and elemental abundances. One of the key goals of this survey is to provide homogeneous parameters for the the large amount of the observed spectra from the ESO facilities. We used the GES line list (version 4) to derive stellar parameters for the GES benchmark stars presented in Jofré et al. (2014). The GES methogology suggests to use MARCS models and the provided line list.

I used the high resolution and high S/N spectra provided in their database for the benchmark stars. I used the same methodology described in Chapter 5. The only difference in this analysis is the use of the line list and model atmospheres. I kept the same wavelength intervals but included only the lines with their atomic data provided but the GES. The results for the stars that this method is applied are shown below. The extremely metal poor stars and M-dwarfs were excluded.

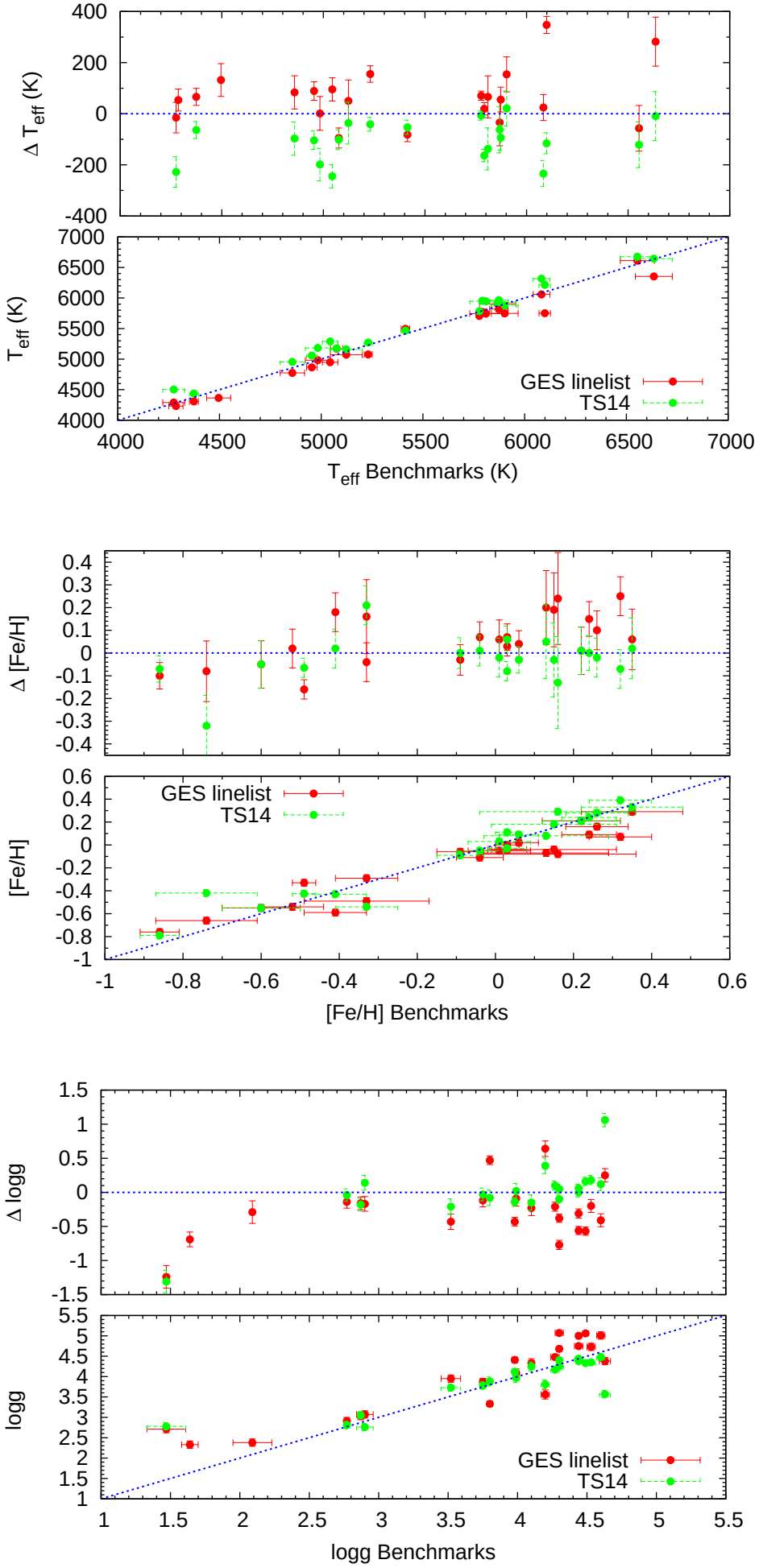

Figure D.1: Comparison between the stellar parameters derived with our methodology (green points) and our methodology+the GES line list (red points). Top figure: The x-axis shows the literature values for temperature as published in Jofré et al. (2014). Middle figure: Same for metallicity. Bottom figure: Same for surface gravity.

APPENDIX E

The iron line list

Table E.1: The complete line list used for the spectroscopic analysis of Chapter 3 with the atomic parameters of Fe I and Fe II as well as the corresponding EWs of the Sun

λ (Å)	χ	$\log gf$	Element	EW (mÅ)
4523.40	3.65	–1.871	FeI	44.2
4537.67	3.27	–2.870	FeI	17.4
4551.65	3.94	–1.928	FeI	29.1
4556.93	3.25	–2.644	FeI	26.3
4566.52	3.30	–2.156	FeI	46.2
4574.22	3.21	–2.353	FeI	41.0
4593.53	3.94	–1.921	FeI	29.5
4596.41	3.65	–2.090	FeI	34.1
4602.00	1.61	–3.163	FeI	72.2
4630.12	2.28	–2.488	FeI	74.3
4631.49	4.55	–1.890	FeI	11.6
4661.54	4.56	–1.186	FeI	38.5
4690.14	3.69	–1.550	FeI	58.8
4802.88	3.69	–1.527	FeI	60.4
4808.15	3.25	–2.630	FeI	27.7
4809.94	3.57	–2.542	FeI	19.4
4811.05	3.07	–3.182	FeI	14.5
4885.43	3.88	–1.136	FeI	72.5
4961.92	3.63	–2.301	FeI	26.7
5127.36	0.92	–3.317	FeI	99.4
5141.74	2.42	–2.125	FeI	89.3
5223.19	3.63	–2.252	FeI	29.4
5228.38	4.22	–1.095	FeI	60.0
5242.50	3.63	–1.124	FeI	86.7
5243.78	4.26	–1.022	FeI	62.2
5247.06	0.09	–4.941	FeI	66.4
5294.55	3.64	–2.627	FeI	15.5
5295.32	4.42	–1.518	FeI	29.3
5376.83	4.29	–2.040	FeI	14.7
5379.58	3.69	–1.552	FeI	61.2
5386.34	4.15	–1.709	FeI	32.1
5389.48	4.42	–0.534	FeI	84.6
5398.28	4.45	–0.684	FeI	73.3
5409.14	4.37	–1.051	FeI	55.7
5432.95	4.45	–0.729	FeI	70.6
5436.30	4.39	–1.319	FeI	40.5

5464.28	4.14	–1.595	FeI	38.2
5466.99	3.65	–2.141	FeI	34.2
5473.17	4.19	–1.986	FeI	19.5
5522.45	4.21	–1.419	FeI	44.0
5543.94	4.22	–1.070	FeI	62.2
5546.51	4.37	–1.124	FeI	52.0
5560.22	4.43	–1.064	FeI	52.4
5584.77	3.57	–2.189	FeI	35.8
5618.64	4.21	–1.298	FeI	50.5
5619.60	4.39	–1.435	FeI	35.0
5633.95	4.99	–0.385	FeI	66.5
5636.70	3.64	–2.511	FeI	19.8
5638.27	4.22	–0.809	FeI	77.6
5649.99	5.10	–0.785	FeI	36.2
5651.47	4.47	–1.763	FeI	18.4
5653.87	4.39	–1.402	FeI	36.7
5679.03	4.65	–0.756	FeI	59.5
5680.24	4.19	–2.330	FeI	10.3
5715.09	4.28	–0.847	FeI	72.5
5720.90	4.55	–1.805	FeI	14.9
5738.24	4.22	–2.164	FeI	13.6
5775.08	4.22	–1.124	FeI	59.8
5793.92	4.22	–1.622	FeI	34.0
5811.92	4.14	–2.333	FeI	11.4
5814.81	4.28	–1.820	FeI	23.0
5815.22	4.15	–2.364	FeI	10.5
5853.15	1.49	–5.130	FeI	7.5
5855.08	4.61	–1.531	FeI	22.3
5862.36	4.55	–0.404	FeI	87.6
5902.48	4.59	–1.797	FeI	14.2
5905.68	4.65	–0.775	FeI	58.7
5927.79	4.65	–1.057	FeI	42.9
5929.68	4.55	–1.211	FeI	39.5
5930.19	4.65	–0.326	FeI	87.9
5934.66	3.93	–1.091	FeI	76.4
5956.70	0.86	–4.526	FeI	53.7
5983.69	4.55	–0.719	FeI	67.2
5987.07	4.79	–0.478	FeI	70.2
6005.55	2.59	–3.479	FeI	22.4
6024.06	4.55	–0.124	FeI	110.5
6056.01	4.73	–0.489	FeI	72.6
6078.49	4.79	–0.364	FeI	77.9
6079.01	4.65	–1.008	FeI	45.8
6089.57	4.58	–1.273	FeI	35.3
6094.38	4.65	–1.566	FeI	19.9
6096.67	3.98	–1.776	FeI	38.2
6120.25	0.92	–5.894	FeI	5.2
6127.91	4.14	–1.417	FeI	48.9
6151.62	2.18	–3.298	FeI	49.7
6157.73	4.08	–1.238	FeI	61.5
6159.38	4.61	–1.878	FeI	11.9
6173.34	2.22	–2.877	FeI	68.0
6200.32	2.61	–2.397	FeI	73.0
6219.29	2.20	–2.463	FeI	89.6
6226.74	3.88	–2.069	FeI	29.2
6232.65	3.65	–1.240	FeI	83.3

6240.65	2.22	–3.292	FeI	48.3
6270.23	2.86	–2.573	FeI	52.8
6315.81	4.08	–1.645	FeI	40.5
6322.69	2.59	–2.368	FeI	76.0
6335.34	2.20	–2.339	FeI	97.2
6358.68	0.86	–3.907	FeI	84.4
6392.54	2.28	–3.942	FeI	17.8
6481.88	2.28	–2.929	FeI	64.1
6593.88	2.43	–2.384	FeI	84.6
6609.12	2.56	–2.632	FeI	65.7
6627.55	4.55	–1.475	FeI	28.2
6646.94	2.61	–3.915	FeI	10.3
6699.15	4.59	–2.106	FeI	8.2
6705.11	4.61	–1.057	FeI	46.5
6710.32	1.49	–4.810	FeI	15.9
6713.74	4.79	–1.425	FeI	21.2
6725.36	4.10	–2.187	FeI	17.6
6726.67	4.61	–1.045	FeI	47.2
6732.07	4.58	–2.144	FeI	7.7
6739.52	1.56	–4.902	FeI	11.7
6745.97	4.08	–2.657	FeI	7.2
6839.84	2.56	–3.377	FeI	29.9
6842.69	4.64	–1.169	FeI	39.3
6855.72	4.61	–1.674	FeI	18.6
6857.25	4.08	–2.075	FeI	22.4
6858.15	4.61	–0.972	FeI	51.6
6861.94	2.42	–3.795	FeI	18.9
6864.32	4.56	–2.229	FeI	6.8
4508.28	2.86	–2.403	FeII	87.3
4520.22	2.81	–2.563	FeII	81.9
4576.34	2.84	–2.947	FeII	64.9
4656.98	2.89	–3.676	FeII	33.8
4731.47	2.89	–2.515	FeII	82.1
4923.93	2.89	–1.541	FeII	154.3
5197.57	3.23	–2.293	FeII	80.1
5234.63	3.22	–2.235	FeII	83.5
5264.81	3.23	–3.091	FeII	45.6
5337.75	3.23	–3.338	FeII	35.5
5414.07	3.22	–3.568	FeII	26.9
5991.38	3.15	–3.539	FeII	31.2
6149.25	3.89	–2.719	FeII	36.2
6247.56	3.89	–2.347	FeII	52.2
6442.97	5.55	–2.399	FeII	5.1
6456.39	3.90	–2.110	FeII	63.0
6516.09	2.89	–3.279	FeII	54.2

PUBLICATIONS RELATED TO THE THESIS

[1] M. Tsantaki, S. G. Sousa, N. C. Santos, M. Montalto, E. Delgado-Mena, A. Mortier, V. Adibekyan, and G. Israelian. Spectroscopic parameters for solar-type stars with moderate-to-high rotation. New parameters for ten planet hosts. *A&A*, 570:A80, October 2014.

[2] J. Molenda-Żakowicz, S. G. Sousa, A. Frasca, K. Uytterhoeven, M. Briquet, H. Van Winckel, D. Drobek, E. Niemczura, P. Lampens, J. Lykke, S. Bloemen, J. F. Gameiro, C. Jean, D. Volpi, N. Gorlova, A. Mortier, M. Tsantaki, and G. Raskin. Atmospheric parameters of 169 F-, G-, K- and M-type stars in the Kepler field. *MNRAS*, 434:1422–1434, September 2013.

[3] A. Mortier, N. C. Santos, S. G. Sousa, V. Z. Adibekyan, E. Delgado Mena, M. Tsantaki, G. Israelian, and M. Mayor. New and updated stellar parameters for 71 evolved planet hosts. On the metallicity-giant planet connection. *A&A*, 557:A70, September 2013.

[4] N. C. Santos, S. G. Sousa, A. Mortier, V. Neves, V. Adibekyan, M. Tsantaki, E. Delgado Mena, X. Bonfils, G. Israelian, M. Mayor, and S. Udry. SWEET-Cat: A catalogue of parameters for Stars With ExoplanETs. I. New atmospheric parameters and masses for 48 stars with planets. *A&A*, 556:A150, August 2013.

[5] M. Tsantaki, S. G. Sousa, V. Z. Adibekyan, N. C. Santos, A. Mortier, and G. Israelian. Deriving precise parameters for cool solar-type stars. Optimizing the iron line list. *A&A*, 555:A150, July 2013.

Acknowledgments

I would like to acknowledge my beloved supervisors, Sergio and Nuno for the privilege of working with them. I am grateful for all the opportunities, experiences, knowledge I gained from you, but also because I never heard the word 'deadline' from neither of you. Thank you for your patience and support.

I would like to acknowledge the support of CAUP for offering my PhD grant from the Starting Grant (reference 239953), awarded by the European Research Council/European Community under the FP7 to Nuno Santos.

I would like to thank the team of CAUP that welcomed me as family. I gained precious friends who I list in random order: Elisa, Daniel, Jorge, Babs, Guilherme, Vardan, Mahmoud, Pedro, it's been a long journey. I learned a lot from our multi-cultural environment. I also thank: my office-mates that dealt with my not so good singing; Elsa, Filipe, Paulo that made my life easier dealing with bureaucracy and non-cooperative computers; the staff from Casagricola that hosted me a second institution.

I would like also to thank the person that guided me in my first steps in research, my ex-supervisor, A. Zezas.

Also I would like to thank people unrelated to the thesis, but without them I would certainly not be here: my family, of course, for the endless support even though they never wanted me to leave home; tin aderfi mou gia tis valerianes; Gianna, Rena, Eleni kai o neos tis pareas Konstantinos, sas agapo; Maria kai Eleana, gia ta xronia sto Irakleio kai gia tin upostiriksi meso Skype; Peblo den exo logia.

Last but not least, I would like to thank the all the people from Porto that were very hospitable to a foreigner like me and made me feel like home. I will certainly miss this place.

BIBLIOGRAPHY

Adibekyan, V. Z., Delgado Mena, E., Sousa, S. G., et al. 2012a, A&A, 547, A36

Adibekyan, V. Z., Figueira, P., Santos, N. C., et al. 2013, A&A, 554, A44

Adibekyan, V. Z., Santos, N. C., Sousa, S. G., et al. 2012b, A&A, 543, A89

Adibekyan, V. Z., Sousa, S. G., Santos, N. C., et al. 2012c, A&A, 545, A32

Albrecht, S., Winn, J. N., Johnson, J. A., et al. 2012, ApJ, 757, 18

Allende Prieto, C., Barklem, P. S., Lambert, D. L., & Cunha, K. 2004, A&A, 420, 183

Allende Prieto, C., Ruiz Cobo, B., & García López, J. 1998, ApJ, 502, 951

Ammler-von Eiff, M., Santos, N. C., Sousa, S. G., et al. 2009, A&A, 507, 523

Bakos, G. Á., Hartman, J., Torres, G., et al. 2011, ApJ, 742, 116

Bakos, G. Á., Hartman, J. D., Torres, G., et al. 2012, AJ, 144, 19

Bazot, M., Ireland, M. J., Huber, D., et al. 2011, A&A, 526, L4

Bensby, T., Feltzing, S., & Lundström, I. 2003, A&A, 410, 527

Bensby, T., Feltzing, S., & Oey, M. S. 2014, A&A, 562, A71

Bergemann, M., Lind, K., Collet, R., Magic, Z., & Asplund, M. 2012, MNRAS, 427, 27

Bessell, M. S., Castelli, F., & Plez, B. 1998, A&A, 333, 231

Blackwell, D. E. & Shallis, M. J. 1977, MNRAS, 180, 177

Blanco-Cuaresma, S., Soubiran, C., Heiter, U., & Jofré, P. 2014, A&A, 569, A111

Bodaghee, A., Santos, N. C., Israelian, G., & Mayor, M. 2003, A&A, 404, 715

Bond, J. C., O'Brien, D. P., & Lauretta, D. S. 2010, ApJ, 715, 1050

Boss, A. P. 2002, ApJ, 567, L149

Bouchy, F., Pepe, F., & Queloz, D. 2001, A&A, 374, 733

Bouvier, J. 2008, A&A, 489, L53

Boyajian, T. S., McAlister, H. A., van Belle, G., et al. 2012a, ApJ, 746, 101

Boyajian, T. S., von Braun, K., van Belle, G., et al. 2012b, ApJ, 757, 112

Brott, I. & Hauschildt, P. H. 2005, in ESA Special Publication, Vol. 576, The Three-Dimensional Universe with Gaia, ed. C. Turon, K. S. O'Flaherty, & M. A. C. Perryman, 565

Bruntt, H., Basu, S., Smalley, B., et al. 2012, MNRAS, 423, 122

Bruntt, H., Bedding, T. R., Quirion, P.-O., et al. 2010, MNRAS, 405, 1907

Bruntt, H., Bikmaev, I. F., Catala, C., et al. 2004, A&A, 425, 683

Bruntt, H., Catala, C., Garrido, R., et al. 2002, A&A, 389, 345

Buchhave, L. A., Latham, D. W., Johansen, A., et al. 2012, Nature, 486, 375

Burrows, A., Guillot, T., Hubbard, W. B., et al. 2000, ApJ, 534, L97

Casagrande, L., Portinari, L., & Flynn, C. 2006, MNRAS, 373, 13

Casagrande, L., Ramírez, I., Meléndez, J., Bessell, M., & Asplund, M. 2010, A&A, 512, A54

Casagrande, L., Schönrich, R., Asplund, M., et al. 2011, A&A, 530, A138

Castelli, F. & Kurucz, R. L. 2004, ArXiv Astrophysics e-prints

Castro, M., Vauclair, S., Richard, O., & Santos, N. C. 2008, Mem. Soc. Astron. Italiana, 79, 679

Cayrel, R., van't Veer-Menneret, C., Allard, N. F., & Stehlé, C. 2011, A&A, 531, A83

Claret, A. 2000, A&A, 363, 1081

Claret, A. & Bloemen, S. 2011, A&A, 529, A75

Colavita, M. M., Wallace, J. K., Hines, B. E., et al. 1999, ApJ, 510, 505

da Silva, L., Girardi, L., Pasquini, L., et al. 2006, A&A, 458, 609

Davis, J., Ireland, M. J., North, J. R., et al. 2011, PASA, 28, 58

Davis, J. & Tango, W. J. 1986, Nature, 323, 234

Deleuil, M., Deeg, H. J., Alonso, R., et al. 2008, A&A, 491, 889

Delgado Mena, E., Israelian, G., González Hernández, J. I., et al. 2014, A&A, 562, A92

Doyle, A. P., Davies, G. R., Smalley, B., Chaplin, W. J., & Elsworth, Y. 2014, MNRAS, 444, 3592

Dyck, H. M., Benson, J. A., van Belle, G. T., & Ridgway, S. T. 1996, AJ, 111, 1705

Edvardsson, B., Andersen, J., Gustafsson, B., et al. 1993, A&A, 275, 101

Fischer, D. A. & Valenti, J. 2005, ApJ, 622, 1102

Flower, P. J. 1996, ApJ, 469, 355

Frasca, A., Alcalá, J. M., Covino, E., et al. 2003, A&A, 405, 149

Fuhrmann, K. 2004, Astronomische Nachrichten, 325, 3

Gandolfi, D., Hébrard, G., Alonso, R., et al. 2010, A&A, 524, A55

Gilli, G., Israelian, G., Ecuvillon, A., Santos, N. C., & Mayor, M. 2006, A&A, 449, 723

Gilmore, G. & Reid, N. 1983, MNRAS, 202, 1025

Gilmore, G., Wyse, R. F. G., & Kuijken, K. 1989, ARA&A, 27, 555

Girardi, L., Bertelli, G., Bressan, A., et al. 2002, A&A, 391, 195

Glindemann, A., Abuter, R., Carbognani, F., et al. 2000, in Society of Photo-Optical Instrumentation Engineers (SPIE) Conference Series, Vol. 4006, Interferometry in Optical Astronomy, ed. P. Léna & A. Quirrenbach, 2–12

Gómez Maqueo Chew, Y., Faedi, F., Cargile, P., et al. 2013, ApJ, 768, 79

Gonzalez, G. 1997, MNRAS, 285, 403

Gonzalez, G. & Vanture, A. D. 1998, A&A, 339, L29

Gray, D. F. 1984, ApJ, 281, 719

Gray, D. F. 1994, PASP, 106, 1248

Gray, D. F. 2005, The Observation and Analysis of Stellar Photospheres

Gray, R. O., Corbally, C. J., Garrison, R. F., et al. 2006, AJ, 132, 161

Guillot, T., Santos, N. C., Pont, F., et al. 2006, A&A, 453, L21

Gustafsson, B., Edvardsson, B., Eriksson, K., et al. 2008, A&A, 486, 951

Hartman, J. D., Bakos, G. Á., Béky, B., et al. 2012, AJ, 144, 139

Haywood, M. 2008, A&A, 482, 673

Hebb, L., Collier-Cameron, A., Loeillet, B., et al. 2009, ApJ, 693, 1920

Hekker, S. & Meléndez, J. 2007, A&A, 475, 1003

Hjerting, F. 1938, ApJ, 88, 508

Hubeny, I., Lanz, T., & Jeffery, C. S. 1994

Huber, D., Chaplin, W. J., Christensen-Dalsgaard, J., et al. 2013, ApJ, 767, 127

Ida, S. & Lin, D. N. C. 2004, ApJ, 616, 567

Israelian, G., Delgado Mena, E., Santos, N. C., et al. 2009, Nature, 462, 189

Israelian, G., Santos, N. C., Mayor, M., & Rebolo, R. 2004, A&A, 414, 601

Ivezić, Ž., Beers, T. C., & Jurić, M. 2012, ARA&A, 50, 251

Jofré, P., Heiter, U., Soubiran, C., et al. 2014, A&A, 564, A133

Jofré, P., Panter, B., Hansen, C. J., & Weiss, A. 2010, A&A, 517, A57

Johns-Krull, C. M., McCullough, P. R., Burke, C. J., et al. 2008, ApJ, 677, 657

Johnson, J. A., Winn, J. N., Bakos, G. Á., et al. 2011, ApJ, 735, 24

Kang, W. & Lee, S.-G. 2012, MNRAS, 425, 3162

Katz, D., Soubiran, C., Cayrel, R., Adda, M., & Cautain, R. 1998, A&A, 338, 151

Kervella, P. & Fouqué, P. 2008, A&A, 491, 855

Kervella, P., Thévenin, F., Ségransan, D., et al. 2003, A&A, 404, 1087

Koleva, M., Prugniel, P., Bouchard, A., & Wu, Y. 2009, A&A, 501, 1269

Kovtyukh, V. V., Soubiran, C., Belik, S. I., & Gorlova, N. I. 2003, A&A, 411, 559

Kupka, F., Piskunov, N., Ryabchikova, T. A., Stempels, H. C., & Weiss, W. W. 1999, A&AS, 138, 119

Kupka, F. G., Ryabchikova, T. A., Piskunov, N. E., Stempels, H. C., & Weiss, W. W. 2000, Baltic Astronomy, 9, 590

Kurucz, R. 1993, ATLAS9 Stellar Atmosphere Programs and 2 km/s grid. Kurucz CD-ROM No. 13. Cambridge, Mass.: Smithsonian Astrophysical Observatory, 1993., 13

Kurucz, R. L., Furenlid, I., Brault, J., & Testerman, L. 1984, Solar flux atlas from 296 to 1300 nm

Lai, D. K., Bolte, M., Johnson, J. A., et al. 2008, ApJ, 681, 1524

Laughlin, G., Crismani, M., & Adams, F. C. 2011, ApJ, 729, L7

Lind, K., Bergemann, M., & Asplund, M. 2012, MNRAS, 427, 50

Magrini, L., Randich, S., Friel, E., et al. 2013, A&A, 558, A38

Malavolta, L., Sneden, C., Piotto, G., et al. 2014, AJ, 147, 25

Mandel, K. & Agol, E. 2002, ApJ, 580, L171

Marcy, G. W., Isaacson, H., Howard, A. W., et al. 2014, ApJS, 210, 20

Mashonkina, L., Gehren, T., Shi, J.-R., Korn, A. J., & Grupp, F. 2011, A&A, 528, A87

Mayor, M., Pepe, F., Queloz, D., et al. 2003, The Messenger, 114, 20

Mayor, M. & Queloz, D. 1995, Nature, 378, 355

McAlister, H. A., ten Brummelaar, T. A., Gies, D. R., et al. 2005, ApJ, 628, 439

Mihalas, D. M. 1982, Stellar atmospheres.

Molenda-Żakowicz, J., Sousa, S. G., Frasca, A., et al. 2013, MNRAS, 434, 1422

Montalto, M., Gregorio, J., Boué, G., et al. 2012, MNRAS, 427, 2757

Mordasini, C., Alibert, Y., Benz, W., Klahr, H., & Henning, T. 2012, A&A, 541, A97

Morel, T. & Micela, G. 2004, A&A, 423, 677

Mortier, A., Santos, N. C., Sousa, S. G., et al. 2013a, A&A, 557, A70

Mortier, A., Santos, N. C., Sousa, S. G., et al. 2013b, A&A, 558, A106

Mozurkewich, D., Johnston, K. J., Simon, R. S., et al. 1991, AJ, 101, 2207

Mucciarelli, A., Pancino, E., Lovisi, L., Ferraro, F. R., & Lapenna, E. 2013, ApJ, 766, 78

Neuforge-Verheecke, C. & Magain, P. 1997, A&A, 328, 261

Neves, V., Santos, N. C., Sousa, S. G., Correia, A. C. M., & Israelian, G. 2009, A&A, 497, 563

Nielsen, M. B., Gizon, L., Schunker, H., & Karoff, C. 2013, A&A, 557, L10

Nissen, P. E. 1981, A&A, 97, 145

Nordgren, T. E., Germain, M. E., Benson, J. A., et al. 1999, AJ, 118, 3032

Noyes, R. W., Bakos, G. Á., Torres, G., et al. 2008, ApJ, 673, L79

Pál, A., Bakos, G. Á., Torres, G., et al. 2010, MNRAS, 401, 2665

Pijpers, F. P., Teixeira, T. C., Garcia, P. J., et al. 2003, A&A, 406, L15

Pinsonneault, M. H., An, D., Molenda-Żakowicz, J., et al. 2012, ApJS, 199, 30

Piskunov, N. E. 1992, in Physics and Evolution of Stars: Stellar Magnetism, ed. Y. V. Glagolevskij & I. I. Romanyuk, 92

Piskunov, N. E., Kupka, F., Ryabchikova, T. A., Weiss, W. W., & Jeffery, C. S. 1995, A&AS, 112, 525

Pollacco, D., Skillen, I., Collier Cameron, A., et al. 2008, MNRAS, 385, 1576

Pollack, J. B., Hubickyj, O., Bodenheimer, P., et al. 1996, Icarus, 124, 62

Pradhan, A. K. & Nahar, S. N. 2011, Atomic Astrophysics and Spectroscopy

Press, W. H., Teukolsky, S. A., Vetterling, W. T., & Flannery, B. P. 1992, Numerical recipes in FORTRAN. The art of scientific computing

Preston, G. W., Sneden, C., Thompson, I. B., Shectman, S. A., & Burley, G. S. 2006, AJ, 132, 85

Prugniel, P., Vauglin, I., & Koleva, M. 2011, A&A, 531, A165

Ramírez, I., Allende Prieto, C., & Lambert, D. L. 2007, A&A, 465, 271

Ramírez, I., Allende Prieto, C., & Lambert, D. L. 2013, ApJ, 764, 78

Ramírez, I., Fish, J. R., Lambert, D. L., & Allende Prieto, C. 2012, ApJ, 756, 46

Ramírez, I. & Meléndez, J. 2004, ApJ, 609, 417

Ramírez, I. & Meléndez, J. 2005, ApJ, 626, 446

Recio-Blanco, A., Bijaoui, A., & de Laverny, P. 2006, MNRAS, 370, 141

Reddy, B. E., Lambert, D. L., & Allende Prieto, C. 2006, MNRAS, 367, 1329

Reddy, B. E., Tomkin, J., Lambert, D. L., & Allende Prieto, C. 2003, MNRAS, 340, 304

Ruchti, G. R., Bergemann, M., Serenelli, A., Casagrande, L., & Lind, K. 2013, MNRAS, 429, 126

Rybicki, G. B. & Lightman, A. P. 1985, Radiative processes in astrophysics.

Saar, S. H. & Osten, R. A. 1997, MNRAS, 284, 803

Santos, N. C., Israelian, G., & Mayor, M. 2004, A&A, 415, 1153

Santos, N. C., Israelian, G., Mayor, M., et al. 2005, A&A, 437, 1127

Santos, N. C., Sousa, S. G., Mortier, A., et al. 2013, A&A, 556, A150

Schuler, S. C., King, J. R., Terndrup, D. M., et al. 2006, ApJ, 636, 432

Schuler, S. C., Plunkett, A. L., King, J. R., & Pinsonneault, M. H. 2010, PASP, 122, 766

Seager, S. & Mallén-Ornelas, G. 2003, ApJ, 585, 1038

Ségransan, D., Mayor, M., Udry, S., et al. 2011, A&A, 535, A54

Sneden, C. A. 1973, PhD thesis, The University of Texas at Austin.

Sousa, S. G., Fernandes, J., Israelian, G., & Santos, N. C. 2010, A&A, 512, L5

Sousa, S. G., Santos, N. C., Adibekyan, V., et al. 2014, A&A, 561, A21

Sousa, S. G., Santos, N. C., Israelian, G., Mayor, M., & Monteiro, M. J. P. F. G. 2007, A&A, 469, 783

Sousa, S. G., Santos, N. C., Israelian, G., Mayor, M., & Udry, S. 2011, A&A, 533, A141

Sousa, S. G., Santos, N. C., Mayor, M., et al. 2008, A&A, 487, 373

Sozzetti, A., Torres, G., Charbonneau, D., et al. 2007, ApJ, 664, 1190

Stetson, P. B. & Pancino, E. 2008, PASP, 120, 1332

Suda, T., Yamada, S., Katsuta, Y., et al. 2011, MNRAS, 412, 843

Tabernero, H. M., Montes, D., & González Hernández, J. I. 2012, A&A, 547, A13

Takeda, Y. 2007, PASJ, 59, 335

Teixeira, T. C., Kjeldsen, H., Bedding, T. R., et al. 2009, A&A, 494, 237

Teske, J. K., Cunha, K., Schuler, S. C., Griffith, C. A., & Smith, V. V. 2013, ApJ, 778, 132

Thévenin, F., Kervella, P., Pichon, B., et al. 2005, A&A, 436, 253

Thygesen, A. O., Frandsen, S., Bruntt, H., et al. 2012, A&A, 543, A160

Tolstoy, E., Hill, V., & Tosi, M. 2009, ARA&A, 47, 371

Torres, G. 2010, AJ, 140, 1158

Torres, G., Andersen, J., & Giménez, A. 2010, A&A Rev., 18, 67

Torres, G., Fischer, D. A., Sozzetti, A., et al. 2012, ApJ, 757, 161

Torres, G., Winn, J. N., & Holman, M. J. 2008, ApJ, 677, 1324

Tsantaki, M., Sousa, S. G., Adibekyan, V. Z., et al. 2013, A&A, 555, A150

Tsantaki, M., Sousa, S. G., Santos, N. C., et al. 2014, A&A, 570, A80

Udry, S., Mayor, M., Naef, D., et al. 2000, A&A, 356, 590

Unsöld, A. 1955, Physik der Sternatmospharen, MIT besonderer Berucksichtigung der Sonne.

Valencia, D., Sasselov, D. D., & O'Connell, R. J. 2007, ApJ, 665, 1413

Valenti, J. A. & Fischer, D. A. 2005, ApJS, 159, 141

Valenti, J. A. & Piskunov, N. 1996, A&AS, 118, 595

Valenti, J. A., Piskunov, N., & Johns-Krull, C. M. 1998, ApJ, 498, 851

van Belle, G. T. & von Braun, K. 2009, ApJ, 694, 1085

Van Eylen, V., Lund, M. N., Silva Aguirre, V., et al. 2014, ApJ, 782, 14

van Leeuwen, F. 2007, A&A, 474, 653

Viana Almeida, P., Santos, N. C., Melo, C., et al. 2009, A&A, 501, 965

Winn, J. N., Fabrycky, D., Albrecht, S., & Johnson, J. A. 2010, ApJ, 718, L145

Yong, D., Lambert, D. L., Allende Prieto, C., & Paulson, D. B. 2004, ApJ, 603, 697

Zeng, L. & Sasselov, D. 2013, PASP, 125, 227

Zeng, L. & Seager, S. 2008, PASP, 120, 983